CHEMICAL AND STUCTURAL ASPECTS OF ILMENITE TO RUTILE/HEMATITE TRANSFORMATION

Nadežda Stanković

Doctoral Dissertation
Jožef Stefan International Postgraduate School
Ljubljana, Slovenia

Supervisor: Asst. Prof. Dr. Nina Daneu, Jožef Stefan Institute, Ljubljana, Slovenia
Co-Supervisor: Asst. Prof. Dr. Aleksander Rečnik, Jožef Stefan Institute, Ljubljana, Slovenia

Evaluation Board:
Prof. Dr. Miran Čeh, Chair, Jožef Stefan Institute, Ljubljana, Slovenia
Prof. Dr. Anton Meden, Faculty of Chemistry and Chemical Technology, University of Ljubljana, Slovenia
Prof. Dr. Werner Mader, Member, Universität Bonn, Germany

MEDNARODNA PODIPLOMSKA ŠOLA JOŽEFA STEFANA
JOŽEF STEFAN INTERNATIONAL POSTGRADUATE SCHOOL



Nadežda Stanković

CHEMICAL AND STRUCTURAL ASPECTS OF ILMENITE TO RUTILE/HEMATITE TRANSFORMATION

Doctoral Dissertation

KEMIJSKI IN STRUKTURNI VIDIKI TRANSFORMACIJE ILMENITA V RUTIL IN HEMATIT

Doktorska disertacija

Supervisor: Asst. Prof. Dr. Nina Daneu

Co-Supervisor: Asst. Prof. Dr. Aleksander Rečnik

Ljubljana, Slovenia, February 2016

To my family, my super secret super group and AAA

Acknowledgments

First, I would like to thank my supervisor Nina Daneu for fruitful discussion, suggestions and for guiding me through the experimental work, as well for the great help with writing. Also I am gratefully tankful to her for teaching me how to do a scientific work in the best way. It was my great honour to be her first PhD student. Also I would like to thank my co-supervisor Aleksander Rečnik for helping me with the TEM investigations, and teaching me about microscopy, and for guidance with writing the scientific papers. I am also gratefully thankful to the members of the commission board, Miran Čeh, Anton Meden and Werner Mader for helpful suggestions and constructive criticism.

I am also gratefully thankful to Branko Matović, who told be about the scholarship for this PhD studies, and without whom I wouldn't even be in the science. Also, I would like to thank Medeja Gec for her great help with the TEM sample preparation and Sašo Šturm for his help with EELS analyses.

Of great help were also my co-workers with whom I discussed the problems and challenges of my work during all the coffees in the noon and lunches. Besides education, during the studies I gained a few great friends, so special thanks goes to Mateja, Shahid and Martina. As Martina said already, we learned together, we "suffered" together, we laughed together. I also have to thank Maja for all the coffees that waited for me in the mornings and helped me start the day. And thanks to my last "office-mates" from office E58 Vanja, Sara and Sandra; thanks for all the questions and waiving over monitors.

And, of course, at the end, I have to say thanks to my family, my Mom and Dad, sister and big brother, and to my closest friends, my other family: Jeca, Jovana (Super sikret super group) and Stanislava and Maki (AAA). Without them I would not have accomplished so many great things in my life. They made me who I am today, and without their support and encouragement I would not be able to do great things in my life, and just one of them is finishing my PhD studies. Although they were not physically close, they were there for me during all four years of my doctoral studies and I will always be gratefully thankful.

Abstract

In nature, minerals are often exposed to significant changes in physical and geochemical conditions that lead to the formation of structural intergrowths through the topotaxial reactions. During progressive recrystallization, the precursor mineral is transformed into more stable phases. The topic of the thesis is a topotaxial transformation of ilmenite to hematite and rutile where oriented transformation is possible since all three minerals (ilmenite, rutile and hematite) have a common oxygen sublattice which is controlling the orientation relationship between these minerals. The topotaxial transformation was studied on two groups of samples; first are the rutile and hematite intergrowths from Mwinilunga, Zambia; the second part of the thesis is discussing the transformation of ilmenite single crystal from Zagi Mountain, Pakistan, to rutile and hematite during oxidation in air.

In the thesis I studied mechanisms of ilmenite transformation to rutile and hematite at the atomic-scale. For investigating structural transformation during topotaxial transformations I used X-ray powder diffraction, optical microscopy, scanning and transmission electron microscopy. For complete image of structural transformation, the samples were observed in two perpendicular zone axes.

In the samples investigated in the thesis I observed two different orientation relationships. The crystallographic orientation relationship between rutile and hematite in samples from Zambia is determined to be $<101>\ \{010\}_{R}\ ||\ <210>\{001\}_{H}$ (OR-2). On the other hand, ilmenite samples heated in air show different orientation relationship described by $<001>\{010\}_{R}\ ||\ <210>\{001\}_{I}$ (OR-1). The mechanism of transformation includes initial oxidation of Fe^{2+} in ilmenite to Fe^{3+} and its diffusion to the surface that triggers exsolution of Ti ions within the parent ilmenite structure to form rutile lamellae. The diffusion of iron is controlled by the activity of oxygen. When the oxygen is readily available for the oxidation of Fe^{2+} to Fe^{3+}, diffusion is fast; on the other hand if activity of oxygen is low, the oxidation of iron is slow. The kinetics of diffusion controls the orientation relationship. The OR-1 is formed when the diffusion is fast since the Ti cations completely inherit the ilmenite oxygen sublattice. However when the diffusion is slow, the cations have enough time to adopt energetically most favourable positions and to form tetragonally deformed rutile structure.

Different orientation relationships between rutile and hematite/ilmenite also leads to different rutile-rutile interfaces. In the case of OR-2, these interfaces could be classified into four groups: (1) symmetry-related configuration at 60° and 120°, (2) $\{101\}_{R}$ twins with incidence angles of 114.44° and their complementaries at 65.56°, (3) $\{301\}_{R}$ twins at 54.44° with complementaries at 125.56° and (4) low-angle tilt boundaries at 174.44° and 5.56°. On the other hand, OR-1 leads only to symmetry-related rutile-rutile contacts at 60° and 120°.

Povzetek

V naravi so minerali po kristalizaciji pogosto izpostavljeni različnim spremembam fizikalnih in geokemičnih pogojev, ki vodijo do nastanka novih, strukturno koreliranih, produktov. Odvisno od poteka reakcije novonastale faze kristalizirajo v jasno definiranih kristalografskih odnosih, ki jih pogosto imenujemo topotaksialni odnosi. Pri tej vrsti faznih transformacij gre za progresivno rekristalizacijo začetnega minerala v stabilnejše nove produkte, med katerimi se ohranja strukturna soodvisnost v vseh treh dimenzijah.

Tema moje doktorske naloge je bil študij topotaksialne transformacije ilmenita ($FeTiO_3$) v hematit (Fe_2O_3) in rutil (TiO_2). Glede na to, da imajo vsi ti minerali skupno kisikovo podmrežo, med njimi nastopajo kompleksni strukturni odnosi, ki so bili osrednja vsebina doktorske naloge. Topotaksialno transformacijo sem preučevala na dveh skupinah vzorcev; prvi del doktorske naloge se nanaša na študij naravnih vzorcev, na katerih so vidna orientirana preraščanja rutila in hematita; v drugem delu naloge pa sem topotaksialno transformacijo skušala reproducirati s termično obdelavo kristalov ilmenita v oksidacijskih pogojih. Raziskave so temeljile na študiju strukturnih in kemijskih odnosov v vzorcih od makroskopskega do atomarnega nivoja. Za preiskovanje topotaksialnih transformacij sem uporabila rentgensko praškovno difrakcijo, optično mikroskopijo, vrstično in presevno elektronsko mikroskopijo. Vzorce sem preiskovala v več nizkoindeksnih orientacijah, kar omogoča prostorsko določitev kompleksnih strukturnih odnosov.

Odvisno od kinetike oksidacijskega procesa sem v vzorcih določila dva tipa topotaksialnih orientacijskih odnosov med nastalimi fazami. Kristalografska orientacijska zveza, ugotovljena med rutilom in hematitom v naravnih vzorcih z orientiranimi preraščanji rutila in hematita, je ta odnos OR-2: $<101>\{010\}_R \parallel <210>\{001\}_H$, pri termično obdelanih monokristalih ilmenita pa je ta odnos OR1: $<001>\{010\}_R \parallel <210>\{001\}_I$. Razlog za drugačen orientacijski odnos je v kinetiki oksidacijskega procesa v primeru naravnih in termično obdelanih kristalih ilmenita. Mehanizem topotaksialne transformacije, ki je posledica oksidacije Fe^{2+} v ilmenitu do Fe^{3+}, je difuzijsko kontroliran proces, pri katerem pride do izločanja železa iz ilmenita ter posledične preureditve Ti^{4+} ionov v rutilno strukturo. Kinetika tega difuzijskega procesa nadzoruje orientacijsko zvezo; če so difuzijski procesi omejeni s hitrostjo oksidacije na površini (nizek parcialni tlak kisika), dobimo OR-2, v nasprotnem primeru, kjer je oksidacija hitra (visok parcialni tlak kisika), pa dobimo OR-1. Najbolj kompleksne orientacijske odnose opazimo takrat, ko je reakcija počasna in imajo kationi na razpolago dovolj časa, da se preuredijo v energetsko najbolj stabilno konfiguracijo pri dani temperaturi. Medtem ko pri hitri oksidaciji (OR-1) izločene rutilne domene kažejo le enostaven simetrijski odnos, povezan preko troštevne simetrijske operacije glede na kisikovo podmrežo (60° in 120°), pri počasni oksidaciji (OR-2) med kristali rutila opazimo 144 različnih kristalografskih odnosov, ki jih lahko razdelimo v štiri razrede: (1) simetrijsko odvisna konfiguracija pri 60° in 120°, (2) $\{101\}_R$ dvojčki z vpadnimi koti 114,44° ter komplementarni kontakti pri 65,56°, (3) $\{301\}_R$ dvojčki pri 54,44° ter komplementarni kontakti pri 125,56° in (4) nizkokotne meje pri 174,44° ter 5,56°.

Contents

Acknowledgments **vii**

Abstract **ix**

Povzetek **xi**

Contents **xiii**

List of Figures **xv**

List of Tables **xvii**

Abbreviations **xix**

Symbols **xxi**

1 Introduction **1**
1.1 Topotaxial Reactions in Crystalline Solids 1
1.2 Phase Relations in the FeO-Fe_2O_3-TiO_2 System 3
1.3 Ilmenite-Hematite Solid Solution Series 10
1.4 Exsolution Textures in Rhombohedral Fe-Ti Oxides (Ilmenite/Hematite) 13
1.5 Oxidation of Ilmenite and Formation of Rutile Intergrowths with Hematite and Ilmenite 15
1.5.1 Oxidation of ilmenite under natural conditions 16
1.5.2 Oxidation of ilmenite for the production of TiO_2 16
1.5.3 Crystallographic orientation relationships in the ilmenite-hematite-rutile system 17

2 Experimental Methods **21**

3 Oriented Rutile/Hematite Intergrowths from Mwinilunga, Zambia **25**
3.1 Specimen Description and XRD-Phase Analyses 25
3.2 Textural Characterization of the Intergrowths by Optical Microscopy and SEM 26
3.3 Crystallography of Rutile/Hematite Intergrowth Structures 29
3.4 Exsolution Processes in the Rutile/Hematite Intergrowths 35
3.5 Mechanism of Formation of Oriented Rutile/Hematite Intergrowths 36

4 Topotaxial Transformation of Ilmenite Single Crystal During Oxidation in Air **43**
4.1 Characterization of the Starting Sample and Experimental Procedure 43
4.2 Phase Composition of the Heated Ilmenite Samples 44
4.3 Microstructure Characterization of Heated Ilmenite Along $[001]_I$ 47
4.4 Characterization of Surface Layer 51

4.5 Microstructure Characterization of Heated Ilmenite Along $[110]_I$ 52
4.6 Mechanism of Topotaxial Transformation of Heated Ilmenite 53

5 Conclusions **59**

References **61**

Bibliography **69**
Publications Related to the Thesis 69
Journal Articles 69
Conference Papers 69

Biography **71**

List of Figures

Figure 1.1: Schematic presentation of topotaxial and epitaxial reactions. 3
Figure 1.2: Schematic phase diagram of the FeO-Fe_2O_3-TiO_2 ternary system 4
Figure 1.3: Hematite crystal structure. 5
Figure 1.4: Rutile crystal structure. 7
Figure 1.5: Comparison of ilmenite, hematite and rutile structures....9
Figure 1.6: Typical morphology of ilmenite crystal 9
Figure 1.7: Phase diagram for the hematite-ilmenite (Fe_2O_3-$FeTiO_3$) solid solution....11
Figure 1.8: Log $fO2$- T diagram showing the stability of different oxidation states of iron (Frost, 1991). 12
Figure 1.9: $fO2$ -T for magnetite-ulvöspinel$_{ss}$ and hematite-ilmenite$_{ss}$. 14
Figure 1.10:Exsolution texture observed in hemo-ilmenite from Allard Lake region of Quebec 15
Figure 1.11: Rutile lamellae in oxidized ilmenite from Ecstall pluton, British Columbia, Canada 17
Figure 1.12:Schematic presentation of ilmenite oxidation mechanism. 18
Figure 1.13:Schematic presentation of two orientation relationships between corundum type structure (black arrows) and rutile (red arrows) 19
Figure 2.1: TEM images of grinded samples 23
Figure 3.1: Oriented intergrowths of rutile and hematite from Mwinilunga, Zambia. 26
Figure 3.2: Rutile/hematite intergrowths under polarized light microscope. 27
Figure 3.3: SEM images of sample observed from $[001]_H$ direction. 28
Figure 3.4 BSE/SEM images of the sample observed from $[100]_H$ direction....29
Figure 3.5: $(101)_R$ rutile twin in hematite matrix viewed along $[001]_H$....30
Figure 3.6: TEM analysis of rutile lamellae in hematite matrix viewed along the $[001]_H$ 32
Figure 3.7: HRTEM analysis of the low-angle grain boundary and the rutile/hematite interface. 33
Figure 3.8: TEM analyses of rutile/hematite intergrowths viewed along $[100]_H$ projection36
Figure 3.9: Hematite exsolutions in rutile viewed along $[010]_R$ 37
Figure 3.10:Schematic presentation of mechanism of transformation of rutile/hematite intergrowths from Mwinilunga, Zambia....39
Figure 3.11:Schematic presentation of cation rearrangement in the ilmenite lattice during oxidation. 41
Figure 4.1: Ilmenite single crystal from Zagi mountain, Pakistan. 44
Figure 4.2: XRD diagrams of untreated ilmenite and samples heated at different temperatures from 600-1000 °C for 12 hours. 45
Figure 4.3: XRD diagrams of untreated ilmenite and samples heated at 800 °C for 1, 12 and 100 hours 46
Figure 4.4: SEM/BSE images of samples heat-treated at different temperatures (600-1000 °C) for 12 hours 48
Figure 4.5: SEM/BSE image of rutile lamellae in ilmenite and pseudobrookite 48

Figure 4.6: Low-magnification TEM analyses of rutile lamellae in the 800 °C/12h sample observed in $[001]_I$ 49
Figure 4.7: Transitional rutile-type phase at the recrystallization front observed in the sample 800 °C/12h 50
Figure 4.8: EELS analyses of Ti-L_{32} edge in ilmenite, transitional zone and rutile. 50
Figure 4.9: SEM images of surface oxide layer of samples heated for 12 hours at temperatures from 700 to 1000 °C. 51
Figure 4.10: Rutile lamellae in the 800 °C/100h sample viewed along $[110]_I$. 53
Figure 4.11: The mechanism of exsolution processes during oxidation of ilmenite under 800 °C. 56

List of Tables

Table 3.1: List of all possible rutile-rutile configurations forming during impingement of rutile lamellae according to the OR-2 law. 31
Table 3.2: Temperature dependence of lattice misfit (δ) for different interfaces. 42
Table 4.1: EDS analyses of starting ilmenite sample. 45
Table 4.2: Oxidation rates of the ilmenite single crystal heated at different temperatures and for different times. 46
Table 4.3: TEM/EDS analyses of composition in parent ilmenite, rutile and secondary ilmenite'. 52

Abbreviations

OR	... Orientation relationship
hcp	... Hexagonal close packing
ccp	... Cubic close packing
QIF	... Quartz-iron-fayalite buffer
FMQ	... Fayalite-magnetite-quartz buffer
MH	... Magnetite-hematite buffer
Ilmenite-hematite$_{ss}$	... Ilmenite-hematite solid solution
Ulvöspinel-magnetite$_{ss}$	... Ulvöspinel-magnetite solid solution
CS	... Crystallographic shear
XRPD	... X-ray powder diffraction
SEM	... Scanning electron microscopy
SE	... Secondary electrons
BSE	... Backscattered electrons
EDS	... Energy-dispersive spectroscopy
FEG	... Field emission gun
TEM	... Transmission electron microscope
SAED	... Selected area electron diffraction
HRTEM	... High-resolution electron microscope
STEM	... Scanning transmission electron microscope
HAADF	... High angular annular dark-field
EELS	... Electron energy loss spectroscopy
FFT	... Fast Fourier transform
IVCT	... Intervalence charge transfer

Symbols

f_{O_2} ... Oxygen fugacity
Φ ... Angle between the c-axes of rutile domains
Δ ... Lattice misfit
D ... Vernier period of a misfit
R_{ox} ... Oxidation rate

Chapter 1

Introduction

1.1 Topotaxial Reactions in Crystalline Solids

Topotaxial reactions are structurally controlled transformations of a parent phase into one or more products in a well-defined orientation relationship (OR). The newly formed phases contain information about the thermodynamics and chemical conditions during the transformation.

Oriented transformations were first mentioned by Bernal (1957) as "solid state transformations that proceed by a minimum rearrangement of the structures of single crystals, involving little more than a mechanism of dislocation glides, such as produce stacking faults and twinning". Lotgering (1959) proposed the most widely accepted definition, where topotaxial reactions are described as "chemical solid state reactions that lead to a material with crystal orientations which are correlated with crystal orientations in the initial product". Bernal (1960) later pointed out that the majority of the atomic positions in the original and transformed phases are substantially the same. Dent Glasser, et al. (1962) referred to topotaxy as the most ordered type of pseudomorphs; a pseudomorph is a single crystal which is transformed to one or more products while the morphology of the crystal stays intact. In the case of pseudomorphs, the newly formed phases can have a different degree of orientation relationship with the parent mineral (or between new formed phases). The pseudomorphs with the highest degree of orientation are topotaxial transformations. That is why in the topotaxial transformation, one or more products of the transformation must have a definite crystallographic orientation with respect to the original crystal. Dent Glasser, et al. (1962) also added the necessity of three-dimensional similarity between parent and product structures since the topotaxial reactions occur throughout the entire crystal. Shannon and Rossi (1964) suggested that there are different degrees of topotaxy; low-degree and high-degree topotaxial reactions. For example, the anatase-rutile transformation is an intermediate topotaxial transformation; during transformation $\{112\}_{\mathrm{A}}$ oxygen planes in anatase are converted in $\{100\}_{\mathrm{R}}$ oxygen planes in rutile, while Ti atoms are rearranging. Although there is the orientation relationship between rutile as a new phase and anatase as a starting phase, there is no preservation of anatase axes of symmetry (Shannon & Pask, 1964). On the other hand, the lepidocrocite (γ-FeOOH)-maghemite (γ-Fe_2O_3) transformation is nearly perfect topotaxy, since only hydroxyl groups and hydrogen atoms are removed from the

structure resulting in a perfect single crystal diffraction of the newly formed phase (Bernal, et al., 1957; Mackay, 1960).

Topotaxial transformation reactions are dictated by the structure of the parent phase in three dimensions, therefore common structural features between the parent and the product phase must be present. This is the main difference between topotaxial and epitaxial reactions, where a new phase grows on the top of the matrix phase. The matrix phase remains intact and only acts as a substrate for oriented nucleation and growth of the product (Figure 1.1). Epitaxially related phases must have common structural features in two dimensions (Shannon & Rossi, 1964), whereas in topotaxial transformations, structural coherence in three dimensions is required.

All topotaxial reactions have a crystallographic and a chemical aspect. From the crystallographic point of view, most of the atomic positions are preserved during a topotaxial transformation, while the main crystal axes or planes transform into the crystal axes or planes of the newly formed phase or phases. The unit cell of a newly formed phase has similar dimensions as the unit cell of the parent phase, but it can have different crystal symmetry. Fourfold axis of tetragonal structure, for example, can transform to the twofold axes of the newly formed cubic phase (Bernal & Mackay, 1965); whereas the [111] axis of the parent cubic cell can become the [001] axis of new trigonal phase (Bernal, et al., 1957). From the chemical point of view, topotaxial transformations involve loss or gain of atoms through diffusion processes. Diffusion processes may occur either in the cation or anion sublattice of the matrix phase. This depends on the size and electronegativity of the cations (Dent Glasser, et al., 1962). In oxides with small cations (e.g., Mg^{2+}, Al^{3+}, Fe^{3+}, Si^{4+}), the oxygen framework remains intact and cations diffuse. On the other hand, large and more electronegative cations (e.g. U^{4+}, Pb^{4+}) remain in their positions and the anions diffuse. Large electropositive cations (e.g., Ca^{2+}) represent an intermediate case, where both, cations and anions, can change their atomic positions (Dent Glasser, et al., 1962).

According to Dent Glasser, et al. (1962), factors that influence the orientation relationship between the parent and the newly formed phase in topotaxial reactions include temperature, pressure, physical state and specific experimental conditions such as time and rate of heating used to induce the changes. Therefore, it is very important to understand thermodynamic conditions that lead to the formation of different phases during topotaxial reactions.

A typical example of a topotaxial reaction is the oxidation of ilmenite, where ilmenite transforms to rutile and hematite in an oriented manner. This is possible because all three minerals have a common hexagonal closed packed (*hcp*) oxygen sublattice. The ilmenite contains iron in a divalent form, which is not stable under oxidizing conditions and its oxidation to trivalent state triggers transformation of ilmenite ($Fe^{2+}TiO_3$) to hematite ($Fe^{3+}{}_2O_3$) and rutile (TiO_2). The orientation relationships formed during transformation, as well as the mechanism of transformation, will be the subject of the thesis.

In the first part of the thesis, natural rutile/hematite intergrowths from Mwinilunga, Zambia, will be characterized down to the atomic scale in order to determine the rutile/hematite OR and reconstruct the formation mechanism of these samples. In the second part, results on the conversion of a natural ilmenite single crystal from Zagi Mountain, Pakistan to rutile and hematite during heat treatment in air will be presented. In both cases, the transformation is topotaxial, resulting in the orientation relationship between ilmenite (or hematite) and rutile. In two cases that will be presented, different relationships are observed, and the reasons for their formation will be discussed.

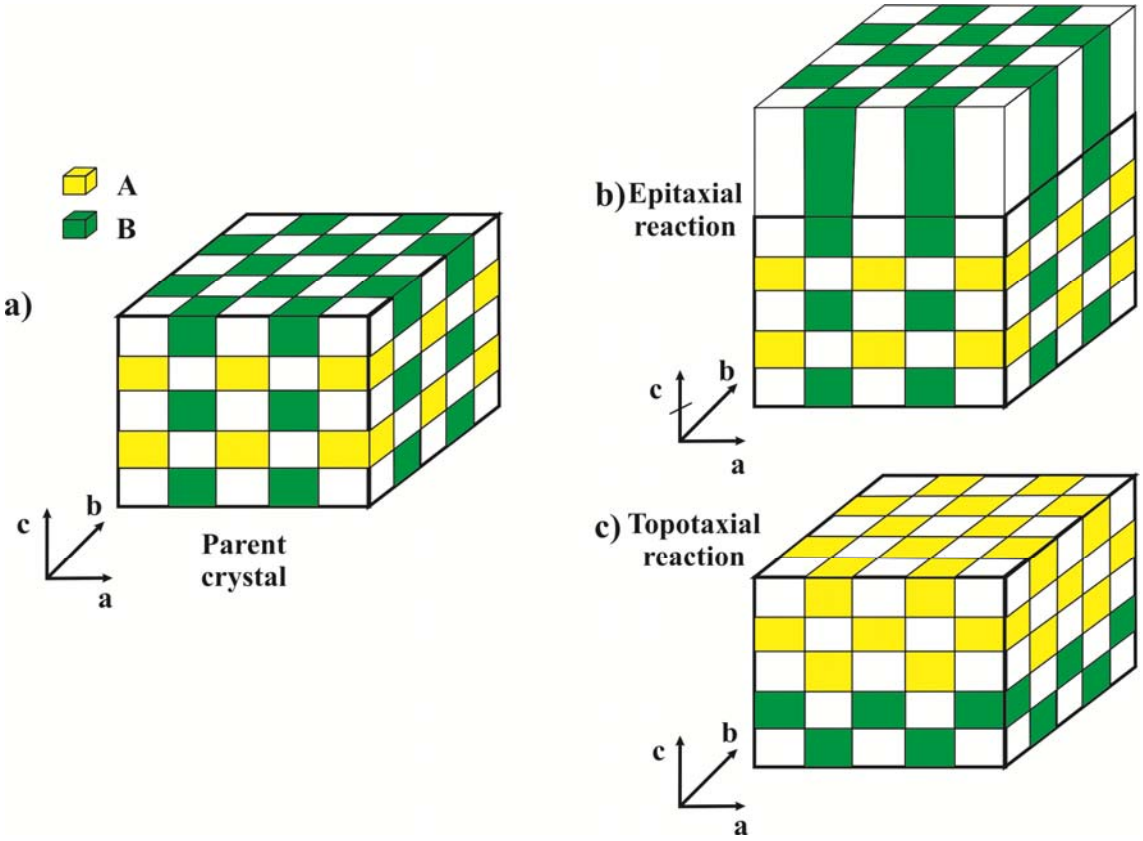


Figure 1.1: Schematic presentation of topotaxial and epitaxial reactions. a) Starting crystal, where green and yellow cubes represent two different types of atoms. b) In epitaxial reaction a new phase grows on the top ("epi") of the parent crystal (matrix) and the two phases have common features along two directions (a and b axis, 2D). c) Topotaxial reaction, where the similarity between the starting phase and the product is in all three directions (a,b and c axis, 3D).

1.2 Phase Relations in the FeO-Fe_2O_3-TiO_2 System

Rutile, hematite and ilmenite belong to a wider group of Fe-Ti oxides and relations between minerals in this system can be schematically presented within the FeO-Fe_2O_3-TiO_2 ternary diagram presented in Figure 1.2 (Lindsley, 1962). The three end-phases of this system are iron-II-oxide (wüstite), iron-III-oxide (hematite) and the titanium-dioxide (rutile, anatase or brookite). Beside single oxides of iron or titanium, the main phases of this ternary system are mixed oxides: ulvöspinel (Fe_2TiO_4), ilmenite ($FeTiO_3$) and ferropseudobrookite ($FeTi_2O_5$) as oxides with divalent iron; pseudobrookite (Fe_2TiO_5) with trivalent iron and magnetite (Fe_3O_4) as mixed oxide of divalent and trivalent iron. Beside the single phases, three solid solution series exist in this system; the ulvöspinel (Fe_2TiO_4) magnetite (Fe_3O_4), the ilmenite ($FeTiO_3$) hematite (Fe_2O_3) and the feropseudobrookite ($FeTi_2O_5$) pseudobrookite (Fe_2TiO_5) series. In the next chapter, the main phases of this ternary diagram will be described, as well as crystal structures of the most relevant phases to this thesis: ilmenite, hematite and rutile.

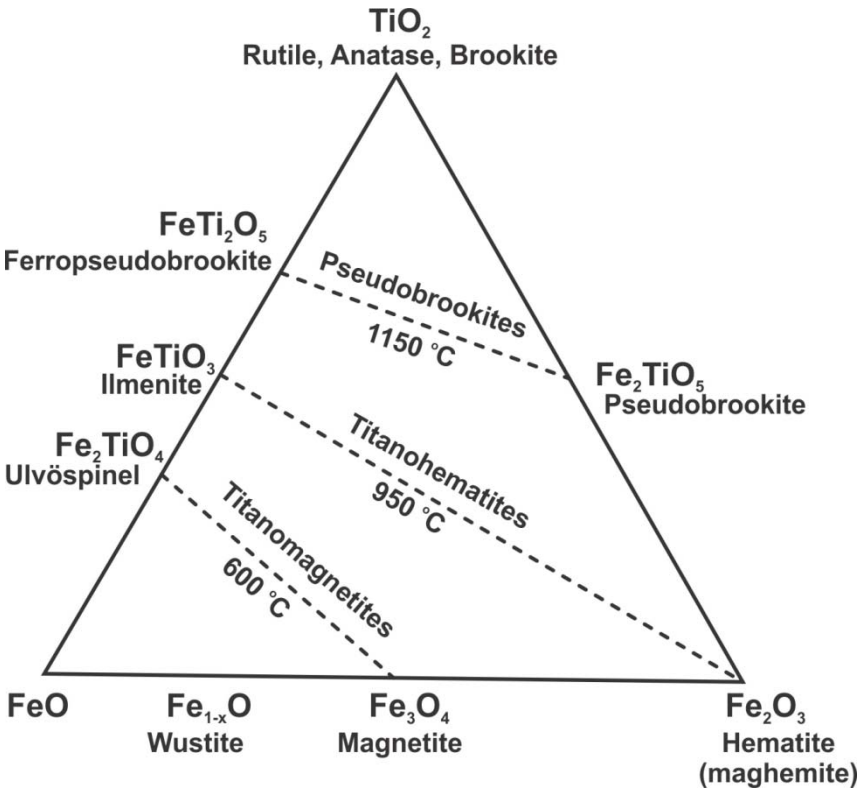


Figure 1.2: Schematic phase diagram of the FeO-Fe_2O_3-TiO_2 ternary system (Lindsley, 1962). The main phases are wüstite ($Fe_{1-x}O$), hematite (Fe_2O_3) and rutile (TiO_2) in the corners of the diagram. Three solid solution series are presented: Fe_2TiO_4-Fe_3O_4 (titanomagnetites), $FeTiO_3$-Fe_2O_3 (titanohematites) and $FeTi_2O_5$-Fe_2TiO_5 (pseudobrookites), and the regions of the existing phases in equilibrium depending on the composition of the main phases. Temperatures of complete solid solutions are written on their tie-line.

Wüstite ($Fe_{1-x}O$) is an iron oxide with the highest content of the divalent iron. It has the rock-salt structure, where oxygen atoms are arranged in a cubic close packing (*ccp*) with the divalent iron cations in the octahedral coordination sites. It is rarely stoichiometric and usually has vacancies on the Fe sites and electroneutrality is achieved by partial substitution of Fe^{2+} with Fe^{3+} (Roth, 1959). It is stable at temperatures above 570 °C and at very low oxygen fugacities f_{O_2} (oxygen partial pressures). It has a high affinity to react with SiO_2 to form silicates (Lindsley, 1991) and therefore it is very rarely found in nature as an oxide phase.

Hematite (Fe_2O_3) is the iron -III- oxide that has the rhombohedral corundum-type structure (Lee & Lagerlof, 1985) with the $R\bar{3}c$ space group and cell parameters a,b=5.038 Å and c=13.772 Å (Blake, et al., 1966). In contrast to wüstite, it has a hexagonally close packed oxygen sublattice, with individual oxygen layers stacked in ABAB sequence along the c-axis. Oxygen layers extend in the basal plane where chains of oxygen atoms intersect at 60°. In each layer, iron cations occupy 2/3 of the octahedral interstitials forming a regular pattern (Figure 1.3a). Since 2/3 of octahedral positions are occupied by iron cations, 1/3 of the positions is presented with the vacancies. Because of the present vacancies, the diffusion in hematite is faster perpendicular to the c-axis

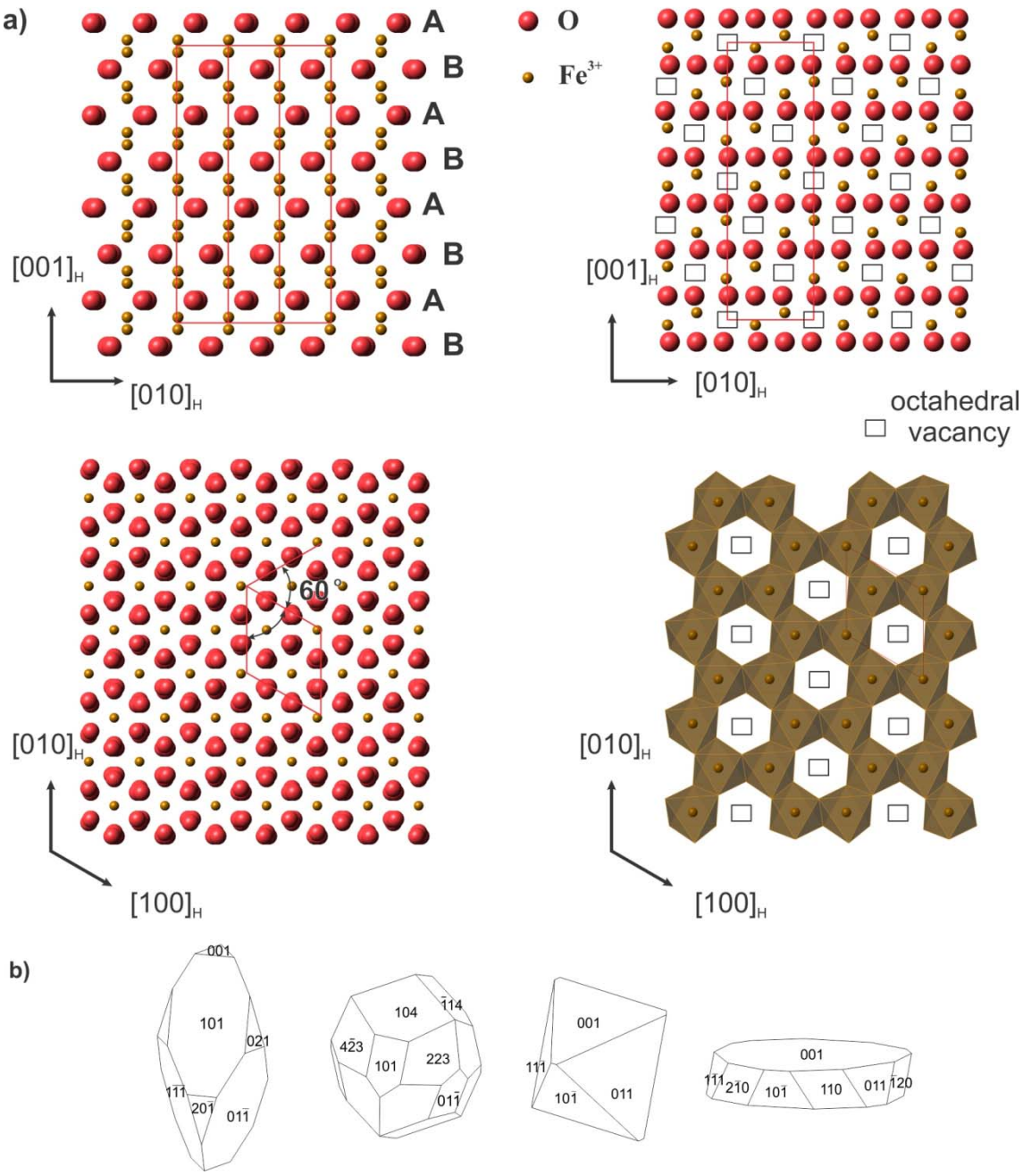


Figure 1.3: Hematite crystal structure. a) Atomic models of hematite structure in three different orientations presenting the hexagonal close packing (ABAB sequence), occupancy of 2/3 of octahedral positions and 60° angle between oxygen chains in the layer. Polyhydric model of one basal plane shows the 2/3 occupancy of octahedral positions (Blake, et al., 1966). b) Typical morphologies of hematite crystals (Palache, et al., 1952).

of hematite for several orders of magnitude (Sabioni, et al., 2005). Adjacent octahedral layers are related to each other by inversion through the centre of horizontal faces and 60° rotation of the layer around any 3-fold vertical axis (Blake, et al., 1966). Half of the octahedra in one layer share a face with the upper adjacent layer, and the other half with

the layer below. All layers are related to each other by c-glide plane parallel to the (001) (Harrison, et al., 2000; Lindsley, 1976; Waychunas, 1991).

Hematite is found in discrete grains and intergrowths with ilmenite in igneous rocks, formed in the late magmatic crystallization stage between 800 and 1050 °C; at lower temperatures between 500 and 600 °C it is found in the form of ilmenite-hematite intergrowths. It is very common in hydrothermal and pneumatolytic ores (Bowles, et al., 2011; Ramdohr, 1979). Morphology of hematite crystals depends mainly on the formation temperature. In igneous rock when it is formed at higher temperatures it has the form of thick crystals, while at lower temperatures and in hydrothermal stage it forms tabular crystal after (001) (Figure 1.3b) (Palache, et al., 1952; Ramdohr, 1979).

Titania (TiO_2) mainly occurs in three different polymorphs in nature: rutile, anatase and brookite. Furthermore, there are additional high-pressure polymorphs. α-PbO_2 crystallizes in the orthorhombic crystal system and is found in nature in rocks which formed at high pressures of 5-7 GPa; at even higher pressures of 12-17 GPa TiO_2 polymorph with the baddeleyite structure is stable and it crystallizes in the monoclinic system. The fifth polymorph has the tetragonal hollandite-type structure and is highly metastable. TiO_2 polymorphs with baddeleyite and hollandite type structure are found only as synthetic polymorphs. There are two more high-pressure polymorphs; at pressures over 37.4 GPa the stable phase has a cotunnite structure and at pressures higher than 60GPa is a cubic phase and its structure is still not determined (Meinhold, 2010; Zhu & Gao, 2014).

Rutile is the most stable and hence the most widespread polymorph of TiO_2. The rutile structure is shown in Figure 1.4. Rutile has a tetragonal structure, it crystallizes in the space group $P4_2/mnm$ with cell parameters a=4.5937 Å and c=2.9587 Å (Howard, et al., 1991). Similar as in hematite, the oxygen sublattice of rutile may be described as hexagonal close packed but with a slight tetragonal deformation along the a and b axis. Because of tetragonal deformation one of the oxygen chains is straight and parallel to c-axis, while two undulating chains are parallel to <101> and they intersect with the c-axis at 57.22° (Figure 1.4a). The Ti^{4+} cations occupy 1/2 of the octahedral positions forming characteristic chains of edge-shared Ti-octahedra along the c-axis. Full chains are connected by corner-sharing to four surrounding chains parallel to [010] and [100] (Hyde, 1976). Full and empty chains alternate along the c-axis. Empty chains may also be interpreted as chains of vacancies that serve as fast diffusion paths for ions and therefore the diffusion of different ions in rutile is highly anisotropic; diffusion parallel to c-axis is for several magnitudes faster (Sasaki, et al., 1985; Steele & McCartney, 1969; Wittke, 1966). For diffusion of different ions in rutile, the charge of the ion is more important than the size. Although the divalent cations can have bigger radius than some trivalent cations, they can be displaced to the interstitial positions much easier because the same position is energetically less favourable for trivalent cations. Divalent cations diffuse rapidly along the c-axis by interstitial mechanism, while the trivalent cations involve simultaneous motion of titanium ions and the diffusing cations. In the case of mixed valence cations, such as Fe and Mn, they diffuse along c-axis of rutile in both divalent and trivalent state (Sasaki, et al., 1985).

Rutile is found in all types of rocks, but usually in very small amounts. It is more abundant in pegmatites and metamorphic ore bodies, while in hydrothermal stage it is usually formed from ilmenite in wallrock (Ramdohr, 1979). Typical morphology of rutile crystals is elongated in c-axis direction and pyramidal (Figure 1.4 b). Very often rutile is forming twins where the twinning planes are (101) or (301). The characteristic angle between c-axis of rutile individuals for $\{101\}_R$ twins is 114.4° and for $\{301\}_R$ 54.7°

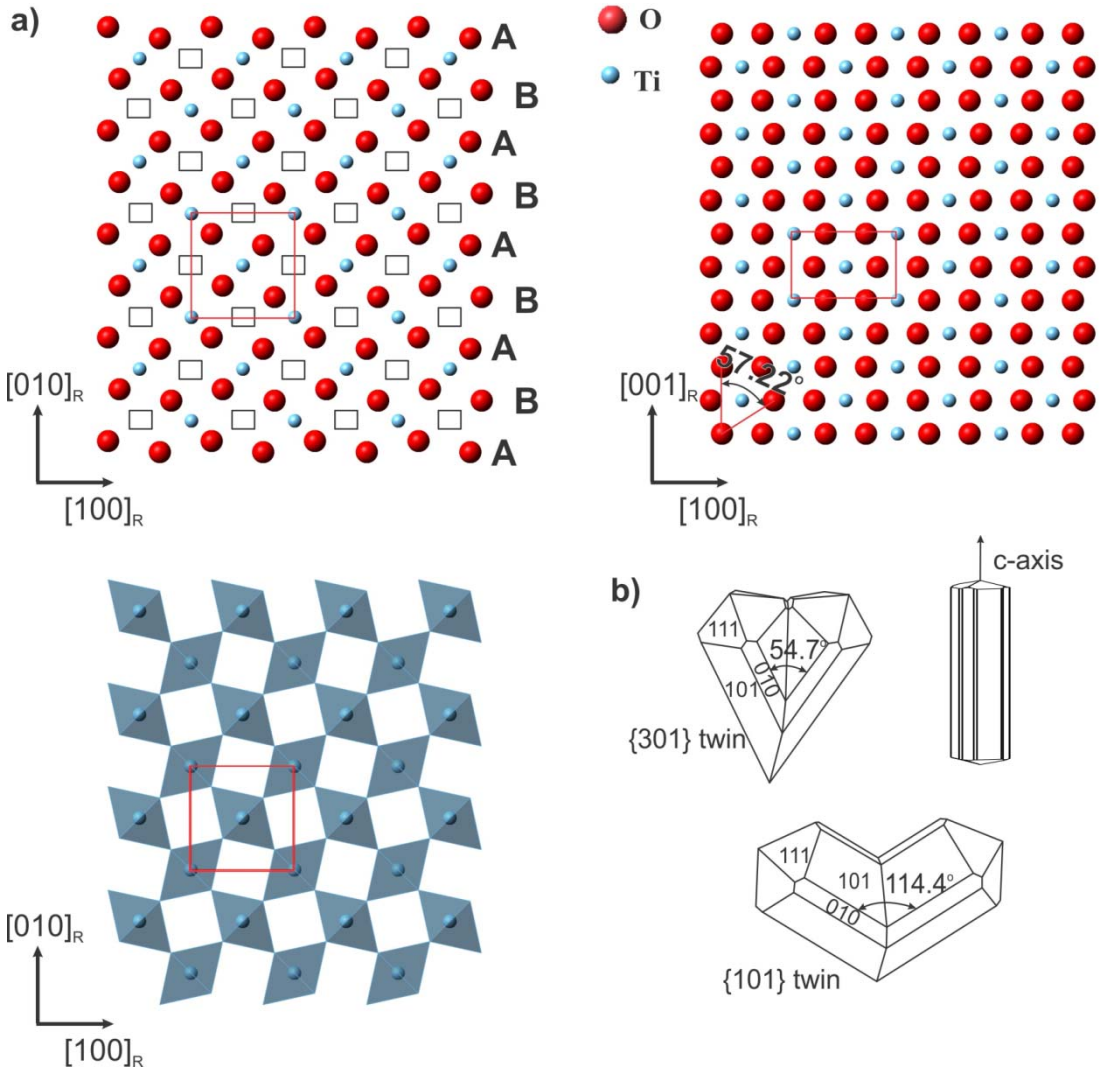


Figure 1.4: Rutile crystal structure. a) Observed from [001] zone axis, the hexagonal close packing of oxygen is observed. The polyhedral model shows the occupancy of 1/2 of octahedral positions with Ti and empty channels for cation diffusion in the direction of c-axis. (Howard, et al., 1991) b) typical morphologies of rutile crystals (Palache, et al., 1952).

(Lee, et al., 1993). In natural samples very often both types of twins are found together in the form of 2D sagenitic structure (Daneu, et al., 2014; Force, et al., 1996; Palache, et al., 1952).

FeO-Fe_2O_3 join. The intermediate phase at the wüstite - hematite binary join is magnetite (Fe_3O_4) (see Figure 1.2). It contains both, divalent and trivalent iron atoms and its formula may also be written as $Fe^{3+}{}_2O_3 \cdot Fe^{2+}O$. Magnetite has the inverse spinel structure, where the Fe^{2+} cations lie in the octahedral and the Fe^{3+} cations occupy both the tetrahedral and octahedral positions (Fleet, 1981). There is no solid solubility between wüstite ($Fe_{1-x}O$) and magnetite (Fe_3O_4), but limited solubility exists between magnetite and hematite at high temperatures. Below 600°C, oxidation of magnetite leads to the formation of hematite through the metastable solid solution of hematite and maghemite (γ -Fe_2O_3) (Lindsley, 1991).

TiO_2-FeO join. There are three main intermediate phases at this binary join: ulvöspinel, ilmenite and "ferropseudobrookite" which all contain divalent iron (Figure 1.2) and do not form solid solutions. Ferropseudobrookite ($FeTi_2O_5$) is rare in nature and is stable only above 585 °C (Lindsley, 1991). Ulvöspinel (Fe_2TiO_4) is a mixed oxide and has the inverse spinel structure with Ti^{4+} in octahedral positions and one half of Fe^{2+} is in tetrahedral while the other half is in the octahedral positions (Bosi, et al., 2009). The ulvöspinel oxidizes during subsolidus cooling of magma and transforms to magnetite with ilmenite lamellae (Buddington & Lindsley, 1964).

Ilmenite ($FeTiO_3$) is isostructural with hematite, it has the rhombohedral corundum-type structure (space group $R\bar{3}$) with the cell parameters a,b=5.0884 Å and c=14.0855 Å (Figure 1.5). The common feature of ilmenite and hematite structure is the extension of oxygen layers in the basal plane, where oxygen chains intersect at 60° (Figure 1.5a). When compared to oxygen chains in rutile, there is an angular difference of 2.78°, since the oxygen layers in rutile intersect at 57.22° (Figure 1.5b). On the other hand, the main difference between hematite and ilmenite structure is that in ilmenite, layers of octahedrally coordinated Fe^{2+} and Ti^{4+} atoms alternate along the c-axis (Figure 1.5c), ordering along threefold axis as -Fe-Ti-v-Ti-Fe- (-Ti-Fe-v-Fe-Ti-) resulting in the loss of the c-glide plane that exists in hematite (which contains only Fe^{3+} cations). Since the ilmenite has corundum type structure, 2/3 of octahedral positions are occupied by Fe^{2+} and Ti^{4+}, while in the rutile only 1/2 of the octahedral positions are occupied by Ti^{4+}(Figure 1.5d). Along the c-direction of ilmenite, each octahedron shares one face with the octahedron of the other type while on the other face there is a vacant octahedron (v). Octahedron edges are shared in basal plane between the cations of the same type (Wechsler & Prewitt, 1984; Wilson, et al., 2005).

Ilmenite occurs in all igneous rocks (intrusive and extrusive) and their pegmatites, and rarely in hydrothermal deposits. It is very resistant to weathering, therefore it is frequently found in sedimentary rocks and very often it is concentrated in beach sand (Bowles, et al., 2011). In regional metamorphic rocks it is transformed to rutile and hematite by oxidation (Brownlee, et al., 2010). Typically it occurs in thick tabular crystal with well-developed basal planes, and very often has acute rhombohedral forms (Figure 1.6) (Palache, et al., 1952; Ramdohr, 1979).

TiO_2-Fe_2O_3 join. The only phase of this join (see Figure 1.2) is the high-temperature pseudobrookite (Fe_2TiO_5) that has orthorhombic structure (Guo, et al., 1999). The majority of natural pseudobrookite is formed through the reaction of ilmenite and hematite or their solid solutions above 1000 °C (Ramdohr, 1979).

There is no significant solid solubility between rutile, hematite and pseudobrookite as the phases of this join. In the TiO_2 corner of a diagram there is an area representing the phase stability of rutile with ~6% Fe_2O_3 and FeO (Lindsley, 1991; Taylor, 1964). The solid solubility of iron in rutile depends on the temperature, and at 800 °C it is up to 1 cation % going up to 3 cation % at 1350 °C. Below 700 °C Fe is practically immobile in rutile structure (Wittke, 1967). The precipitation of Fe from rutile starts in the form of Guinier-Preston zones, coherent precipitates with the monoclinic structure. The structures of the rutile and the first formed precipitates are considerably different, but the two phases are still coherent. Further growth of Fe-rich phase proceeds with the formation of hematite as the equilibrium precipitate (Putnis, 1978).

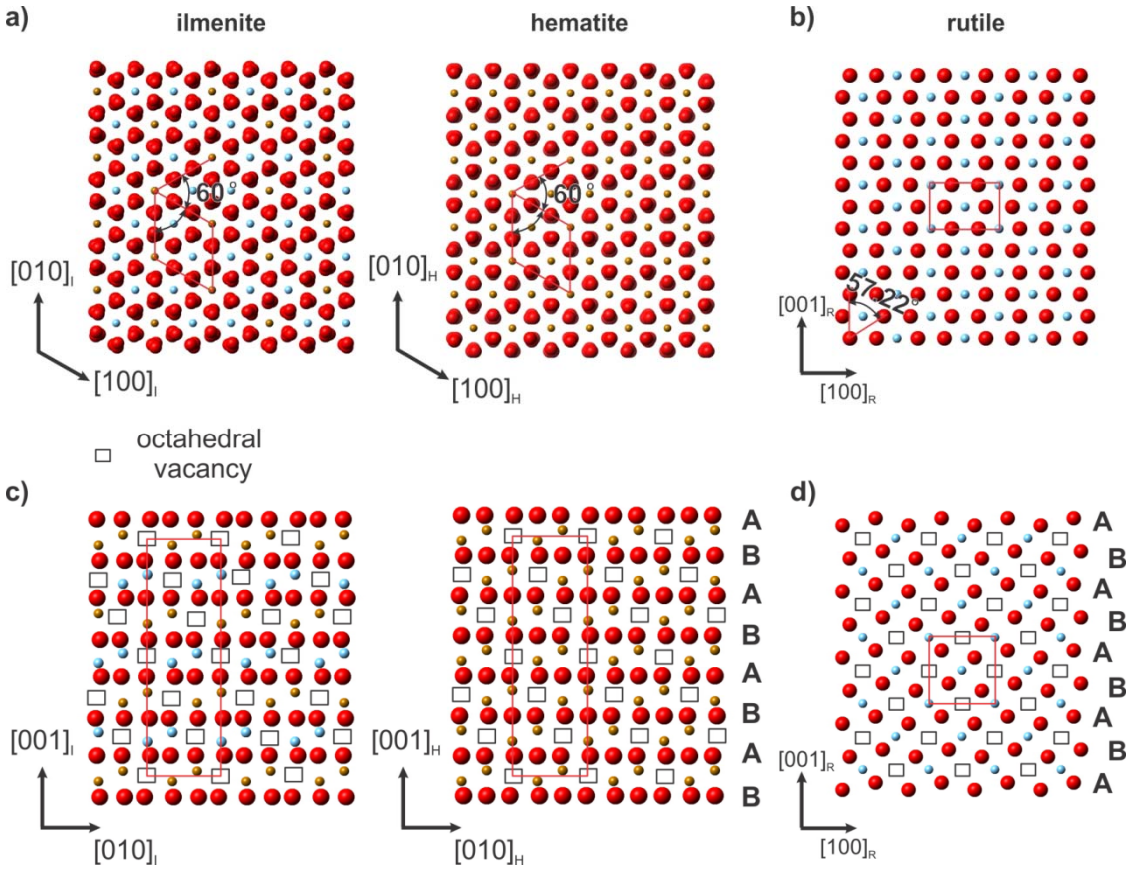


Figure 1.5: Comparison of ilmenite, hematite and rutile structures a) Oxygen chains in corundum type structure are intersecting at 60°. b) In rutile structure oxygen chains are intersecting at 57.22°. c) In corundum type structure 2/3 of octahedral positions are occupied; in ilmenite structure, octahedral positions are occupied by the alternating Fe^{2+} and Ti^{4+} layers along the c-axis (Wechsler & Prewitt, 1984), while in the hematite all octahedral positions are occupied by Fe^{3} (Blake, et al., 1966). Both hematite and ilmenite have *hcp* oxygen sublattice. d) In rutile structure the oxygen sublattice is slightly tetragonally deformed and only 1/2 of octahedral positions are occupied by titanium cations (Howard, et al., 1991).

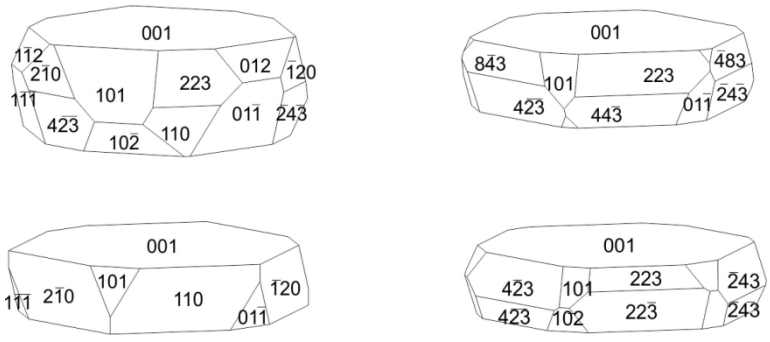


Figure 1.6: Typical morphology of ilmenite crystal. Ilmenite crystals are usually tabular with different combinations of crystal planes (Palache, et al., 1952).

Three additional binary joins exist within the FeO-Fe_2O_3-TiO_2 system at the edges of the ternary phase diagram, and all of them show complete solid solubility between the end-phases at higher temperatures:

- the cubic magnetite-ulvöspinel series, also referred to as the β-series or the spinel phase series where the solid solubility is complete already at 600 °C (Lindsley, 1962, 1963);
- the rhombohedral hematite-ilmenite series, also referred to as the α-series or rhombohedral phase with a limited solubility at lower temperatures, but complete solubility at 950-1050 °C (Lindsley, 1962);
- the orthorhombic pseudobrookite - "ferropseudobrookite" series, also referred to as the ω-series where complete solid solubility exists at 1150 °C (Lindsley, 1962, 1963; Verhoogen, 1962).

From a chemical perspective, substitutions in these solid solution series are always identical: one divalent iron and one titanium are substituted for two trivalent irons in order to preserve the electroneutrality of the system: $Fe^{2+} + Ti^{4+} = 2Fe^{3+}$. All phases often contain a low percentage of impurity elements; the most common being Mg and Mn. The presence of different impurities can affect ordering of the cations and the equilibrium temperatures for solid solutions. The content of Mg and Mn is always higher in the spinel series than in the rhombohedral series varying from 2-5 wt% and decreasing with temperature. (Buddington & Lindsley, 1964; Ghiorso & Sack, 1991). Structure of the ilmenite-rich solid solution is more ordered when Mn or Mg are incorporated; as a result equilibrium temperature of ilmenite-rich solid solution is lowered (Ghiorso, 1990; Toplis & Carroll, 1995).

The ilmenite-hematite series will be described in more detail in the next chapter since rutile-hematite intergrowths, which are the topic of this thesis, form by topotaxial reactions during oxidation of the phases from this solid solution series.

1.3 Ilmenite-Hematite Solid Solution Series

The ilmenite-hematite solid solutions (Ilmenite-hematite$_{ss}$) are presented with the formula $xFeTiO_3(1\text{-}x)Fe_2O_3$. In the Figure 1.7 theoretical phase diagram for ilmenite-hematite$_{ss}$ is shown. Ilmenite and hematite form perfect solid solutions at elevated temperatures of 950-1050 °C (Lindsley, 1962). The exact temperature of stability depends on the phase composition (x value). Solubility is not symmetrical and more hematite can be dissolved in ilmenite than vice versa (Burton, 1991; Lindsley, 1973). However at lower temperatures the solubility of ilmenite and hematite is limited and these two phases are immiscible. The temperature range of miscibility gap is not precisely defined (Burton, 1985, 1991; McEnroe, et al., 2002); Lindsey (1973) defined it up to 800 °C, while Carmichael (1961) defined it between 575 and 600 °C.

The ilmenite-hematite$_{ss}$ is characterized by the Fe-Ti order-disorder transition with the change of the phase composition and temperature. Hematite rich solutions crystalize in the space group $R\overline{3}c$ and the solid solution has cation disordered composition; all regular octahedral sites are occupied by Fe^{3+} in pure hematite and randomly distributed Fe^{3+}, Fe^{2+} and Ti^{4+} in the disordered ilmenite-hematite$_{ss}$. The ilmenite-rich solid solutions have the $R\overline{3}$ structure with ordered cations; iron and titanium occupy alternating layers, where one cation layer in c-direction is pure iron and the next one is pure titanium (Nord & Lawson, 1989). If the composition is near x=0.5 (ilm50) the structure can be either ordered or disordered depending on the temperature. The phase with this composition has random distribution; Fe and Ti cations are not arranged in layers but randomly distributed within the lattice on the corundum-type sites ions at higher temperatures,

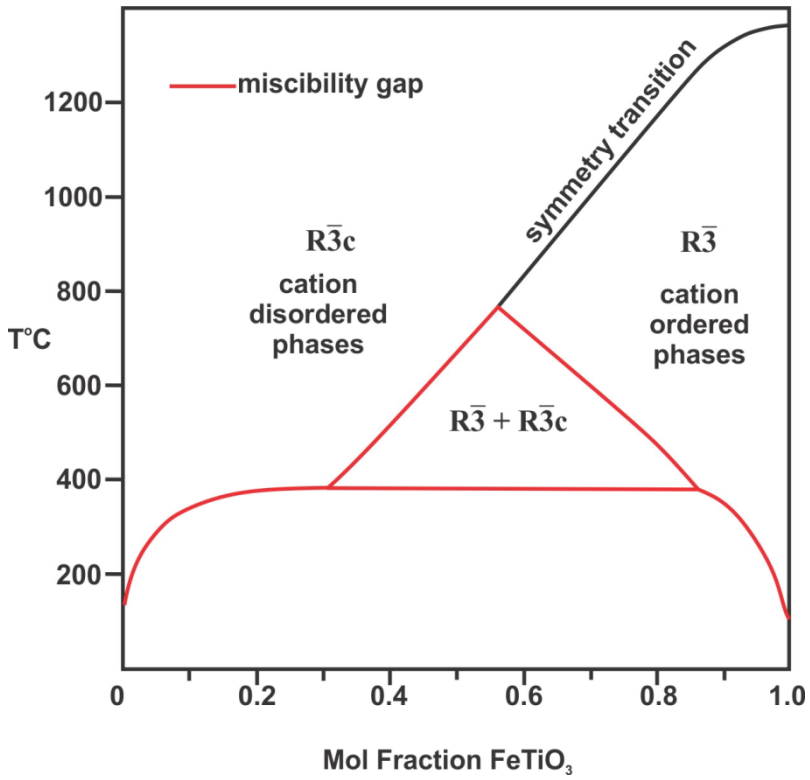


Figure 1.7: Phase diagram for the hematite-ilmenite (Fe_2O_3-$FeTiO_3$) solid solution. $R\bar{3}c$ indicates disordered phase and $R\bar{3}$ the chemically ordered phase. The miscibility is presented with the red line, while the black line presents symmetry transition of complete solid solution (Burton, 1985, 1991; McEnroe, et al., 2002).

and order ilmenite structure at lower temperatures (Ishikawa, 1958, 1962). Therefore, in more ilmenite-rich solutions (above ilm50), cation ordering will occur even before cooling and the exsoluted phases will have the structure of hematite; the final phase will be ilmenite with exsolutions of hematite. Vice versa, more hematite-rich solutions (below ilm50) will lead to precipitation of ilmenite during cooling.

Ilmenite-hematite series as a function of oxygen fugacity (f_{O_2}). Beside temperature, oxygen fugacity (or oxygen partial pressure) is another very important factor that influences the stability of ilmenite and hematite. Oxygen fugacity is a measure of oxygen availability to participate in a chemical reaction (Frost, 1991). The oxidation state of elements in melts and hence mineral assemblage of the rock depends on the level of oxygen fugacity. Consequently, the same melt can form rocks with different mineral compositions. Based on different mineral composition there are few buffers that indicate the oxygen pressure under which the rocks were formed. Buffers were developed in a laboratory in order to perform the experiments which investigated mineral stabilities (Eugster, 1957). The three most widely used buffers are quartz-iron-fayalite (QIF), fayalite-magnetite-quartz (FMQ) and magnetite-hematite (MH) buffer. These buffers are presented with the following reactions:

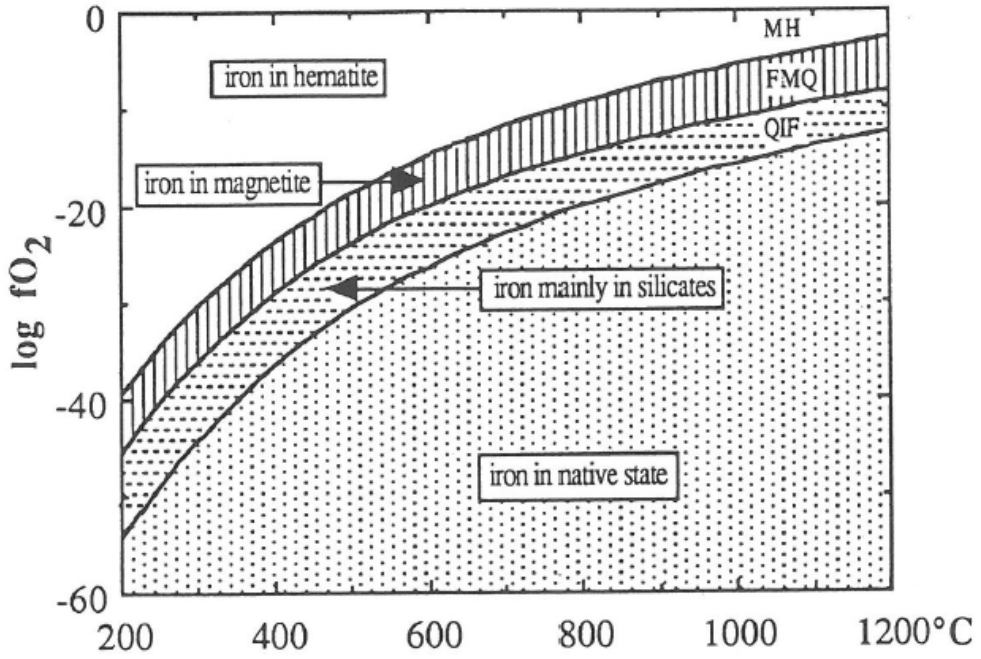


Figure 1.8: Log f_{O_2}- T diagram showing the stability of different oxidation states of iron (Frost, 1991).

$$Fe_2SiO_4 = 2Fe + SiO_2 + O_2 \qquad \text{QIF} \qquad (1.1)$$

$$2Fe_3O_4 + 3\ SiO_2 = 3Fe_2SiO_4 + O_2 \qquad \text{FMQ} \qquad (1.2)$$

$$6Fe_2O_3 = 4Fe_3O_4 + O_2 \qquad \text{MH} \qquad (1.3)$$

For each of these reactions, a line with fixed oxidation conditions for a pure mineral assemblage of the buffer is plotted in a fugacity-temperature diagram (Figure 1.8). With temperature increase, all buffers show increase in oxygen fugacity and approximately the same change in $\log f_{O_2}$-T. This is a consequence of devolatilization of magma which leads to a release of oxygen and therefore to the increase of the oxygen fugacity. For most systems in nature, mineral equilibrium is multivariant and the oxygen fugacity is changing to adapt to a mineral composition. The variation of oxygen fugacity is sub-parallel to the log f_{O_2}-T of the buffers (Frost, 1991).

The oxygen fugacity is a very important parameter in the FeO–Fe_2O_3–TiO_2 system, since iron exists in two oxidation states. At lower oxygen fugacities iron is found in divalent form incorporated in the ilmenite and ulvöspinel. With the increase of fugacity, iron is partially oxidized to the trivalent state and exists in both oxidation states, as ferrous (Fe^{2+}) and the ferric (Fe^{3+}) iron which are incorporated into magnetite. At even higher oxygen fugacities, iron occurs in the ferric state and as such it is found in hematite (Fe_2O_3) (Frost, 1991; Hill & Roedar, 1974).

Oxygen fugacity controls which phases will be formed at certain temperatures. For example, at 1100 °C and at oxygen fugacity above the FMQ buffer, oxygen is highly active causing the oxidation of iron to its highest oxidation state, resulting in the formation of ilmenite-hematite$_{ss}$ with highest percentage of Fe^{3+}. On the other hand, if oxygen fugacity is below the FMQ buffer, because of the lower activity of oxygen, iron is present also in the divalent state and as a result the main Fe-Ti oxide phase is ulvöspinel-magnetite$_{ss}$ (Toplis & Carroll, 1995). Ulvöspinel-magnetite$_{ss}$ stability only depends on the oxidation state of iron, whereas the stability of ilmenite-hematite$_{ss}$, which contains only divalent iron, is controlled also by the content of TiO_2 (Buddington, et al., 1955). At this temperature 1100°C, the TiO_2 content in melt reaches a maximum of 5.5 wt % and decreases with the decreasing temperature. Verhoogen (1962) calculated thermodynamic conditions (temperature and oxygen fugacity) that control the TiO_2 content in the Fe-Ti oxide geothermometre. The free energy of reaction ulvöspinel (Fe_2TiO_4) + hematite (Fe_2O_3) = ilmenite ($FeTiO_3$) + magnetite (Fe_3O_4) suggests that ulvöspinel would react with hematite to produce either two spinel phases and ilmenite (Ti-rich rhombohedral phase); or ulvöspinel (Ti-rich spinel phase) and two rhombohedral phases, depending on the composition of the system and the oxygen fugacity (Verhoogen, 1962).

If the stability contours of hematite-ilmenite$_{ss}$ and ulvöspinel-magnetite$_{ss}$ series are projected together on the log f_{O_2}-T diagram (Figure 1.9), the intersection of any two lines represents the temperature and oxygen fugacity at which those two solid solutions coexist. In the composition range $Hem_{15}Ilm_{85}$ to Hem_3Ilm_{97}, the compositions are unique functions of temperature and oxygen fugacity and they do not depend on the presence of the phases from magnetite-ulvospinel$_{ss}$ (Buddington & Lindsley, 1964). Oxygen fugacity at which a certain hematite-ilmenite$_{ss}$ composition is formed, can be determined if the temperature of its formation is known.

1.4 Exsolution Textures in Rhombohedral Fe-Ti Oxides (Ilmenite/Hematite)

With the change of temperature and oxygen fugacity during formation of rhombohedral Fe-Ti oxides a variety of exsolutions and intergrowth textures is formed. Observed textures result either from exsolution, eutectoid crystallization, or mineral replacement reactions (Rao & Rao, 1965).

Ilmenite and hematite form typical exsolution textures at lower temperatures because the solubility of one phase in another decreases with temperature (see the phase diagram in Figure 1.6). Depending on the composition of the host mineral, two types of textures occur: exsolution of hematite in ilmenite and vice versa. In both cases, exsolutions are in the basal plane of the host mineral occurring in the form of elongated lenses or disks parallel to each other. Sometimes more than one generation of exsolution bodies can be found, where a second generation of exsolutions is observed in the primary lamellae of the host mineral (Carmichael, 1961; Rao & Rao, 1965).

In literature there is no consistent term for different types of exsolutions. Ilmenite with hematite exsolutions can be referred to as hemo-ilmenite (Ramdohr, 1979) or ferrian ilmenite (Morisset, et al., 2010), whereas hematite with ilmenite exsolution lamellae can either be called ilmeno-hematite (Carmichael, 1961; Ramdohr, 1979) or titanohematite (McEnroe & Brown, 2000). Further in the thesis I will use terms hemo-ilmenite and ilmeno-hematite.

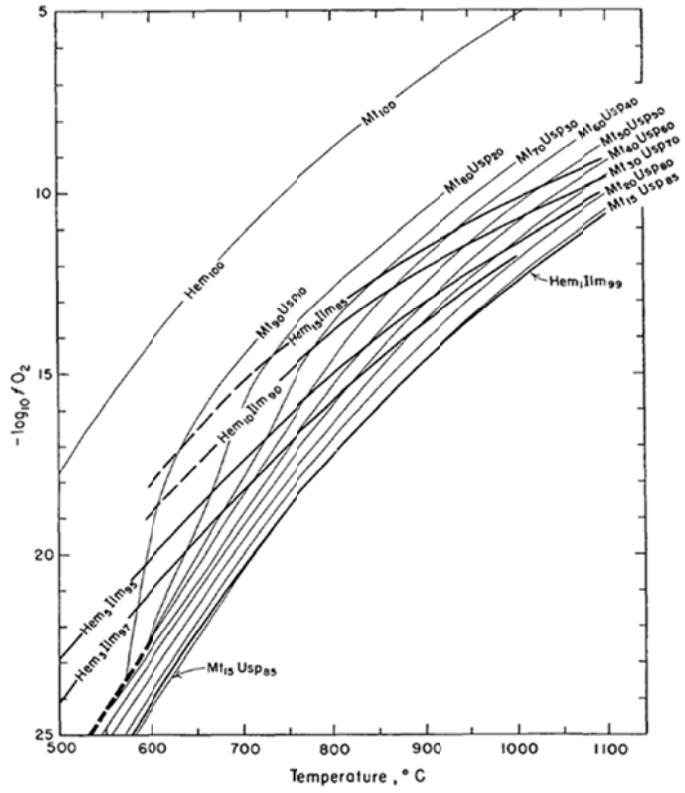


Figure 1.9: f_{O_2} -T for magnetite-ulvöspinel$_{ss}$ and hematite-ilmenite$_{ss}$. The intersection of lines for two different solid solutions represents the temperature and oxygen fugacity at which those two phases can coexist (Lindsley, 1963).

Exsolution textures within the rhombohedral Fe-Ti oxides are extensively studied in the Fe-Ti ore deposits. The most important ore deposits, which are currently exploited, are the massive ilmenite ($FeTiO_3$) deposit at Lac Tio (Allard Lake) associated with the Lac Allard anorthosite suite in Quebec, Canada (Carmichael, 1961; Charlier, et al., 2010; Morisset, et al., 2010), and the ilmenite-norite deposit at Tellnes in the Rogaland anorthosite province, Norway (Charlier, et al., 2007; McEnroe, et al., 2002).

The primary mineral of the rhombohedral Fe-Ti oxides in both deposits is hemo-ilmenite with ilmeno-hematite lamellae (Figure 1.10a). The thickness of lamellae varies from a few nanometers up to 20 µm (sometimes even up to 100µm). The thickness varies with the generation of their formation. In contrast to the irregular shape of the large and intermediate second generation of hemo-ilmenite lamellae, the small lamellae have a long and an intermediate dimension in the basal plane, as well as a short dimension in the c-axis direction (Carmichael, 1961). These lamellae are actually well-defined discrete hematite precipitates with thicknesses in the order of 10 nm, surrounded by homogeneous ilmenite host.

The lamellae form by nucleation and growth, which is controlled by the diffusion rate and the distance between two nucleating sites. Coarse and large lamellae are formed at high temperatures when the diffusion is fast, whereas nanometre-sized lamellae are formed at lower temperatures where the diffusion processes are slow (McEnroe, et al., 2002; McEnroe, et al., 2007). Once hematite lamellae nucleate within ilmenite, they grow by inward diffusion of Fe^{3+} ions and outward diffusion of Fe^{2+} and Ti^{4+} ions, and once

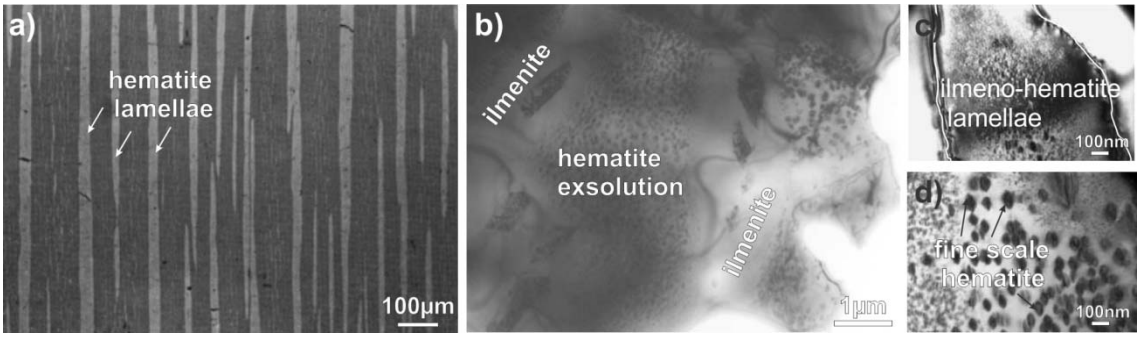


Figure 1.10: Exsolution texture observed in hemo-ilmenite from Allard Lake region of Quebec a) The hematite lamellae are parallel to the basal plane of host ilmenite. (Carmichael, 1961). b) Low magnification TEM image of typical microstructure of the ilmenite host with nanometre sized hematite lamellae (McEnroe, et al., 2007). c) HRTEM image of hematite lamellae containing fine scale ilmenite precipitates. d) Nanosized hematite precipitates of hematite in ilmenite host formed during fast cooling of magma (McEnroe, et al., 2002).

nucleated in hematite, ilmenite lamellae must grow by inward diffusion of Ti^{4+} and Fe^{2+} and outward diffusion of Fe^{3+} ions (McEnroe, et al., 2002).

In the Rogaland region, several generations of exsolution lamellae indicate slow cooling rates leading to several exsolution cycles at low temperatures, where slow diffusion rates limit the size of the lamellae (Figure 1.10b). With time, the regions between lamellae become too big for lamellar diffusion, and they retain the hosting ilmenite composition. Because of the slow diffusion rates, the regions between the exsoluted lamellae remain more hematite rich than expected at low temperatures; these regions become oversaturated and new, very small lamellae nucleate, triggering another nucleation cycle, in which a generation of lamellae with smaller size is formed (Figure 1.10c). Larger lamellae which formed at higher temperatures when the diffusion was faster are surrounded by smaller exsolution bodies. Rapid cooling of magma with hematite-ilmenite$_{ss}$ results in nanosized precipitates homogeneously distributed within the matrix (Figure 1.10d) (McEnroe, et al., 2002).

1.5 Oxidation of Ilmenite and Formation of Rutile Intergrowths with Hematite and Ilmenite

Ilmenite contains ferrous iron (Fe^{2+}), therefore it is prone to oxidation that results in formation of hematite and rutile as end-phases. At low temperatures, oxidation of ilmenite can be presented by the following equation:

$$4FeTiO_3 + O_2 \rightarrow 4TiO_2 + 2Fe_2O_3 \tag{1.4}$$

while at temperatures above 800 °C it results in the formation of pseudobrookite, according to the following equation:

$$4FeTiO_3 + O_2 \rightarrow 2Fe_2TiO_5 + 2TiO_2 \tag{1.5}$$

1.5.1 Oxidation of ilmenite under natural conditions

Oxidation of ilmenite occurs during cooling of the deposits along grain boundaries or cracks within ilmenite grains. The reaction of oxygen and ilmenite results in the formation of hematite and rutile, while the Fe/Ti ratio of the bulk rock remains constant (Morisset, et al., 2010; Rao & Rao, 1965). Hydrothermal processes also lead to an ilmenite transformation to intergrowths of rutile and hematite (Ramdohr, 1979).

Rutile crystals are usually found in the form of needle-like exsolutions within rhombohedral planes of the parent ilmenite and the rutile needles intersect at roughly 60° (Baker & Buddington, 1970; Force, 1980; Ramdohr, 1979; Rao & Rao, 1965). In ilmenite deposits, rutile is also found in two other morphologies: as fine-grade rutile lenses (10 to 200 µm) within ilmenite grains or along ilmenite grain boundaries and as discrete rutile grains (Morisset, et al., 2010). The large and isolated grains (up to 5 mm) are formed during the differentiation of magma and present a primary mineral. The
presence of the minor lenses of rutile within ilmenite are mostly surrounded by hematite. The rutile lenses are therefore secondary phases formed by late oxidation reaction of ilmenite or ilmenite-hematite$_{ss}$.

In metamorphic rocks ilmenite-hematite$_{ss}$ are transformed and form two types of textures. Degree of orientation of formed rutile with respect to the original crystal depends on temperature. At higher temperatures rutile is found in the form of large needles growing in different directions resulting in a blitz structure (Figure 1.11). At lower temperatures, rutile forms only small and isolated rutile needles (Brownlee, et al., 2010; Ramdohr, 1979).

1.5.2 Oxidation of ilmenite for the production of TiO_2

TiO_2 powders are produced by acid-leaching of ilmenite since ilmenite deposits are abundant in nature and rutile deposits cannot provide enough supplies for market demands. Oxidation of ilmenite is a pre-process in ilmenite acid-leaching; during oxidation the Fe^{2+} is transformed to a more soluble Fe^{3+} that is more easily leached out resulting in the production of more pure TiO_2 powders (Murphy & L.Frick, 2006).

Which phases will be formed depends on the temperature of oxidation (Briggs & Sacco, 1993; Fu, et al., 2010; Zhang, et al., 2013). At higher temperatures the oxidation will lead to formation of pseudobrookite, while on lower temperature hematite and rutile will form as the most important phases, as well as some intermediate crystallographic shear (CS) phases - $Fe_2Ti_3O_9$ (Bhogeswara Rao & Rigaud, 1974, 1975; Fu, et al., 2010; Grey & Reid, 1972) and $Fe_2Ti_2O_7$ (Gupta, et al., 1991; Zhang & Ostrovski, 2002). Beside temperature, grain size also influences the oxidation products (Fu, et al., 2010). Rutile and CS phase are formed by parallel and competing reactions Eq 1.4 and Eq 1.6, which determine the phase composition of the oxidation product.

$Fe_2Ti_3O_9$ formation is favoured with smaller particle size and higher oxygen pressure, and rutile is the main product with a large particle size and low oxygen pressure. Also, rutile formation is slightly increased with temperature (Fu, et al., 2010). With the decreasing grain size specific surface is higher and so the oxidation is faster. First step in transformation is the oxidation of Fe^{2+} to Fe^{3+} that as smaller cation leaves the structure resulting in formation of intermediate metastable phase (Fu, et al., 2010).

$$12FeTiO_3 + 3O_2 \rightarrow 4Fe_2Ti_3O_9 + Fe_2O_3 \tag{1.6}$$

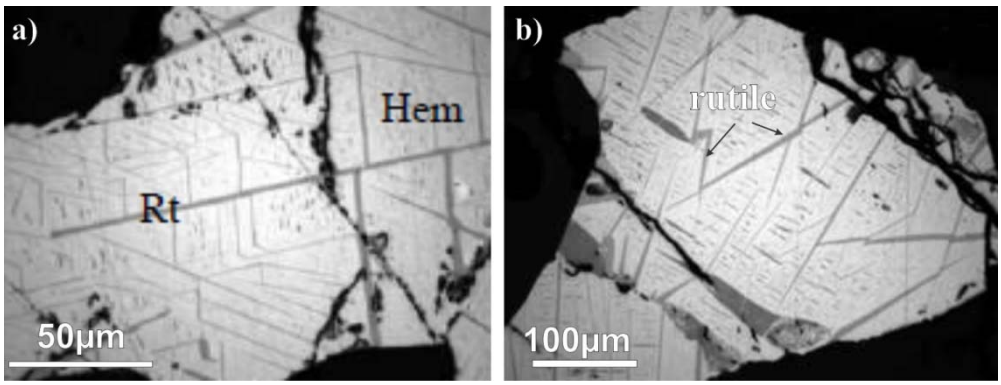


Figure 1.11: Rutile lamellae in oxidized ilmenite from Ecstall pluton, British Columbia, Canada (Brownlee, et al., 2010).

During the oxidation morphology of ilmenite is changing. The energy for Fe ion diffusion comes from chemical potential of the oxidation reaction and its diffusion to the surface results in the growth of a hematite layer. Gaseous diffusion of O_2 cannot cause the formation of this layer but it is formed through the reaction with oxygen on the surface of ilmenite (Fu, et al., 2010). In the case of ilmenite, oxygen and titanium can also diffuse in the structure to provide solid-state transformation. During the oxidation rutile grains are formed in the interior of ilmenite grain (Briggs & Sacco, 1993). At lower temperatures rutile forms the needle-like grains. However, at temperatures above 800°C, rutile and hematite tend to combine into thermodynamically stable pseudobrookite. The initial needle-like rutile network is destroyed and both hematite and rutile are consumed to form the morphology with irregular rutile grains and isolated hematite grains dispersed in the pseudobrookite matrix (Zhang, et al., 2013). The formation of pseudobrookite is not direct but through reaction of already formed rutile or intermediate phase and hematite at lower temperature (Zhang, et al., 2013). This part of transformation can be presented with the following reactions:

$$TiO_2 + Fe_2O_3 \rightarrow Fe_2TiO_5 \tag{1.7}$$

$$Fe_2Ti_3O_9 + 2Fe_2O_3 \rightarrow 3Fe_2TiO_5 \tag{1.8}$$

The schematic presentation of ilmenite oxidation mechanism is presented in Figure 1.12.

1.5.3 Crystallographic orientation relationships in the ilmenite-hematite-rutile system

Temperature, oxygen fugacity and oxidation are the factors that lead to phase transformations in Fe-Ti-O system. Because of structural similarities of ilmenite, hematite and rutile, these transformations are topotaxial in nature. The common feature of all three structures is oxygen hexagonal close packing. Because of the difference in the angle between oxygen chains in corundum and rutile type structure, different types of exsolutions are possible. The difference of 2.78° leads to different orientation relationships during phase transformations. Armbruster (1981) described two possible orientation relationships (OR) of rutile with the corundum type structure. In first OR straight chains

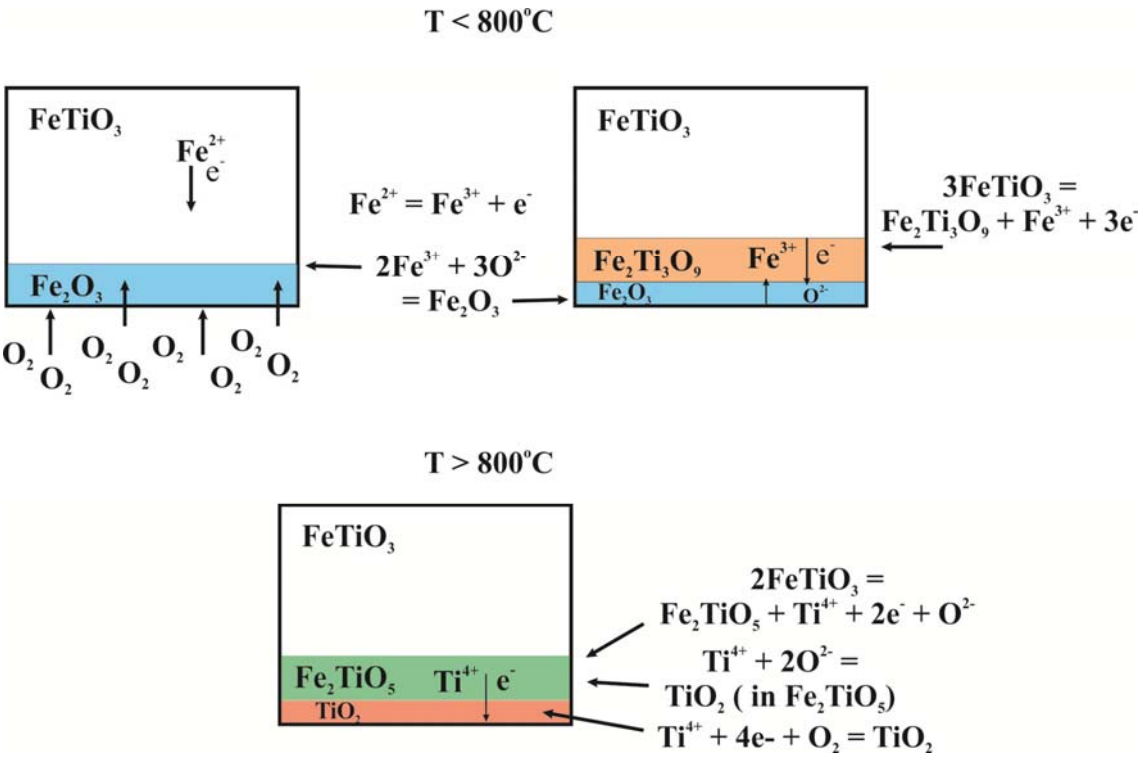


Figure 1.12: Schematic presentation of ilmenite oxidation mechanism. Oxidation starts with the reaction of Fe^{3+} with oxygen on the surface and formation of hematite layer. With the further increase of the temperature, the intermediate phase is formed. At temperatures above 800 °C pseudobrookite is formed by diffusion of Ti^{4+} and simultaneously, rutile can be formed (Bhogeswara Rao & Rigaud, 1975).

in rutile are parallel to straight oxygen chains in hematite/ilmenite leading to the orientation:

$$\text{OR-1: } <001>_R \{010\}_R \parallel <210>_C \{001\}_C$$

If the undulating $(101)_R$ chains in rutile are parallel to straight chains in hematite/ilmenite, a second orientation relationship will exist:

$$\text{OR-2: } <101>_R \{010\}_R \parallel <210>_C \{001\}_C$$

The rutile intergrowths that follow OR-1 intersect at 60 or 120° (Figure 1.13a). If the intergrowths follow the OR-2, they form twin boundaries: $(301)_R$ twin with the twining angle of 54.7° and $(101)_R$ twin with the angle of 114.4° (Figure 1.13b). Force (1991) suggested that angles between rutile individuals in intergrowths are indicators of their formation; rutile formed by topotaxial transformation has angles of 60 or 120°, while the intergrowths with OR-2 are growth twins.

Recent investigations by Daneu, et al. (2007, 2014) showed that growth twins can also be formed by topotaxial transformation of Al-rich Fe-Ti oxy-hydroxide precursors with tivanyte-type structure. This topotaxial transformation results in well-defined junction between rutile individuals according to OR-2 resulting in sagenite structure. On twin boundaries there are remains of a precursor phase; in thecase of $(101)_R$ twin it is precipitate of corundum phase and $(301)_R$ twin boundary few nm thick Al-rich ilmenite

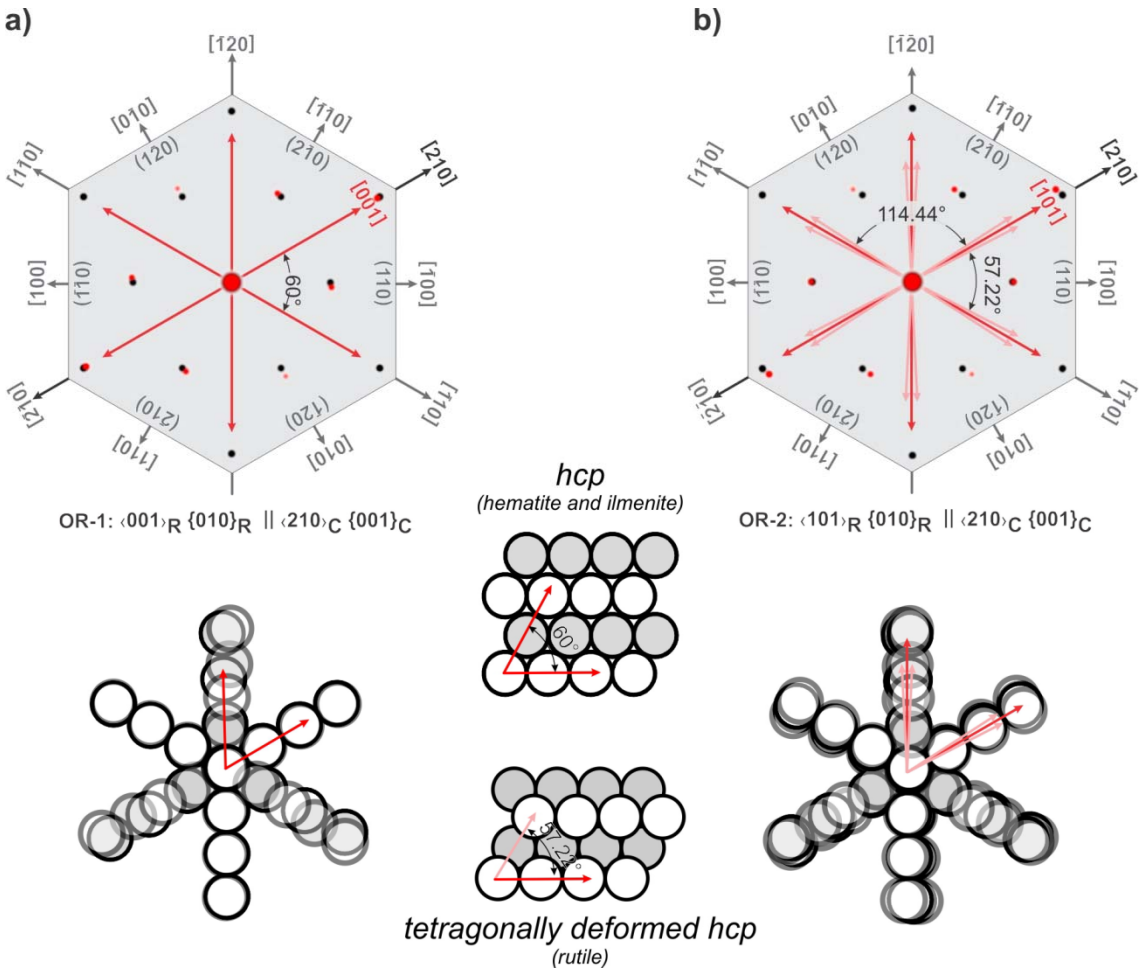


Figure 1.13: Schematic presentation of two orientation relationships between corundum type structure (black arrows) and rutile (red arrows) a) The OR-1, where the c-axes of rutile crystals <001> are parallel to the <210> directions of corundum structure resulting in three orientations of rutile, which intersect at 60°or 120°. b) In OR-2 the c-axis of rutile is misaligned for 2.78° away from <210>-type directions of corundum type structure and therefore the <101> directions in rutile are parallel to the <210> directions of corundum type structure. This orientation relationship leads to formation of $\{101\}_R$ and $\{301\}_R$ twin boundaries.

lamellae is found. In literature the crystallographic orientation relationship was determined based only on macroscopic observations (Armbruster, 1981; Force, et al., 1996). However, the OR deduced from morphology can differ from the one at the atomic level. In the case of ilmenite/hematite intergrowths with rutile the OR is defined by difference of only 2.78°; the angular difference of intersection of oxygen chains in corundum and rutile type structure. This angular difference is difficult to observe in the morphology of crystal, but it can be very significant at atomic level. For this reason, in this thesis I will investigate topotaxial transformation of ilmenite to rutile and hematite at atomic level.

Chapter 2

Experimental Methods

For analyses of rutile intergrowths with hematite and ilmenite I used top-down approach, starting with X-ray powder diffraction (XRPD) for the determination of bulk phase composition. After the determination of phase composition I investigated the texture and microstructure of the samples with optical microscopy and further with electron microscopy down to atomic-resolution investigations. Optical microscopy and XRPD give a general bulk phase composition and crystallographic relations between parent mineral and newly formed phases in topotaxial transformation on macroscopic level. However, electron microscopy methods provide insight into structural and chemical composition of minerals at the atomic level.

X-ray powder diffraction (XRPD) was used for the determination of phase composition of bulk samples and changes in the phase composition during heating experiments. However, this method is not suitable for the determination of the phases present with less than ~2 wt% in the sample, and for this reason I combined the XRPD analyses with electron microscopy techniques. Raw data were interpreted by Philips X'Pert HighScore Software Suite (Philips PANalytical B.V.) using PDF2 database (International Centre for Diffraction Data).

Optical microscopy was used for identification of mineral composition and for observation of distribution of the phases in the samples. I used both transmitted and reflective light, since the combination of both methods enables observation of optically transparent and opaque phases. All samples were examined under optical microscope Zeiss Axio Imager.Z1m, Carl Zeiss Light Microscopy. For sample investigation I used polarized light and polarization filters, integrated into microscope system.

Scanning electron microscopy (SEM) was used for determination of samples morphology with secondary electrons (SE), phase composition with backscattered electrons (BSE) and for chemical semi-quantitative analyses with energy-dispersive spectroscopy of X-rays (EDS). SEM techniques were suitable for determination of phase composition of larger inclusions and precipitates of rutile in hematite/ilmenite matrix.

For imaging and phase semi-quantitative chemical analyses of our samples I used two scanning electron microscopes; SEM; Jeol JSM-5800 operated at 20 kV and equipped with an energy-dispersive X-ray spectrometer (EDS; Oxford Instruments Model 6841, Oxford Instruments PLC) and microscope with in-lens thermal field-emission gun FEG-SEM Jeol JSM-7600F, equipped with integrated EDXS system (Oxford INCA X-Max 51-XMX 0021).

Transmission electron microscopy (TEM). For TEM imaging, samples must be electron transparent with thickness of up to several tens of nanometers, depending on the atomic number of the specimen and electron energy of the source. Sample preparation is therefore a crucial step for high-quality TEM imaging. Electron transparency may be

obtained simply by crushing the bulk sample to submicron sized grains and thes deposition on the carbon-coated grid (Cu or Ni). In Figure 2.1 the TEM images of crushed samples from Mwinilunga, Zambia, are presented. This sample preparation technique did not prove advantageous for the analysis of oriented intergrowths because it was not possible to observe any contacts between hematite and rutile. Also, the deformation {011} twins were introduced in rutile grains by the stress induced with crushing. In addition, the hematite part of the sample appears to be nanocrystalline giving the selected area electron diffraction (SAED) characteristic for powders containing no information about orientation of hematite. This was misleading since the self-supporting oriented samples showed that hematite is single-crystalline between rutile lamellae. Therefore, the samples for observations of oriented intergrowths were prepared using the conventional specimen preparation technique. The samples were prepared by orienting the single crystal in specific crystallographic orientation with the rutile contacts with hematite or ilmenite in the centre of the TEM sample. The first step in preparation of oriented samples was cutting it using a wire-saw (Precision Diamond Wire Saw 3242, Well Diamond Wire Saws Inc.) and mounting in a brass tube. Further the sample was mechanically thinned to ~ 100 µm with disk grinder (Gatan Disc Grinder Model 623) and dimpled (Dimple grinder 656, Gatan Inc.) down to 15µm. Final step in sample preparation was perforation in order to obtain electron-transparent regions. The perforation was achieved with Ar^+ ions at glancing angle of 8° at 4,5 eV (PIPS 691 Precision Ion Polishing System, Gatan Inc.). In order to obtain information about the interfaces and for determination of crystallographic orientation relationship in 3 dimensions, samples were prepared in two perpendicular orientations.

The chemistry and structure of the oriented samples were studied using transmission electron microscope JEM-2100, Jeol with LaB_6 filament operating at 200 kV, equipped with an energy-dispersive X-ray spectrometer (EDXS; JED-2300T analyser, Jeol Inc.) and FEG 200 kV transmission electron microscope JEM-2010F, Jeol with point-to-point resolution of 0.23 nm and equipped with an energy-dispersive X-ray spectrometer (EDS; JED-2300 analyser, Jeol Inc.) suited for semi-quantitative chemical analysis. The micrographs were collected using high-resolution CCD camera (Orius DC1000, Gatan Inc.). The microscope used for the local characterization of the particles was a probe Cs corrected Jeol ARM200F equipped with a cold FEG and operated at 200 kV. The presence of Ti and its valence state was followed by an EELS system GIF Quantum ER with Dual EELS from Gatan.

For chemical and structural characterization of crystals and defect structures at atomic level I used numerous TEM techniques for imaging (high resolution transmission electron microscopy-HRTEM, scanning transmission electron microscopy-STEM, high-angle annular dark-field-HAADF), diffraction technique (selected area electron diffraction-SAED), and analytical techniques (energy dispersive X-ray spectroscopy-EDS, electron energy loss spectroscopy-EELS). High resolution transmission electron microscopy (HRTEM) analysis was used for determination of the contact planes between different phases (rutile/rutile, rutile/hematite and rutile/ilmenite) and for investigating different structural defects (edge dislocations, crystallographic shear phases). For simple interpretation of the chemical composition in image mode I used Z-contrast images where the contrast from the atomic column in the observed projection is directly proportional to its average atomic number. SAED was used to obtain accurate crystallographic information about relationships between rutile and hematite intergrowths and the precipitates in the samples, as well as for the determination of rutile twins and rutile domains orientations.

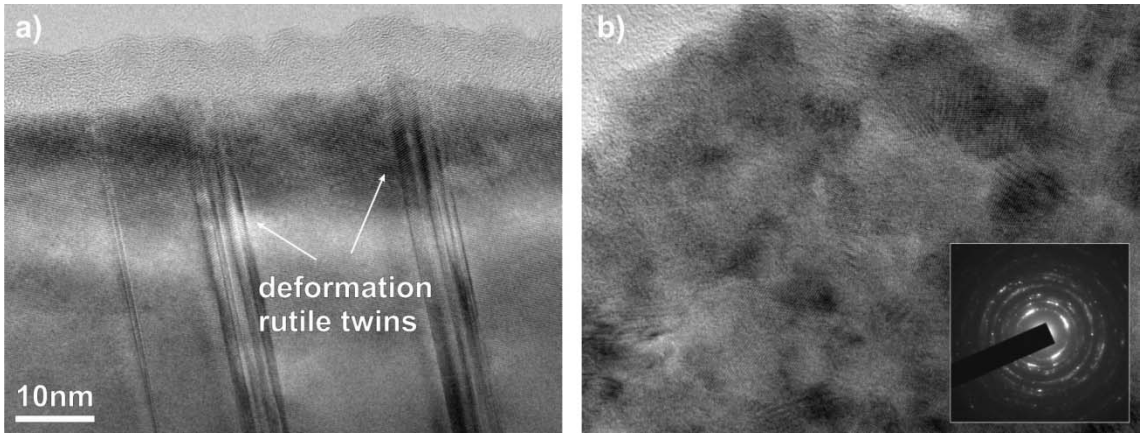


Figure 2.1: TEM images of grinded samples a) rutile particle showing the presence of deformation twins introduced by grinding; b) TEM image of grinded hematite that becomes nanosized with no possibility for observation of rutile/hematite contact.

Analytical techniques in TEM were used to obtain information about chemical composition of the samples. The two methods used were energy dispersive X-ray spectroscopy (EDS) and electron energy loss spectroscopy (EELS) for the determination of oxidation state and bonding character of elements.

Chapter 3

Oriented Rutile/Hematite Intergrowths from Mwinilunga, Zambia

I started the investigations of topotaxial transformation of ilmenite to rutile and hematite on natural rutile/hematite intergrowths from Mwinilunga, Zambia. These samples were suitable for the investigation since the ilmenite is not completely recrystallized to rutile and hematite and the different stages of transformation could be observed. Another advantage of these samples is their morphology that enabled simple orientation of samples that is of key importance for analyses of the transformation mechanisms. In this part of the thesis I will present the results of top-down investigations of these natural intergrowths, starting with the description of the sample at the macroscopic level, followed by analyses of the texture of the sample observed with optical microscope and SEM. At the end I will present results of TEM analyses where the orientation relationship between hematite and rutile and their interfaces will be described in detail.

3.1 Specimen Description and XRD-Phase Analyses

The typical appearance of the intergrowths of hematite and rutile from Zambia are presented in Figure 3.1. Oriented intergrowths of hematite and rutile from Mwinilunga in Zambia occur in a few centimetres large tabular hematite crystals with the smaller rutile crystal of only few millimetres found on the hematite surface. Rutile crystals grow in a specific orientation relationship; even at macroscopic level it is possible to determine orientation relationships between rutile and hematite.

Rutile is found in the form of single crystals, and in the form of $(101)_R$ and $(301)_R$ twins, where the $(101)_R$ are more common (Figure 3.1a). The $(101)_R$ and $(301)_R$ twins are distinguished by characteristic angles between rutile c-axis of two individuals (Lee, et al., 1993). All rutile crystals are jagged parallel to their c-axis. The rutile c-axis is ~ 3° tilted from the edges of the parent hematite crystal, and $\{101\}_R$ are perpendicular to $\{100\}_H$ (visible as grooves). Based on macroscopic observations the orientation of rutile corresponds to OR-2:

$$\text{OR-2: } \langle 010\rangle_R \{101\}_R \parallel \langle 001\rangle_H \{110\}_H$$

The interior sections of rutile/hematite samples were first examined for bulk phase composition. The samples were crushed in an agate mortar and analysed by a X-ray

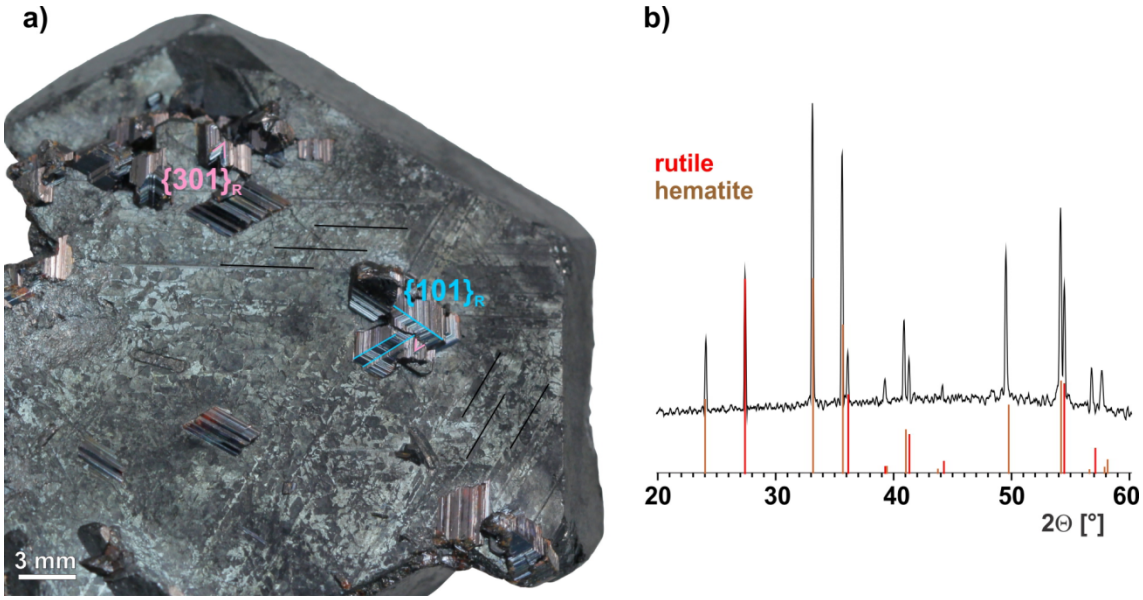


Figure 3.1: Oriented intergrowths of rutile and hematite from Mwinilunga, Zambia. a) Tabular, 3 cm large, hematite crystal with rutile on the surface in a specific crystallographic orientation relationship. Both types of rutile twins are observed on the surface, together with isolated rutile crystals. It is visible that $\{101\}_R$ planes are normal to $\{110\}_H$ planes that are visible in the form of fringes on hematite surface. b) XRD diagram of the sample shows that only hematite and rutile are present in the sample.

powder diffractometer (PW1710, Philips GmbH, Germany) using a Ni-filtered Cu-K_α radiation in the range 2θ = 20–60° with a step of 0.02° and recording time of 0.5 s/step. The XRD of the sample showed that only two present phases in the sample are rutile and hematite (Figure 3.1b). The amount of other possibly present phases was below XRD detection limit.

3.2 Textural Characterization of the Intergrowths by Optical Microscopy and SEM

The samples were further studied with optical microscope and SEM for characterization of texture and microstructure in the interior of the intergrowths. A few millimeters thin segments were cut from the intergrowth crystals in two perpendicular orientations ($[001]_H$ and $[100]_H$) and glued on the glass substrate for preparation of thin sections for optical microscopy investigation. They were further thinned to about 10µm and in the final step polished by ¼ µm diamond paste. Typical texture of the intergrowths observed from two different directions with optical microscope is presented in Figure 3.2. Hematite is optically opaque, and it is therefore black under the transmitted light. On the other hand, rutile is optically transparent and therefore exhibits different colours in perpendicular orientations in transmitted light (red, brown and yellow). The ratio of hematite and rutile in the interior of the intergrowths is approximately 1:1 (Figure 3.2a). Rutile crystals are larger near the surface with more rutile-rutile contacts which are

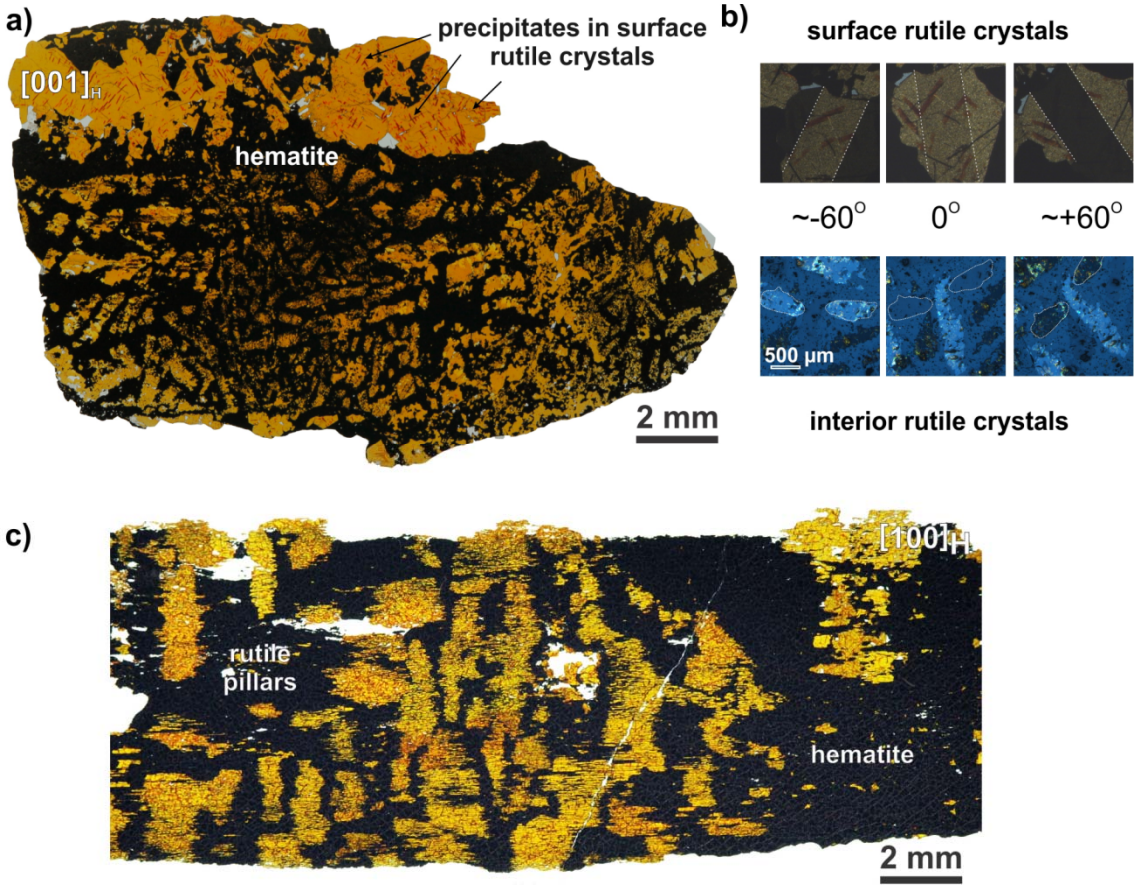


Figure 3.2: Rutile/hematite intergrowths under polarized light microscope. a) Sample observed from $[001]_H$ shows two types of rutile crystals; large with many direct rutile-rutile contacts on the surface and more elongated and irregularly shaped crystals with less direct rutile-rutile contacts in the interior of the intergrowths. Rutile crystals on the surface contain parallel red precipitates. b) Rutile shows regular extinctions of domains on every ~60 ±5 °. c) Sample observed from $[100]_H$ shows different texture, where rutile platelets form pillars that extend throughout the sample height.

sharper and longer than in the interior of the sample. During in-plane rotation of the thin sections, rutile shows extinction of rutile domains on ~60° with about ±5° shift from each set related to the twins (Figure 3.2b). Rutile domains show the presence of very thin parallel red stripes extending in two directions and mirrored across twin boundaries. As already observed at the macroscopic level, rutile crystals near the surface are mostly in the form of $\{101\}_R$ twins. Observed from the $[100]_H$ samples show very different texture and rutile forms pillars in hematite matrix (Figure 3.2c). Some of the rutile pillars extend through the whole thickness of the hematite.

The sample was further analyzed with scanning electron microscope. SEM images of the sample observed from $[001]_H$ are presented in Figure 3.3. It is visible that the rutile crystals on the surface are well developed and show typical sagenite in-plane network (Figure 3.3a) where most of the crystals show $\{101\}_R$ twinning with sharp and long contact planes (Figure 3.3b). Backscattered image of the polished rutile crystals near the sample's surface shows the presence of thin bright lamellae extending in two directions (Figure 3.3c). The orientation is consistent throughout the whole sample suggesting

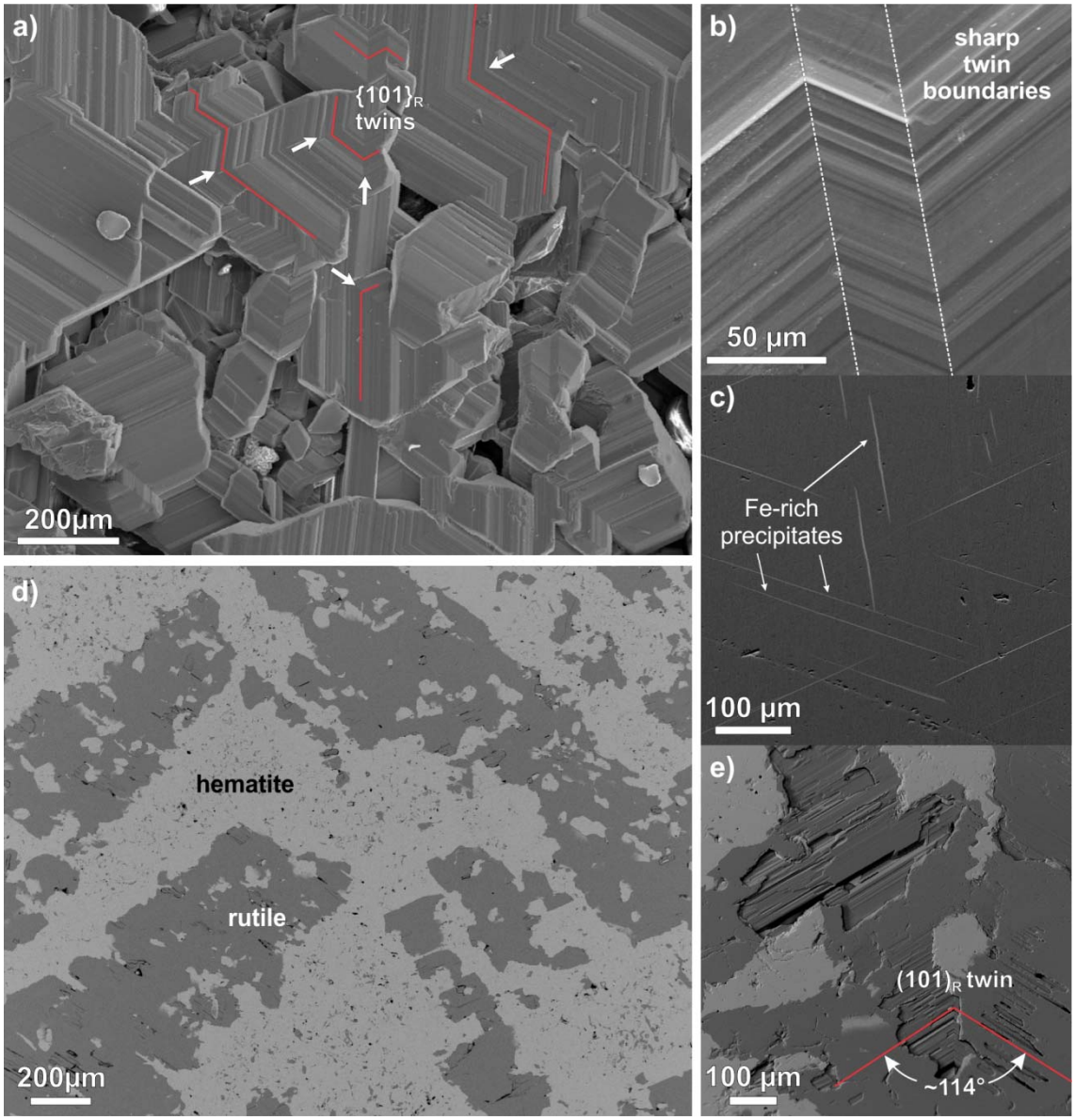


Figure 3.3: SEM images of sample observed from $[001]_H$ direction. a) SE image of the surface showing recrystallized, well-developed rutile crystals with abundant $\{101\}_R$ twins. The $\{101\}_R$ twins are observed in form of simple twins, to more complex ones with two or more twin combinations forming incomplete cyclic twin. The red lines denote the direction of the rutile c-axis, while some of the twin planes are pointed out by arrows. b) The SE image of twins from the surface shows straight contact planes. c) BSE image of polished surface rutile crystals shows very thin lamellae growing in two directions. EDS analyses showed that they are Fe-rich and probably are exsoluted hematite. d) BSE image of the interior of the sample where the elongated rutile domains are very rarely in contact. e) Two rutile domains in $\{101\}_R$ rutile twin show a characteristic angle of ~114°.

structurally controlled exsolution to specific planes of rutile. EDS analyses showed that these lamellae are enriched with Fe. The abundance and coarse crystallinity of the surface rutile crystals indicate free recrystallization on the surface of the hematite crystals. On the other hand, rutile crystals in the interior show irregular shapes (domain-

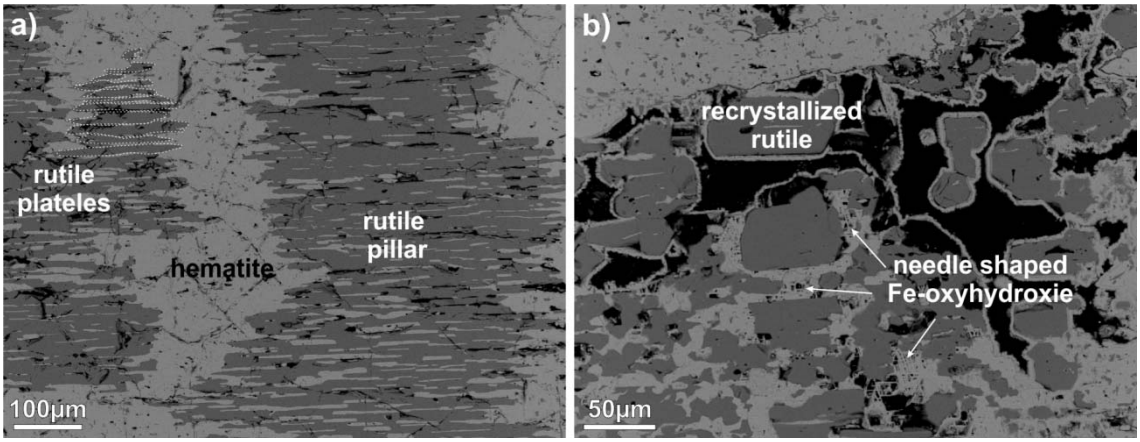


Figure 3.4 BSE/SEM images of the sample observed from $[100]_H$ direction. a) Rutile pillars in hematite matrix are elongated in the direction of b-axis of rutile. Every pillar is constructed from paralel rutile platelets. b) Pores in hematite matrix show recrystallized rutile grains surrounded with needle shaped Fe-oxyhydroxides.

shape) and almost without any rutile-rutile contact planes (Figure 3.3d). The most abundant contact planes that are observed in the central part of the sample are usually the $\{101\}_R$ planes. The direction of the elongation of rutile domains in the interior is not parallel to the rutile's c-axis which is not usual for rutile growth since it usually shows preferential growth in the direction of the c-axis in the absence of some outer restraints (Figure 3.3e). Three general directions of rutile growth intersecting at ~60° ± 5° are observed also in the SEM images (Figure 3.3d). However, rutile is still growing in three main directions intersecting at roughly 60°.

The pillar structure of the rutile/hematite intergrowths observed from the $[100]_H$ is shown in Figure 3.4. Typical thickness of a single rutile platelet is around 20µm whereas its width can reach up to few mm (Figure 3.4a). The contact between rutile and hematite is wavy due to the different thicknesses of individual rutile platelets. Rutile is also observed in the form of small grains in the hematite matrix surrounding the pillars. Occasionally pores are present in the interior of the sample. Within these pores, rutile is recrystallized to larger grains and surrounded by a needle-like Fe-rich phase. The shape of this phase suggests it is some oxyhydroxide phase, most likely lepidocrocite or goethite that is characteristic for post-hydrothermal processes (Figure 3.4b).

3.3 Crystallography of Rutile/Hematite Intergrowth Structures

Already at macroscopic level it was possible to determine the crystallographic orientation between hematite host and rutile crystals. For further analyses of rutile/hematite intergrowths I prepared oriented TEM samples from the interior of the sample in order to investigate the crystallographic relations with TEM. The TEM analyses of all samples confirmed that the orientation of hematite remains unchanged throughout the whole intergrowth. For observation of different orientations of rutile towards the hematite matrix, the samples were oriented in $[001]_H$ direction. In this zone axis, rutile lamellae intersect the hosting hematite crystal at different orientations, forming random topotaxial networks. Rarely, two rutile lamellae intersect to form a twin boundary. One of such situations is presented in Figure 3.5a. The SAED pattern taken

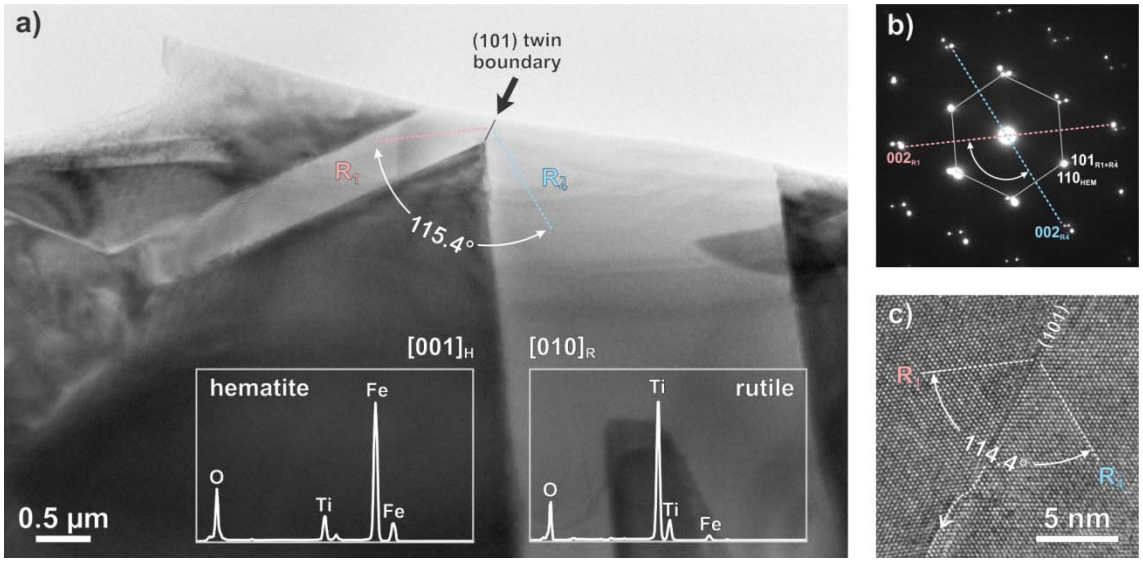


Figure 3.5: $(101)_R$ rutile twin in hematite matrix viewed along $[001]_H$. a) TEM image of rutile $(101)_R$ twin in hematite matrix superposed with EDS spectra taken in rutile and hematite revealing that the hematite matrix always contains certain amounts of Ti, and rutile always contains some Fe. b) SAED taken across rutile twin and hematite matrix confirmed OR-2 between the two phases. c) HRTEM image of $(101)_R$ rutile interface with atomic steps to neighbouring planes to compensate for the small orientation mismatch. Additionally. the section with ideal $(101)_R$ twin boundary is visible and the angle between the c-axes of the twinned rutile domains of 114.4° is shown.

across the rutile twin and the hematite matrix shows doubling of diffraction spots, characteristic for a $\{101\}_R$ twin boundary and oriented relationship with hematite matrix according to the OR-2 (Figure 3.5b). The angle measured from SAED between two c-axes of two rutile individuals is slightly larger (~115°) than the typical angle for rutile $(101)_R$ twins. HRTEM image of the $(101)_R$ interface shows that the twin boundary is disturbed by edge dislocations (Figure 3.5c). The twin boundary has 13 to 15 nm sections of undistorted $(101)_R$ –twin boundary with the characteristic angle of 114° between c-axes. Every dislocation step introduces one additional plane to compensate for ~1° mismatch that is observed in SAED. The length of an undistorted step matches the distance of $d(101)_R/\tan(\theta') = \sim 14$ nm.

Since the rutile-rutile interfaces are a result of impingement of two growing rutile domains we further investigated how many different rutile-rutile contacts can be produced by topotaxial growth of rutile in hematite matrix. As the $(101)_R$ is aligned with $(110)_H$ there is an angular difference of 2.78° between c-axis of rutile and b-axis of hematite (Armbruster, 1981). As a consequence rutile can adopt two mirror orientations (±) with respect to each one of the six $\{110\}_H$ planes, which leads to 12 possible hematite/rutile orientations ($H|R_i$). During rutile growth, any of the 12 rutile individuals (R_i) can impinge with rutile form another set of 12 rutile (R_j) individuals, leading to a total of 144 possible rutile-rutile contacts ($R_{i|j}$) listed in Table 3.1. However, not all of the possible contacts are unique; some of them can be ruled out for different reasons. Some of the configurations result in the formation of rutile crystals in single- crystal orientation; there are 24 combinations that end in a single crystal orientation. The other type of rutile/rutile contacts that can be excluded from the theoretical 144 orientations are impingements that form identical $R_{i|j}$, only the growth direction of the two domains is opposite and these can also be cancelled out. For example $R_{2|3}$ is equal to $R_{3|2}$.

Table 3.1: List of all possible rutile-rutile configurations forming during impingement of rutile lamellae according to the OR-2 law.

i|j	1	2	3	4	5	6	$\bar{1}$	$\bar{2}$	$\bar{3}$	$\bar{4}$	$\bar{5}$	$\bar{6}$
1	$R_{1\|1}$ 0°	$R_{1\|2}$ 5.56°	$R_{1\|3}$ 60°	$R_{1\|4}$ 65.56°	$R_{1\|5}$ 120°	$R_{1\|6}$ 125.56°	$R_{1\|\bar{1}}$ 180°	$R_{1\|\bar{2}}$ -174.44°	$R_{1\|\bar{3}}$ -120°	$R_{1\|\bar{4}}$ -114.44°	$R_{1\|\bar{5}}$ -60°	$R_{1\|\bar{6}}$ -54.44°
2	$R_{2\|1}$ -5.56°	$R_{2\|2}$ 0°	$R_{2\|3}$ 54.44°	$R_{2\|4}$ 60°	$R_{2\|5}$ 114.44°	$R_{2\|6}$ 120°	$R_{2\|\bar{1}}$ 174.44°	$R_{2\|\bar{2}}$ 180°	$R_{2\|\bar{3}}$ -125.56°	$R_{2\|\bar{4}}$ -120°	$R_{2\|\bar{5}}$ -65.56°	$R_{2\|\bar{6}}$ -60°
3	$R_{3\|1}$ -60°	$R_{3\|2}$ -54.44°	$R_{3\|3}$ 0°	$R_{3\|4}$ 5.56°	$R_{3\|5}$ 60°	$R_{3\|6}$ 65.56°	$R_{3\|\bar{1}}$ 120°	$R_{3\|\bar{2}}$ 125.56°	$R_{3\|\bar{3}}$ 180°	$R_{3\|\bar{4}}$ -174.44°	$R_{3\|\bar{5}}$ -120°	$R_{3\|\bar{6}}$ -114.44°
4	$R_{4\|1}$ -65.56°	$R_{4\|2}$ -60°	$R_{4\|3}$ -5.56°	$R_{4\|4}$ 0°	$R_{4\|5}$ 54.44°	$R_{4\|6}$ 60°	$R_{4\|\bar{1}}$ 114.44°	$R_{4\|\bar{2}}$ 120°	$R_{4\|\bar{3}}$ 174.44°	$R_{4\|\bar{4}}$ 180°	$R_{4\|\bar{5}}$ -125.56°	$R_{4\|\bar{6}}$ -120°
5	$R_{5\|1}$ -120°	$R_{5\|2}$ -114.44°	$R_{5\|3}$ -60°	$R_{5\|4}$ -54.44°	$R_{5\|5}$ 0°	$R_{5\|6}$ 5.56°	$R_{5\|\bar{1}}$ 60°	$R_{5\|\bar{2}}$ 65.56°	$R_{5\|\bar{3}}$ 120°	$R_{5\|\bar{4}}$ 125.56°	$R_{5\|\bar{5}}$ 180°	$R_{5\|\bar{6}}$ -174.44°
6	$R_{6\|1}$ -125.56°	$R_{6\|2}$ -120°	$R_{6\|3}$ -65.56°	$R_{6\|4}$ -60°	$R_{6\|5}$ -5.56°	$R_{6\|6}$ 0°	$R_{6\|\bar{1}}$ 54.44°	$R_{6\|\bar{2}}$ 60°	$R_{6\|\bar{3}}$ 114.44°	$R_{6\|\bar{4}}$ 120°	$R_{6\|\bar{5}}$ 174.44°	$R_{6\|\bar{6}}$ 180°
$\bar{1}$	$R_{\bar{1}\|1}$ 180°	$R_{\bar{1}\|2}$ -174.44°	$R_{\bar{1}\|3}$ -120°	$R_{\bar{1}\|4}$ -114.44°	$R_{\bar{1}\|5}$ -60°	$R_{\bar{1}\|6}$ -54.44°	$R_{\bar{1}\|\bar{1}}$ 0°	$R_{\bar{1}\|\bar{2}}$ 5.56°	$R_{\bar{1}\|\bar{3}}$ 60°	$R_{\bar{1}\|\bar{4}}$ 65.56°	$R_{\bar{1}\|\bar{5}}$ 120°	$R_{\bar{1}\|\bar{6}}$ 125.56°
$\bar{2}$	$R_{\bar{2}\|1}$ 174.44°	$R_{\bar{2}\|2}$ 180°	$R_{\bar{2}\|3}$ -125.56°	$R_{\bar{2}\|4}$ -120°	$R_{\bar{2}\|5}$ -65.56°	$R_{\bar{2}\|6}$ -60°	$R_{\bar{2}\|\bar{1}}$ -5.56°	$R_{\bar{2}\|\bar{2}}$ 0°	$R_{\bar{2}\|\bar{3}}$ 54.44°	$R_{\bar{2}\|\bar{4}}$ 60°	$R_{\bar{2}\|\bar{5}}$ 114.44°	$R_{\bar{2}\|\bar{6}}$ 120°
$\bar{3}$	$R_{\bar{3}\|1}$ 120°	$R_{\bar{3}\|2}$ 125.56°	$R_{\bar{3}\|3}$ 180°	$R_{\bar{3}\|4}$ -174.44°	$R_{\bar{3}\|5}$ -120°	$R_{\bar{3}\|6}$ -114.44°	$R_{\bar{3}\|\bar{1}}$ -60°	$R_{\bar{3}\|\bar{2}}$ -54.44°	$R_{\bar{3}\|\bar{3}}$ 0°	$R_{\bar{3}\|\bar{4}}$ 5.56°	$R_{\bar{3}\|\bar{5}}$ 60°	$R_{\bar{3}\|\bar{6}}$ 65.56°
$\bar{4}$	$R_{\bar{4}\|1}$ 114.44°	$R_{\bar{4}\|2}$ 120°	$R_{\bar{4}\|3}$ 174.44°	$R_{\bar{4}\|4}$ 180°	$R_{\bar{4}\|5}$ -125.56°	$R_{\bar{4}\|6}$ -120°	$R_{\bar{4}\|\bar{1}}$ -65.56°	$R_{\bar{4}\|\bar{2}}$ -60°	$R_{\bar{4}\|\bar{3}}$ -5.56°	$R_{\bar{4}\|\bar{4}}$ 0°	$R_{\bar{4}\|\bar{5}}$ 54.44°	$R_{\bar{4}\|\bar{6}}$ 60°
$\bar{5}$	$R_{5\|1}$ 60°	$R_{5\|2}$ 65.56°	$R_{5\|3}$ 120°	$R_{5\|4}$ 125.56°	$R_{5\|5}$ 180°	$R_{5\|6}$ -174.44°	$R_{5\|1}$ -120°	$R_{5\|2}$ -114.44°	$R_{5\|3}$ -60°	$R_{5\|4}$ -54.44°	$R_{5\|5}$ 0°	$R_{5\|6}$ 5.56°
$\bar{6}$	$R_{\bar{6}\|1}$ 54.44°	$R_{\bar{6}\|2}$ 60°	$R_{\bar{6}\|3}$ 114.44°	$R_{\bar{6}\|4}$ 120°	$R_{\bar{6}\|5}$ 174.44°	$R_{\bar{6}\|6}$ 180°	$R_{\bar{6}\|\bar{1}}$ -125.56°	$R_{\bar{6}\|\bar{2}}$ -120°	$R_{\bar{6}\|\bar{3}}$ -65.56°	$R_{\bar{6}\|\bar{4}}$ -60°	$R_{\bar{6}\|\bar{5}}$ -5.56°	$R_{\bar{6}\|\bar{6}}$ 0°

In this way half of the possible orientations can be ruled out. Only 60 unique configurations remain. These can be classified into 4 main groups of rutile-rutile relations:

The first group is a $(301)_R$ twin configuration TW-I with the contact angle φ_{TW-I}=54.44° and the complementary φ'_{TW-I}=125.56°. This group contains 12 possible impingements of two rutile domains, six with φ_{TW-I} contact angle and six with φ'_{TW-I}.

The second group is a symmetry-related configuration TB-I with the contact angle φ_{TB-I}=60° and complementary angle φ'_{TB-I}=120°. Same as in the first group there are 12 configurations (6+6).

The third group is a $(101)_R$ twin configuration TW-II with φ_{TW-II}=114.44° (6 orientations) and complementary TW-II' with φ'_{TW-II}=65.56° (6 orientations).

The fourth group is a group with low-angle tilt configuration TB-II where complementary angles are φ_{TW-I}=174.44° and φ'_{TW-I}=5.56° (12 orientations).

All of the rutile/rutile relations from these 4 groups form eight structurally different $R_{i|j}$ interfaces, four primary ones and four complementary relations. Table 1 shows all of the possible rutile-rutile configurations ($R_{i|j}$) and the (φ) angles between the c-axes of rutile domains.

Figure 3.6a shows four Ri|j interfaces and five different H|R orientations that are a result of exsolution of rutile lamellae and their impingement during growth. Different growth directions of rutile lamellae are observed in form of banding lamellae within the

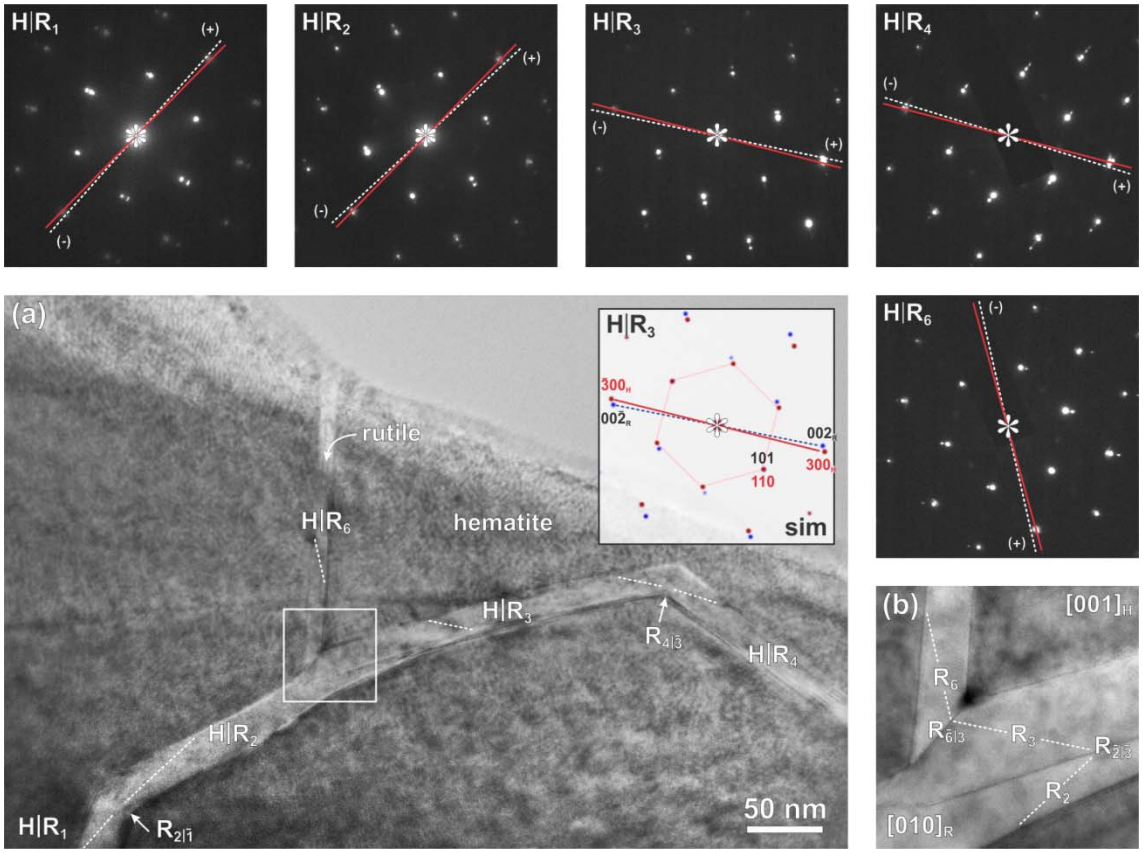


Figure 3.6: TEM analysis of rutile lamellae in hematite matrix viewed along the $[001]_H$ a) Low magnification TEM image of five rutile lamellae with different orientations and the corresponding SAED patterns. Red lines indicate equivalent $\{100\}_H$ directions and white dotted lines present the 12 possible orientations of rutile c-axes tilted for $\pm 2.75°$. b) Close-up of neighbouring $(101)_R$ and $(301)_R$ interfaces from the central part of low magnification image.

hematite matrix. The direction of rutile c-axis in each domain was determined from SAED. SAED patterns from all rutile lamellae show four successive $H|R_i$ orientations (i 1, 2, 3, 4). Although $R_1|R_2$ and $R_3|R_4$ lamellae all grow in different directions, they form the same type of rutile/rutile interface, i.e. TB-II. Especially interesting is the $R_2|R_3$ interface where, based on the orientation, the interface for the minimization of contact energy would be TW-I'. However, the formed contact is the TW-I boundary ($\varphi = 54.44°$) where the interface is five times longer than in the case of the complementary TW-I' orientation. This is the result of considerably lower energy of the coherent twin boundary compared to the incoherent interface. It can be observed in Figure 3.6a that another rutile lamella in another H|Ri orientation joins the main exsolution band. It belongs to the last of the six possible ($\pm$) exsolution directions $H|R_6$ and coincides with the $H|R_3$ lamella to form the $(101)_R$-twin interface $R_{6|3}$. In the close-up of this coincidence situation (Figure 3.6b), one can see that the ($-$) pole of R_6 forms a $(101)_R$-twin with the ($+$) pole of R_3, and the ($-$) pole of R_3 forms a (301)-twin with the ($-$) pole of R_2. The corresponding angular relations for each particular configuration can be found in Table 3.1.

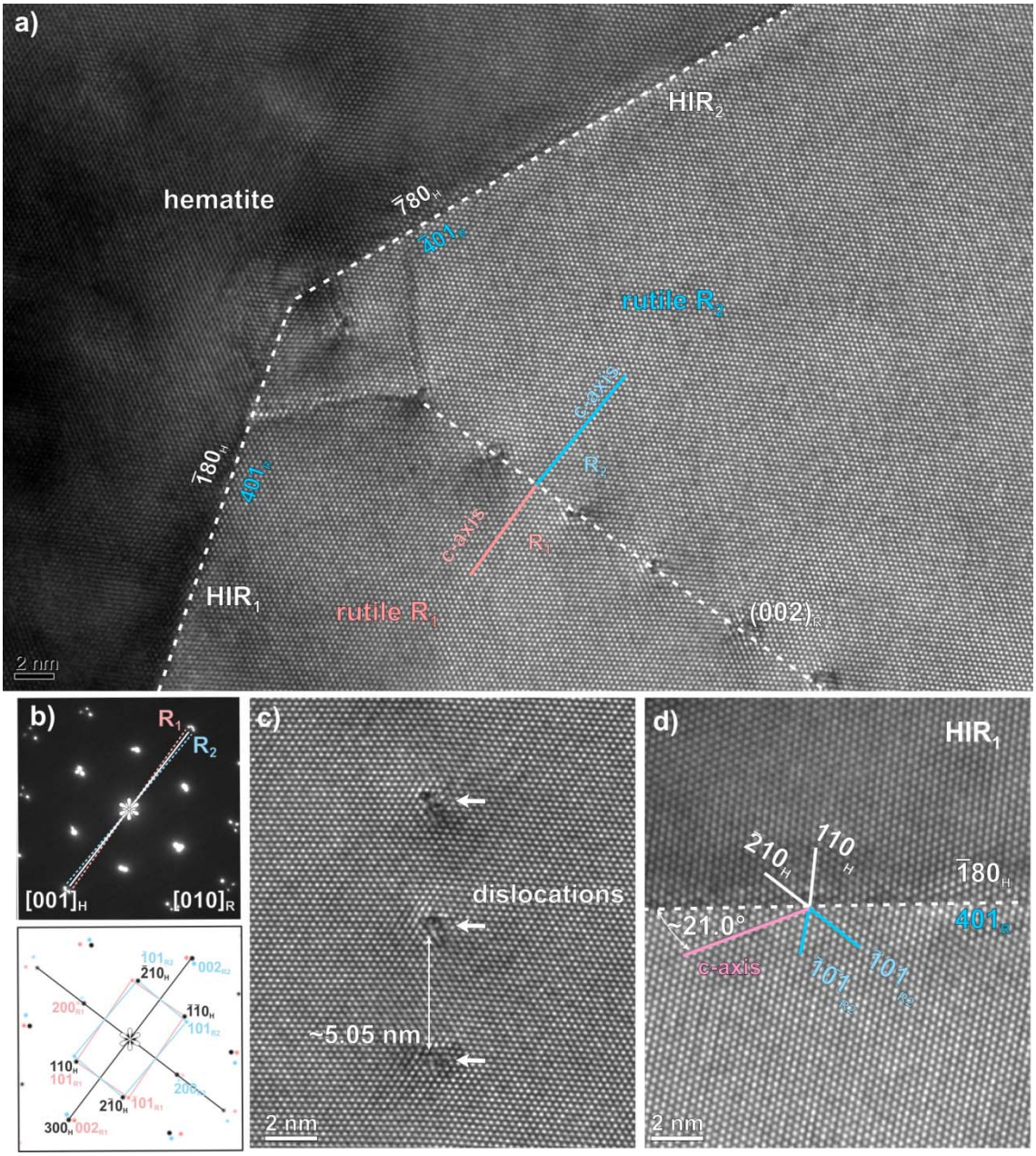


Figure 3.7: HRTEM analysis of the low-angle grain boundary and the rutile/hematite interface. a) The small misorientation between two rutile domains is compensated with regularly distributed dislocations. b) SAED of two rutile domains and the hematite matrix and simulated pattern according to the OR-2 law. c) A close-up of edge dislocations at the LAGB which are distributed on every ~5.5 nm. d) The rutile/hematite interface is presented with a dashed line. Interface is tilted for ~21° with respect to the rutile c-axis. The interface corresponds to $\{170\}_H$ and $\{401\}_R$.

Figure 3.7a is a HRTEM image of two rutile domains forming a low angle boundary. The grain boundary is disrupted by evenly spaced edge dislocations. Net Burger vector around the dislocation core has a length of the rutile c-axis. The misfit between two rutile domains is compensated by the introduction of two half-$(101)_R$, and the Burgers vector of the dislocation can be presented as $\mathbf{b} = \mathbf{b_1} + \mathbf{b_2} = ½[101] + ½[\bar{1}01]$. The energy

of such a dislocation is expected to be lower (Nakamura, et al., 2009) since it comprises of a combination of two edge dislocations in the *hcp* oxygen sublattice.

The expected tilt angle of this type of boundary is θ=2.78°. The calculated distance for the compensation of ½b=$d(002)_R$ (0.1479 nm) in one domain is $D=d(002)_R/\tan(\theta)$=3.05 nm. This is the expected distance between two dislocations, however, the average distance measured from HRTEM images is larger, and it is 5.05 nm. This suggests that the actual angle between rutile c-axes on both sides of the boundary is larger. The expected angle enclosed by the c-axes of rutile domains would be 174.4° (Table 3.1), however angle measured from the EDP is ~175.5°. The difference between the theoretically predicted and actual angle is for ~1° larger, similar to the observed angle in the $(101)_R$ twin boundary (Figure 3.5). Consistently the misorientation angle is smaller than expected by the OR-2 which explains larger distances between dislocations. The tilt angle measured from lattice image is θ'= 2.2°.

If we now look at the hematite/rutile interfaces we can observe that they are coherent and without dislocations. Based on OR-2, one would anticipate that $(110)_H$ planes of hematite would form a coherent interface with $(101)_R$ planes of rutile. If $(110)_H$ lattice planes are viewed across the $H|R_2$ interface, the equivalent planes in the rutile lattice are deflected for a small angle, which is a result of tetragonal deformation of the rutile's *hcp* lattice with respect to hematite. However, the same set of planes observed on the other interface $H|R_1$, they pass the boundary without deflection from rutile planes. The interface between rutile and hematite in this case is not a simple low-index plane, but it is composed of steps in the common oxygen sublattice. The steps are composed of low-index facets at the atomic scale: $3\cdot(110)_H + 2\cdot(\bar{1}20)_H$ and $3\cdot(200)_R + 2\cdot(101)_R$. The angle measured between $H|R_1$ interface and the rutile c-axis is ~21° and this angle matches the $(401)_R$ (the exact angle is 21.2°) belonging to $\{401\}_R$ family of planes. In the same way, the interface plane is identified $(1\bar{8}0)_H$, belonging to the $\{170\}_H$ family of planes.

For calculating the misfit for the $H|R_1$ interface I used a linear combination of basic lattice vectors corresponding to interface planes of rutile and hematite since there are no physical lattice planes running normal to the interface. The interface planes were presented as fractions of lattice vectors, i.e., $(401)_R \equiv (1/1,\ 0,\ 1/4)_R$ and $(170)_H \equiv (1/7,\ 1/1,\ 0)_H$, where the distances between common points, d_R and d_H, are given by:

$$d_R^2 = a_R^2 + (4c_R)^2 \tag{4.1}$$

$$d_H^2 = [(7\ \cdot a_H)^2\ +\ b_H^2\ +\ 2\ \cdot\ (7\ \cdot\ a_H)\ \cdot b_H \cdot\ \cos(\gamma\ )]/3 \tag{4.2}$$

where a_R = 0.45937 nm, c_R = 0.29587 nm; $a_H = b_H$ = 0.5038 nm, γ = 120°. Based on the calculated values for d_R=1.2695 nm and d_H=1.2679 nm, rutile and hematite seem to perfectly match at the interface. These distances also correspond to five interatomic distances $d'_{Ti\text{-}Ti}$ and $d'_{Fe\text{-}Fe}$ when they are projected to the interface from each structure. From these calculated values, the misfit (δ) between rutile and hematite lattice can be calculated according to the following equation (Löffler & Mader, 2003):

$$\delta = \ 2\left|\frac{d_R - d_H}{d_R + d_H}\right| \tag{4.3}$$

Determined misfit for the $(170)_H|(401)_R$ interface is δ = 0.13 %. The Vernier period of a misfit (D) that represents the distance between the misfit dislocations is given by the following equation:

$$D = \frac{d_H \cdot d_R}{|d_H - d_R|} \tag{4.4}$$

Theoretically, the length of ~200 nm would be needed to compensate one extra interatomic distance of the smaller lattice. The length is calculated by dividing calculated Vernier period by the number of projected interatomic distances, d'_{Ti-Ti} and d'_{Fe-Fe}. This indicates that rutile and hematite in this way form an almost perfect and coherent interface that results in high-index lattice planes. The lattice mismatch is probably compensated by relaxation of both lattices, or by steps to neighbouring atomic planes, and not by formation of dislocations. However, the two lattices show a slight rotational misalignment of θ=0.59° away from OR-2, whichtranslates to:

OR-3: $<010>_R$ $\{401\}_R$ || $<001>_H\{170\}_H$

3.4 Exsolution Processes in the Rutile/Hematite Intergrowths

Observations from $[001]_H$ confirmed that the growth of rutile lamellae is completely controlled by the structure of hematite matrix, suggesting that the origin of Ti ions for rutile formation is from the parent hematite. Although the EDS analyses showed that hematite matrix contains up to 6 at% of Ti, and rutile contains up to 1 at% of Fe, no indications for some exsolution processes were observed along this zone axis. That is why the sample was also observed from $[100]_H$. The results are presented in Figure 3.8.

The sample has a typical appearance of the ilmenite-hematite solid solutions (see Figure 1.10) with Ti-rich lens shaped precipitates with thickness up to 20 nm, and length of several-hundred-nanometers. It is interesting to observe that the region next to the rutile lamellae has no precipitates and that the size of the precipitates increases with the distance from rutile lamellae (Figure 3.8a). Bulk hematite matrix contains up to 6 at% of Ti, depleting gradually to almost pure hematite composition near the hematite/rutile interface. Two types of hematite/rutile relations are observed: (1) prismatic with $(030)_H$ | $(301)_R$ interface and (2) basal with $(006)_H$ | $(020)_R$. Both of them obey OR-2, and are presented with sharp and coherent interfaces at atomic level. In the region close to rutile lamellae, diffusion paths are also observed with general direction toward the rutile lamella and approximately parallel to the basal planes of hematite (Figure 3.8b). EDS analyses with nanobeam probe size have indicated Ti enrichment along the observed diffusion paths. This indicates that diffusion paths have served as pathways for Ti migration toward the rutile exsolution. Ti migration pathways indicate the change of the diffusion kinetics. The Ti atoms probably stay frozen in the diffusion pathways toward rutile lamellae. The first step in rutile exsolution is its nucleation perpendicular to basal planes of hematite producing coherent prismatic relations. The next step is the growth of lamellae parallel to basal planes of hematite in the direction of ilmenite precipitates that serve as Ti-supply. The FFT of the precipitates also confirmed that they are ilmenite, since it has two additional diffraction spots that distinguish hematite from ilmenite in this zone axis. The presence of the c-glide plane in hematite leads to the disappearance of reflections of the type hhl, l = 2n + 1 from the diffraction patterns.

The last process in the transformation of rutile/hematite intergrowths is exsolution of hematite in rutile domains. With the BF-STEM we observed that rutile crystals contain extended defects producing irregular light and dark grey patches (Figure 3.9a).

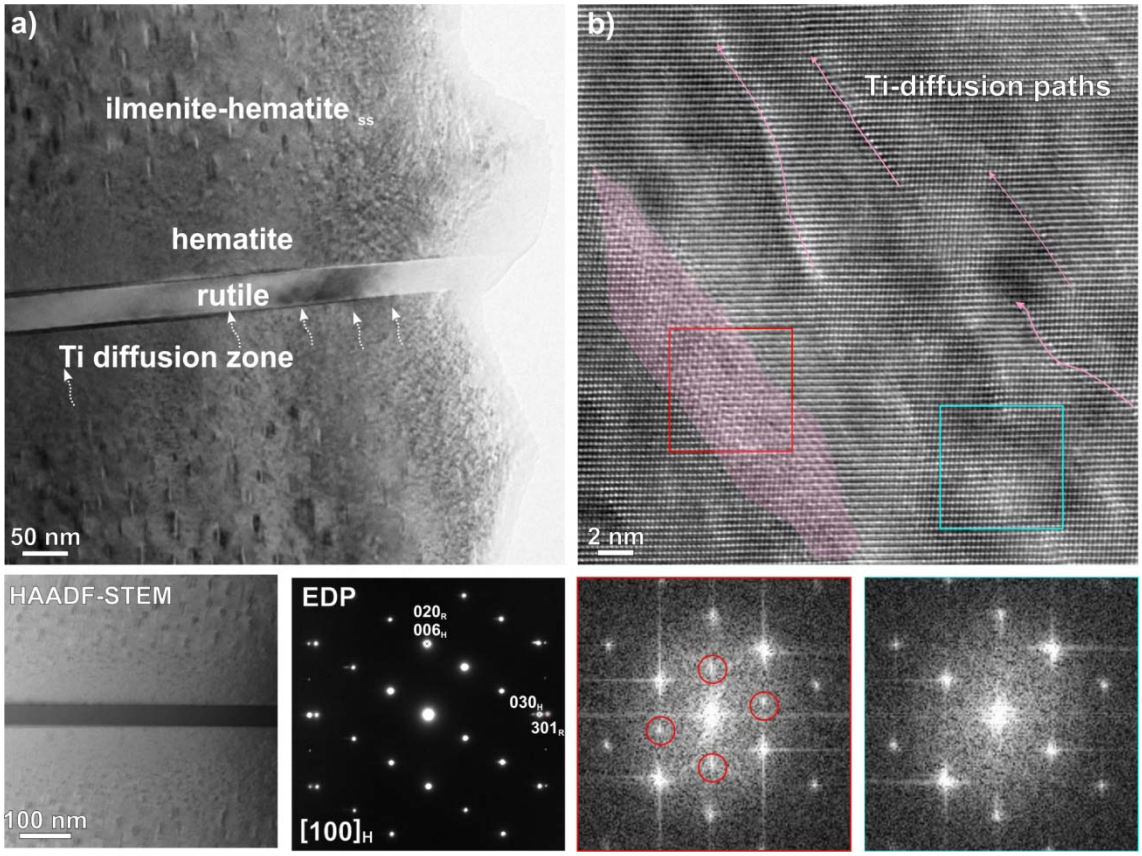


Figure 3.8: TEM analyses of rutile/hematite intergrowths viewed along $[100]_H$ projection a) Low-resolution TEM image of rutile lamella in the ilmenite-hematite$_{ss.}$ The direction of Ti diffusion is presented with white arrows. Area around rutile lamellae is hematite that is best visible in the HAADF image of the same area. The SAED shows that the interface is $(030)_H \mid (301)_R$ b) On the HRTEM image of the hematite-ilmenite$_{ss}$ the Ti-diffusion paths are marked with arrows and the FFT of precipitates shows the presence of additional diffraction spots characteristic for the precipitates of ilmenite.

Z-contrast STEM and EDS confirmed an increased amount of Fe in these areas. The precipitates show specific crystallographic orientations. HRTEM images showed that the width and length of exsolutions are limited by lattice matching in the two growth directions. Diffraction analyses showed that rutile with Fe-rich exsolutions obey OR-2, while the interfaces are different than in the case of rutile growth in hematite matrix. The misfit between $(101)_R$ and $(110)_H$ is only 0.81% and therefore the lamellae can grow without restrain in these directions, and as a result coherent $301_R||030_H$ interfaces are formed. Fine scale exsolution of hematite from hosting rutile is most probably a result of solid-solution separation process at lower temperatures.

3.5 Mechanism of Formation of Oriented Rutile/Hematite Intergrowths

The samples of the rutile/hematite intergrowths from Mwinilunga originate from placer deposits in the Chief Mumena area between the districts of Mwinilunga and Solwezi in NW Zambia. Gabbroic bodies associated with mafic magmatism are reported in this

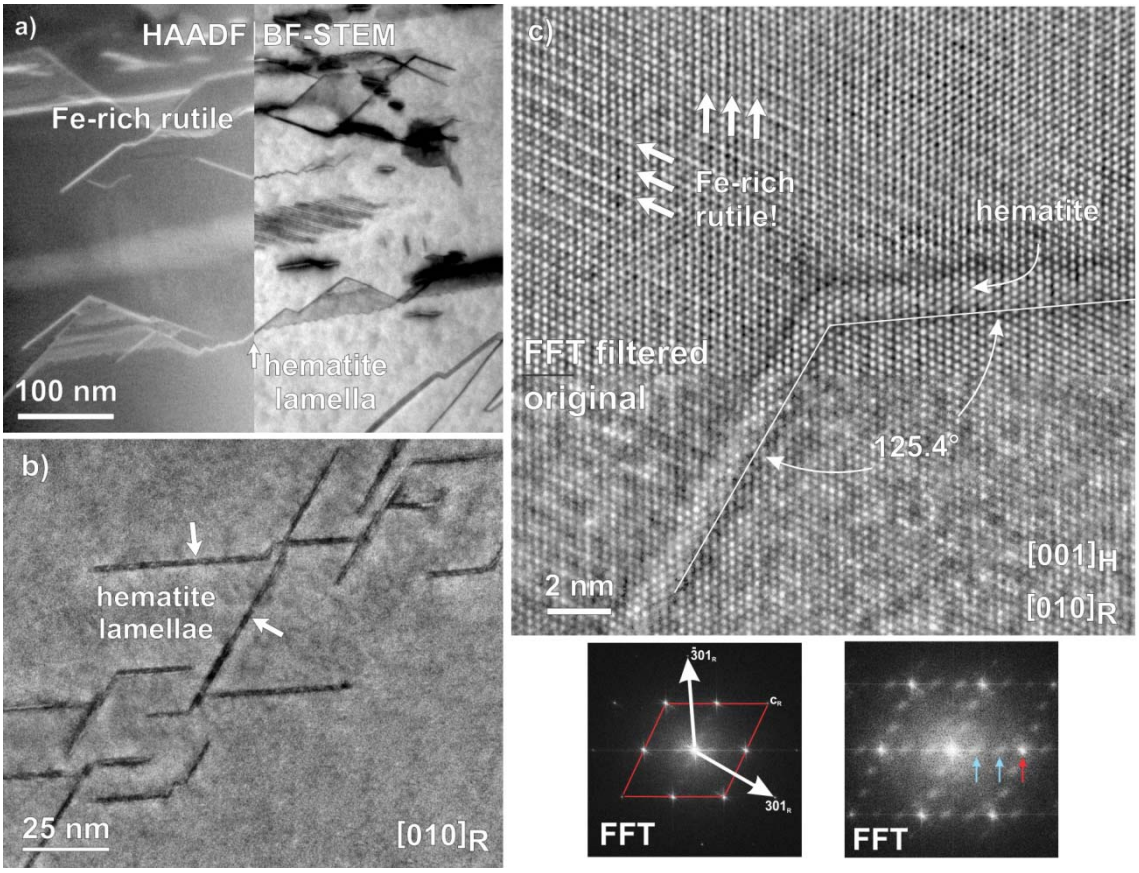


Figure 3.9: Hematite exsolutions in rutile viewed along $[010]_R$ a) Bright-field and high angle annular dark-field (HAADF) STEM image of rutile show Fe-rich parts which appear brighter in HAADF image. b) Phase-contrast TEM image of hematite exsolutions shows their exsolution in two direction dictated by tetragonal structure of rutile. c) HRTEM image shows rutile periodicity in $\{101\}_R$ direction that is best visible in FFT. The SAED shows that hematite exsolutions obey OR-2 and hematite forms coherent $\{301\}_R||\{030\}_H$ interfaces.

region (Porada & Berhorst, 1998). Crystals from this locality usually have thick tabular shape characteristic for ilmenite-rich hematite (McEnroe, et al., 2005; Palache, et al., 1952; Taylor, 1963). The most likely source of the samples are mafic dykes that intrude the pre-katanga basement extending from NW Zambia to Democratic Republic of Kongo (Key, et al., 2001) since the large ilmenite-rich crystals are distinctive for Fe-Ti rich differentiates of mafic and ultramafic magmas (Bateman, 1951; Ramdohr, 1979) formed in isolated discordant bodies emplaced in pegmatite like dykes, as described in the Bushveld complex (Scoon & Mitchell, 1994).

Based on experimental data we were able to reconstruct the mechanism of transformation of parent crystal to rutile/hematite intergrowths. From the rutile/hematite ratio in the interior of the sample we could roughly estimate the composition of starting material. The ratio between rutile and hematite in the interior of the samples is close to 1:1, suggesting that the parent crystal had approximately the composition $Ilm_{67}Hem_{33}$. The temperatures at which complete solid solutions between ilmenite and hematite are formed in mafic rocks are between 1050 and 1150 °C (Ariskin & Barmina, 1999; Nielsen & Dungan, 1983; Scoon & Mitchell, 1994; Thompson, 1976). The complete solid solutions are formed through the substitution of Fe^{2+} and Ti^{4+} pairs

for two Fe^{3+} ions to preserve the charge balance (Burton, 1985; Ishikawa, 1958; McEnroe, et al., 2005). The composition of the solid solution is controlled by the fractions of different oxidation state of iron which is a direct consequence of the oxygen fugacity, f_{O_2} (Buddington & Lindsley, 1964). At higher temperatures the conditions are more reducing resulting in a larger fraction of Fe^{2+} ions and therefore in a more ilmenite-rich phase (Figure 3.10a). With temperature decrease, the crystalizing phase in the melt is depleted and its composition shifts to the hematite rich part of the phase diagram (see Figure 1.7). However at lower temperatures ilmenite$_{ss}$ and hematite$_{ss}$ unmixed into separate phases of ilmenite and hematite by diffusion controlled decomposition (Rao & Rao, 1965) that can be presented with the formula (Figure 3.10b):

$$\mathrm{HI}: (Fe_x^{2+}, Fe_{2-2x}^{3+})Ti_x^{4+}O_3 \rightarrow x \cdot Fe^{2+}TiO_3 + (1-x) \cdot Fe_2^{3+}O_3 \tag{5.5}$$

This decomposition is a topotaxial precipitation of hematite in ilmenite, or vice versa, depending on the composition of parent phase (precipitation of hematite in ilmenite-rich phase and precipitation of ilmenite in hematite rich solid solution). The size of the precipitate, on the other hand, depends on the kinetics of a cooling where the nanosized precipitates are formed during fast cooling and their size increases as the cooling rate decreases. At the temperatures of miscibility gap, a typical lamellar texture is formed and it is not present in the minerals that crystallize below these temperatures (McEnroe, et al., 2005). The lamellar texture is presented in the form of lamellae perpendicular to the basal plane; while in the basal plane the precipitates have a form of irregularly shaped patches. The texture observed in our samples best resembles the texture of the samples of hemo-ilmenites from Allard-lake with the composition of $Ilm_{70}Hem_{30}$ (Carmichael, 1961; Morisset, et al., 2010).

When the majority of iron and titanium from the melt is used for crystallization of the parent crystal and therefore the concentration of crystallizing phase is depleted in melt, the remaining volatiles start to act as an external buffer of constantf_{O_2}. At this point of crystallization the f_{O_2} starts to control phase composition of crystalizing phases (Carmichael & Nicholls, 1967). With the decrease of temperature, the activity of oxygen is increasing and the Fe^{2+} from ilmenite starts to oxidize to Fe^{3+} that forms hematite and rutile (Figure 3.10c):

$$RHI: 2 \cdot Fe^{2+}TiO_3 + {}^1\!/_2 \cdot O_2 \rightarrow Fe_2^{3+}O_3 \ + 2 \cdot TiO_2 \tag{5.6}$$

Oxidation of iron starts at the surface where the crystal is in contact with the oxidizing fluids. The oxidation of iron cations triggers complex reorganization of cations in the oxygen sublattice of a parent crystal. Ferric ions migrate toward the surface where they form a fresh hematite layer and leave behind free sites for formation of rutile. The cation rearrangement is achieved within the common *hcp* oxygen sublattice. In ilmenite one-third of octahedral sites is occupied by Ti^{4+} and one-third with the Fe^{2+} cations and in hematite both two-thirds cationic sites are occupied by Fe^{3+}. On the other hand, the rutile structure has only one-half of all octahedral sites occupied by Ti^{4+} which makes it more vacant compared to corundum type structure. If the rutile and hematite are formed from ilmenite, then the titanium cations rearrange from one third of cation sites to occupy one half and form a rutile structure; the iron is oxidized to form hematite, then one-third of iron must leave the structure (Figure 3.11). The removal of excess iron is most likely achieved through empty octahedral sites (Figure 1.5.c) that serve as diffusion paths (Amami, et al., 1999; Hallström, et al., 2011; Sabioni, et al., 2005). The diffusion of Fe is several magnitudes faster along the c-axis of corundum type structure than in the

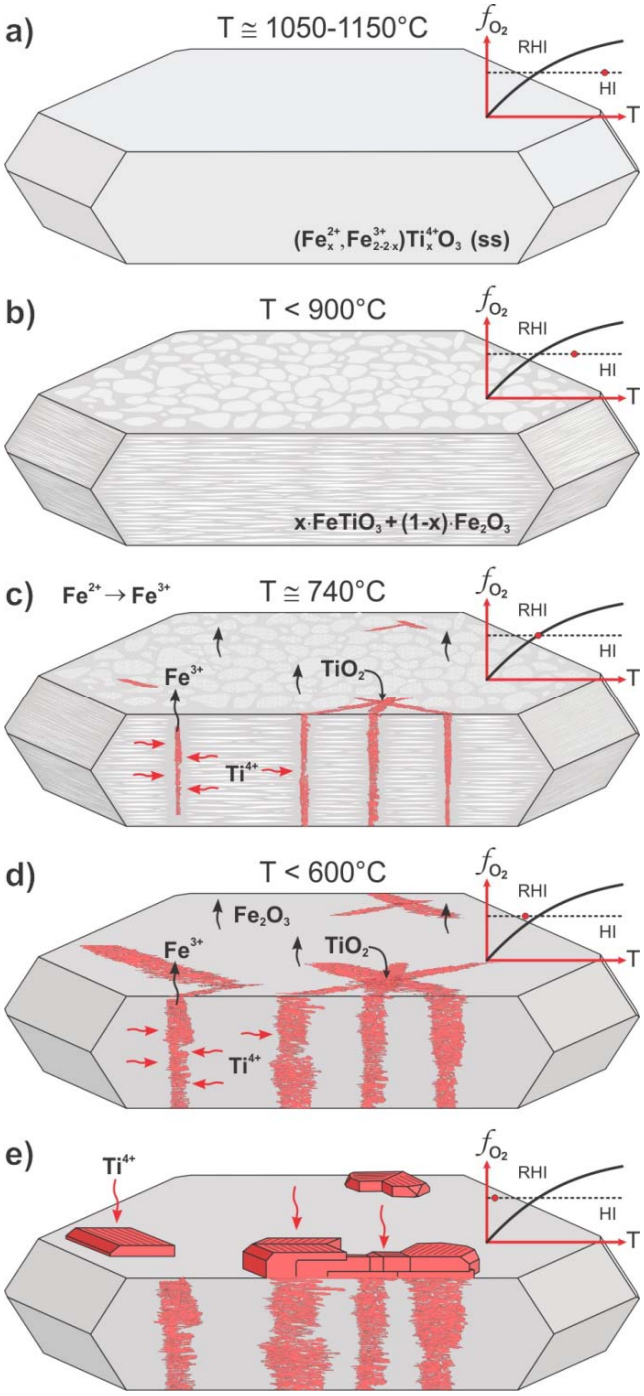


Figure 3.10: Schematic presentation of mechanism of transformation of rutile/hematite intergrowths from Mwinilunga, Zambia. a) Parent hemo-ilmenite was formed at temperatures between 1050 and 1150 °C; b) At temperatures below 900 °C ilmenite and hematite separate to form characteristic lamellar textures. c) With further decrease in temperature, iron is oxidized to Fe^{3+} and it diffuses along the c-axis. The iron diffusion triggers the nucleation of rutile lamellae and formation of rutile pillars. d) With the progression of oxidation, nucleated rutile pillars grow laterally into the parent crystal at the expense of ilmenite layers. e) In pneumatolytic stage of crystallization, TiO_2 recrystallize on the surface.

prism direction. With the out-diffusion of Fe, empty sites for formation of rutile are formed. This explains the formation of a pillar-like structure along the c-axis observed in the prismatic orientation (Figure 3.10d). Titanium diffusion, on the other hand, is sluggish compared to iron diffusion (Petersen, 1970) and it is fastest along the basal planes of ilmenite (Ishikawa & Syono, 1963; Nord & Lawson, 1989). This was also confirmed in our sample where we observed Ti-diffusion paths along basal planes and by Ti-depleted zones near the rutile lamellae in HRTEM (Figure 3.8b). Since Ti is less mobile parallel to the c-axis of parent ilmenite, rutile starts to nucleate in vertical direction and then progressively grows along the basal planes. During growth, some iron remains in the rutile structure since rutile can incorporate up to ~1 at% of ferric iron at 800 °C (Wittke, 1967). Together with the growth of rutile pillars, nanosized ilmenite precipitates are dissolved. The parent hemo-ilmenite is almost completely transformed to rutile and hematite and the remaining ilmenite is observed only in the interior of the sample.

The transformation is controlled by the structure of parent mineral, and the complexity of the formed rutile-rutile domains depends on the kinetics of the reaction. The reaction rate is defined by the following processes:

(1) surface oxidation of Fe;
(2) rate of Fe-diffusion through the parent crystal;
(3) exsolution of rutile with Fe release;
(4) Ti-diffusion rate through hematite and
(5) dissolution of ilmenite.

Since the diffusion paths in observed samples were quite long, the first two processes are rate determining in the case of rutile/hematite intergrowths from Mwinilunga, Zambia. When the f_{O_2} is low, the reaction is limited by the supply of oxygen and therefore the whole transformation is limited by the oxidation of iron. On the other hand, when $f_{O_2}$is high, the oxidation is fast and the Fe-diffusion controls the kinetics of the transformation. Therefore, at specific p-T conditions, the reaction rate is controlled by f_{O_2}; when the surrounding fluids are rich with oxidizing agents, all iron that diffuses out from the parent crystal will instantly form hematite, while in the fluids that are not highly oxidizing, the processes 2-5 are slowed down because of the surface oxidation. Since the surface oxidation controls how much iron will diffuse out from starting phase it also controls rutile exsolution since rutile is formed by Ti cation rearranged on empty Fe-sites. During the slow exsolution, rutile will adopt energetically most favourable directions in oxygen sublattice since it has enough time to establish an equilibrium interface with the parent hemo-ilmenite. During the slow nucleation the rutile forms an interface that produces the best matching interface under given p-T conditions (Putnis, 1978, 1995). Topotaxial growth of rutile is then controlled by structural coherency between hematite and rutile during the exsolution of rutile lamellae, and therefore the resulting orientation relationship is thermodynamically driven and it is different depending on the temperature of rutile exsolution from parent phase. In the samples from Mwinilunga observed relationship is best described by OR-2 that can also be seen in other natural rutile/hematite intergrowths (Armbruster, 1981; Daneu, et al., 2014; Daneu, et al., 2007) and exsolutions of hematite in rutile (Putnis, 1978). In the case of Mwinilunga intergrowths, rutile shows an angular deviation of 0.59° from the OR-2 producing a new orientation relationship OR-3. Instead of the expected low-index interface $(010)_{\mathrm{H}}|(301)_{\mathrm{R}}$ which is the equilibrium interface formed in the OR-2 (Daneu, et al., 2014), we observed a $(170)_{\mathrm{H}}|(401)_{\mathrm{R}}$. The interface can be presented through the steps of low index facets: $3 \cdot (110)_{\mathrm{H}} + 2 \cdot (\bar{1}20)_{\mathrm{H}}$ and $3 \cdot (200)_{\mathrm{R}} + 2 \cdot (101)_{\mathrm{R}}$.

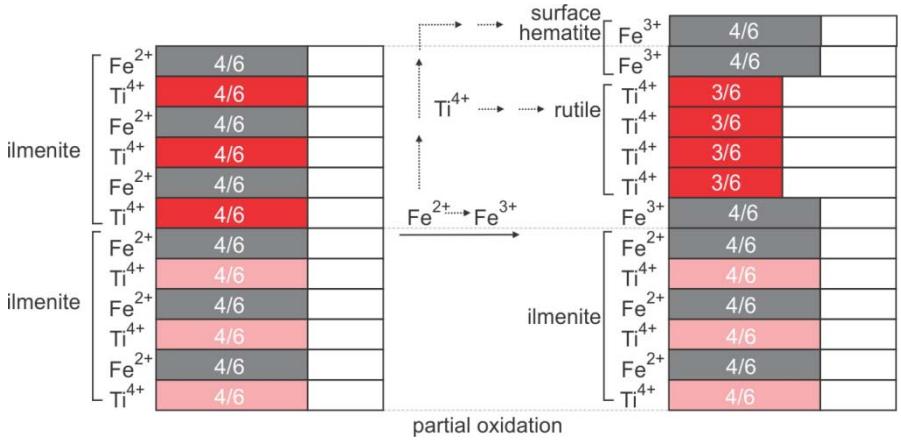


Figure 3.11: Schematic presentation of cation rearrangement in the ilmenite lattice during oxidation. In ilmenite structure, both Ti and Fe occupy 2/3 (4/6) of octahedral positions in octahedral layers. After the oxidation titanium rearrang to form rutile that has 1/2 (3/6) of octahedral positions occupied resulting in the formation of hematite surface layer.

Such interface, in effect, generates even better lattice matching between rutile and hematite. Taking into account unit-cell parameters of ideal rutile (Howard et al. 1991) and hematite (Blake et al. 1966) at ambient conditions, the calculated misfit for this interface is as low as 0.13 %. Compared to misfit of the rutile interface with ilmenite $\delta(100)_I|(301)_R$ = 1.81 % (Daneu, et al., 2007), or corundum $\delta(110)_C|(101)_R$ = 0.53 % (Daneu, et al., 2014) reported in literature, the rutile/hematite $(170)_H|(401)_R$ interface has the smallest misfit. During slow cooling the system is always in near equilibrium state, and the minimization of interfacial energy is accomplished by the best match between two phases. Since the unit cell parameters change with the temperature it results also in the change of the misfit, and the smallest misfit is at ~740 °C (Table 3.2). This presents the most probable temperature of rutile exsolution (Nešković, et al., 1977).

During the formation of rutile lamellae, some iron is present in the rutile structure and during cooling the excess of iron exsolutes in the form of hematite lamellae. The lamellae are exsoluted through the intermediate Fe-rich phase with the structural coherency with rutile. This structure is characterized by the tripling of $\{101\}_R$ and it presents the modulated structure comprising of chemical and structural components of both end phases. These kinds of modulated structures are characteristic for chemically induced transitions between different structures crystallizing within a common sublattice (Takeuchi & Hashimoto, 1990). The hematite exsolved from rutile forms the low index interface $\{301\}_R|\{030\}_H$; however Hwang (2010) observed high index equilibrium interface $(140)_H||(501)_H$ (OR-4) with the low angle tilt boundary in exsolved hematite. The sample they investigated was formed in rutile from ultrahigh-pressure metamorphic rocks (eclogite) in the temperature range of 900-1100 °C. This again suggests that equilibrium interface is dependent on the temperature of exsolution, and the OR-3 interface $(170)_H||(401)_R$ is formed at lower temperatures, while the OR-4 is a result of lattice matching at higher temperatures. However, the interface $(010)_H|(301)_R$ never meets the crossover of lattice matching, and it is probably not an equilibrium interface (Hwang, et al., 2010). The calculated mismatches are only orientational and for more reliable results for estimation of the exsolution temperature the dependence of the cell parameters versus temperature should be measured on the particular phase system.

Table 3.2: Temperature dependence of lattice misfit (δ) for different interfaces. The lattice misfit was calculated based on the Eq. 4.3 for $(010)_H|(301)_R$ interface (OR-2); $(170)_H$ $(401)_R$ interface (OR-3) and $(140)_H$ $(501)_R$ interface (OR-4). Unit cell parameters: [a] Howard et al. (1991), [b] Nešković et al. (1977), extrapolated for temperatures above 890 °C. The values for lattice misfit at ambient conditions are larger for OR-3 and OR-4 due to different data for hematite.

T (°C)	Rutile:a,c (nm)[a]	Hematite: a (nm)[b]	δ_{OR-2} (%)	δ_{OR-3} (%)	δ_{OR-4} (%)
20	0.4593 , 0.2959	0.5036	-0.77	+0.18	+0.69
250	0.4600 ; 0.2965	0.5046	-0.76	+0.18	+0.70
300	0.4603 ; 0.2966	0.5049	-0.79	+0.15	+0.67
460	0.4608 ; 0.2974	0.5059	-0.76	+0.20	+0.72
600	0.4616 ; 0.2977	0.5071	-0.88	+0.08	+0.59
670	0.4617 ; 0.2980	0.5080	-0.94	+0.02	+0.54
890	0.4625 ; 0.2988	0.5094	-1.00	-0.04	+0.49
1060	0.4634 ; 0.2992	0.5108	-1.13	-0.17	+0.36
1190	0.4639 ; 0.2997	0.5125	-1.31	-0.34	+0.18
1350	0.4645 ; 0.3002	0.5146	-1.56	-0.59	-0.07
1480	0.4650 ; 0.3006	0.5162	-1.74	-0.77	-0.25

The final stage of the formation of rutile/hematite intergrowths from Mwinilunga, Zambia, is the growth of larger rutile crystals on the surface of the hematite crystal. The prismatic form observed on the surface of our samples is characteristic for pneumatolytic phases (Ramdohr, 1979). The orientation of surface crystals is controlled by the exposed rutile domains from the interior of the sample. The $\{101\}_R$ twins are dominant since it is the most stable interface configuration in rutile (Lee, et al., 1993). Since at this point the rutile growth is not restrained by hematite matrix they develop crystallographic faces with the lowest surface energy. In the final stage, crystals were also exposed to a hydrothermal solution that caused hydrolysis of hematite and formation of Fe-hydroxides in the pores and cracks. This suggests that the pH of the fluids was neutral to alkaline since the acidic conditions would lead to rapid leaching of Fe^{3+} (Janssen, et al., 2010). The mechanism of formation of rutile/hematite intergrowth from Mwinilunga, Zambia, is presented in Figure 3.10.

From these investigations on natural rutile/hematite intergrowths I was able to reconstruct their formation mechanism. In the next part of the thesis I will try to experimentally replicate the transformation by heat treatment of ilmenite single crystal in air atmosphere.

Chapter 4

Topotaxial Transformation of Ilmenite Single Crystal During Oxidation in Air

4.1 Characterization of the Starting Sample and Experimental Procedure

In the second part of my thesis I studied oxidation of ilmenite to rutile and hematite under controlled conditions (atmosphere, temperature and time of oxidation). In this part of my study I used a single ilmenite crystal from Mt. Zagi in Pakistan that was 3 cm in diameter and 0.5 cm thick. It had characteristic thick tabular crystals with well-developed basal and pyramidal faces (see Figure 1.6). The orientation of c-axis was evident from crystal's morphology, and the *a* and *b* axes were determined from recorded XRPD pattern of one of the pyramidal planes, identified as the plane $(012)_I$ (Figure **4.1a**). After indexing the crystal, I cut it into 2.5 mm cubes with $[110]_I$, $[1\bar{1}0]_I$ and $[001]_I$ as the main crystallographic directions parallel to the edges of the cubes (Figure 4.1b).

The semi-quantitative chemical analysis of the starting ilmenite by SEM/EDS showed that the starting ilmenite is Mn-rich. The sample is homogeneous in composition throughout the whole sample. The chemical composition represents the average measurement of 6 spectrums on different parts of sample (Table 4.1.). Mn is replacing iron (Fe) in an equimolar ratio corresponding to $(Fe_{1-x},Mn_x)TiO_3$ solid-solution series between ilmenite ($FeTiO_3$) and pyrophanite ($MnTiO_3$), with an empirical composition $Fe_{0.58}Mn_{0.42}TiO_3$. Equimolar exchange of iron and manganese cations indicates that Ti^{4+} ions are compensated by divalent Mn and Fe (Wu, et al., 2010).

XRPD analysis of the starting sample shows a systematic shift of reflections towards lower Bragg angles, consistent with the chemical composition of the sample (Figure 4.2.). The unit-cell parameters of natural Mn-ilmenite are: a, b = 5.110 Å and c = 14.168 Å (determined from experimental XRPD), placing the mineral on the tie-line between ilmenite (a, b = 5.0884 Å and c = 14.0855 Å; (Wechsler & Prewitt, 1984)) and pyrophanite (a, b = 5.1395 Å and c = 14.2829 Å; (Kidoh, et al., 1984)). Both measurements thus place the sample at the mid of the solid-solution series, which makes it ideal for studying the mobility of Fe and Mn during the oxidation process.

The oriented cubes cut from the starting Mn-ilmenite crystal were heated in a tube furnace in the air atmosphere with the heating and cooling rates of 10°/min. The selected

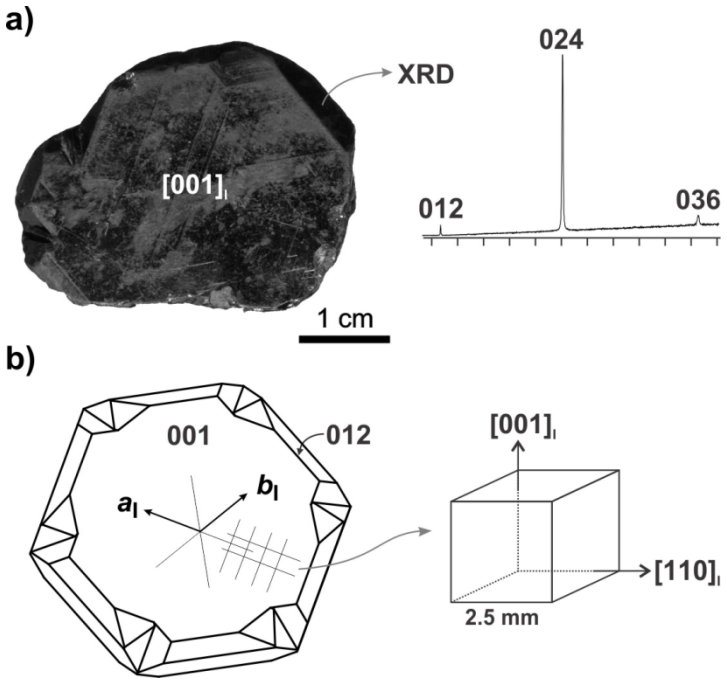


Figure 4.1: Ilmenite single crystal from Zagi mountain, Pakistan. a) Photograph of ilmenite single crystal used for investigation of topotaxial ilmenite oxidation processes. On the right side is the XRD pattern of the crystal plane indicated by arrow. b) Schematic presentation of cutting of the starting crystal into oriented cubes with edges parallel to $[001]_I$ and $[110]_I$ directions.

annealing temperatures were 600 °, 700 °, 800 °, 900 ° and 1000 °C and the annealing times were 1, 12 and 100h. Prior to and after the heating, the weight of cubes was measured in order to follow the mass change during oxidation, Δm (in %), which was used to determine the oxidation rate R_{ox}. Oxidation rates were calculated according to the following equation:

$$R_{ox} = \frac{\Delta \mathrm{m}}{\Delta m_0} \cdot 100\% \tag{4.1}$$

where Δm_0 is a theoretical mass gain of 5.28 wt% that would correspond to acompletely oxidized sample taking into account the empirical Fe:Mn ratio in the starting sample. For characterization of starting sample and annealing products I used XRPD, SEM and TEM.

4.2 Phase Composition of the Heated Ilmenite Samples

XRPD analyses of starting Mn-ilmenite reference and samples fired for 12 hours at different temperatures between 600–1000 °C are shown in Figure 4.2. Phase composition of starting ilmenite and the compositions of the heat-treated samples were determined by powder X-ray diffractometry (XRD; PW1710, Philips, Germany) using Ni-filtered Cu-K_α radiation in the range 2θ = 10°-60° with a step of 0.017 and recording time of 1 s/step. Untreated sample shows reflections that correspond to a member of solid-solution series

Table 4.1: EDS analyses of starting ilmenite sample.

	Ti (at%)	Fe (at%)	Mn (at%)
Spectrum 1	48.96	29.35	21.69
Spectrum 2	49.34	29.72	20.94
Spectrum 3	49.28	29.54	21.18
Spectrum 4	49.55	29.35	21.09
Spectrum 5	50.09	28.29	21.62
Spectrum 6	49.12	29.19	21.69
Mean value	49.39 ±0.40	29.24±0.50	21.37±0.33

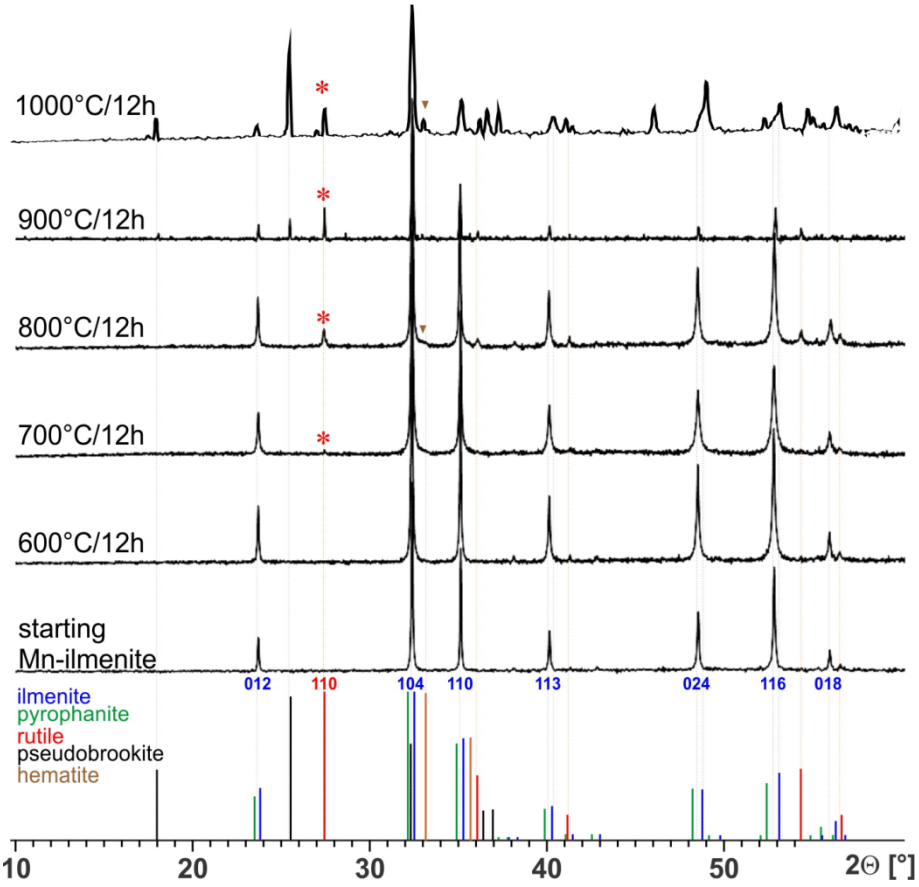


Figure 4.2: XRD diagrams of untreated ilmenite and samples heated at different temperatures from 600-1000 °C for 12 hours. At the bottom of the image the positions of the peaks of the main phases and their relative intensities are schematically presented. The rutile reflections are marked with red asterisk, while the weak hematite reflections are pointed with the arrow.

between ilmenite and pyrophanite (Wu, et al., 2010). No splitting of the reflections is observed. The sample fired at 600 °C shows no products, which is in accordance with previous high temperature oxidation studies of ilmenite (Bhogeswara Rao & Rigaud, 1974, 1975). Faint reflections of rutile first appear in the sample annealed at 700 °C. After heating at 800 °C these reflections become more intense and a shoulder after the (104)I reflection starts to grow due to the presence of hematite. At 900 °C, additional

Table 4.2: Oxidation rates of the ilmenite single crystal heated at different temperatures and for different times.

	Δm [%] 1h	Δm [%] 12h	Δm [%] 100h	R_{ox} [%] 1h	R_{ox} [%] 12h	R_{ox} [%] 100h
700°C	n/a	n/a	0.56	n/a	n/a	11.2
800°C	0.29	0.79	1.34	5.6	15.8	26.8
900°C	0.42	1.04	2.17	8.4	20.8	43.4
1000°C	n/a	2.70	n/a	n/a	51.14	n/a

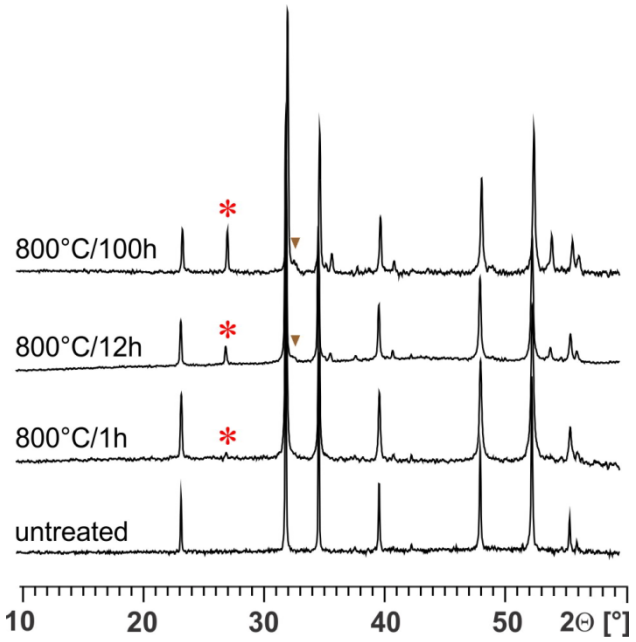


Figure 4.3: XRD diagrams of untreated ilmenite and samples heated at 800 °C for 1, 12 and 100 hours Main reflections belong to Mn-ilmenite, and rutile (red asterisk) and hematite (triangle) are minor phases.

reflections start to emerge, as the oxidation reaction begins to follow the Eq. (1.5). With a decrease of Mn-ilmenite reflections, rutile reflections start to gain in intensity. In addition, reflections of the high temperature pseudobrookite (Fe_2TiO_5) phase are observed. At 1000 °C ilmenite is still present, but the main phase is pseudobrookite.

Figure 4.3 presents the powder X-ray diffractogram of the samples heated at 800 °C for different periods of time. At 800 °C transformation of ilmenite starts after annealing for 1h when a weak reflection of rutile is observed, same as in the sample heated at 700 °C for 12 hours. With the increase of heating time, recrystallization of ilmenite is enhanced and the percentage of rutile in the sample increases. No phases other than rutile and hematite formed even after heating for 100h.

The oxidation rate (R_{ox}) increases with the annealing time and temperature. Even at 1000 °C after heating for 100h the sample only oxidized 51.14 %. This suggests that oxidation kinetic of the single-crystal samples is slow, as it is mainly limited by bulk (crystal) diffusion of cations.

4.3 Microstructure Characterization of Heated Ilmenite Along $[001]_I$

SEM images of $[001]_I$ cross-sections of the samples heat-treated for 12 hours in the temperature range of 600–1000 °C are shown in Figure 4.4. The sample fired at 600 °C (Figure 4.4a) shows no evident transformation, only Mn-ilmenite, which is consistent with XRPD data recorded on this sample (Figure 4.2). At 700 °C (Figure 4.4b) about 1 µm thick Fe-rich layer (Fe_2O_3) appears on the surface of the sample and is accompanied by a 20-25 µm deep recrystallization zone, characterized by thin rutile lamellae, intersecting at 60°. This clearly indicates that at this temperature, the onset of the oxidation process might be driven by out-diffusion of Fe^{2+} ions from ilmenite crystal and its surface oxidation to Fe_2O_3. As a result, rutile lamellae form in the Fe-depleted ilmenite. At 800 °C (Figure 4.4c) both the hematite layer becomes thicker and the recrystallization zone extends deeper into the crystal, indicating faster oxidation kinetics. Along with the sagenitic rutile in the recrystallization zone cracks start to appear. The cracks broaden from the interior towards the surface of the crystal, forming numerous side branches. Quantitative SEM/EDS analyses of the matrix phase between the rutile lamellae revealed that its composition is similar to that of the starting ilmenite. In addition, the composition of the surface oxide layer reveals that it contains the corresponding amounts of fine-grained hematite (Fe_2O_3) and bixbyite (Mn_2O_3), indicating that Fe^{2+} and Mn^{+} diffuse out of the parent Mn-ilmenite during oxidation. The presence of bixbyite is in accordance with the study of Grant et al. (1968) who reported that bixbyite is the most stable low-temperature Mn-oxide phase when Fe^{3+} ions are available in abundance. The 900 °C sample (Figure 4.4d) is completely recrystallized; sagenitic rutile extends throughout the original ilmenite crystal. Here rutile starts to react with the ilmenite matrix to form pseudobrookite. At 1000 °C (Figure 4.4e) the parent ilmenite reacts with the rutile to form pseudobrookite and rutile with irregular shape.

In the course of the high temperature oxidation of ilmenite, rutile changes its morphology. During the exsolution of rutile from the parent Mn-ilmenite, rutile is formed through the rearrangement of Ti cations in the common oxygen sublattice resulting in their growth in three directions intersecting at 60° (Figure 4.5a). However, with the prolonged heating rutiles are forming grains with irregular shape. The structures of pseudobrookite on one hand, and rutile and ilmenite on the other hand have no common structural features and therefore the transformation is not topotaxial and no oriented intergrowths are observed (Figure 4.5 b).

A close-up of rutile exsolutions in parent ilmenite viewed in basal orientation (Figure 4.5a) suggests a simple orientation relationship OR-1, where the c-axes of exsolved rutile domains intersect at 60° (Armbruster, 1981; Force, et al., 1996). To determine a precise orientation relationship between rutile and hosting Mn-ilmenite, the 800 °C/12h sample was further studied by TEM. The TEM sample was prepared with the recrystallization front placed in the centre of the sample (Figure 4.6a). Figure 4.6b is a low-magnification bright-field TEM image of coinciding rutile lamellae viewed in $[001]_I$ projection of ilmenite. Apparently, rutile is exsolved in three directions within the Mn-ilmenite matrix. In this sample, the average width of rutile lamellae ranges from 50–250 nm. The angles measured between individual rutile lamellae roughly correspond to 60°. Electron diffraction pattern (Figure 4.6c) recorded across the selected rutile/Mn-ilmenite area, shown in Figure 4.6b, shows that Mn-ilmenite is oriented in $[001]_I$ projection, while the rutile domains are in $[010]_R$ projection, and $(3\bar{3}0)_I$ plane of ilmenite coincides with $(002)_R$ plane of rutile, or alternatively, $(110)_I$ is parallel to $(200)_R$. Converting planes into directions, the orientation relationship exactly corresponds to OR- 1:

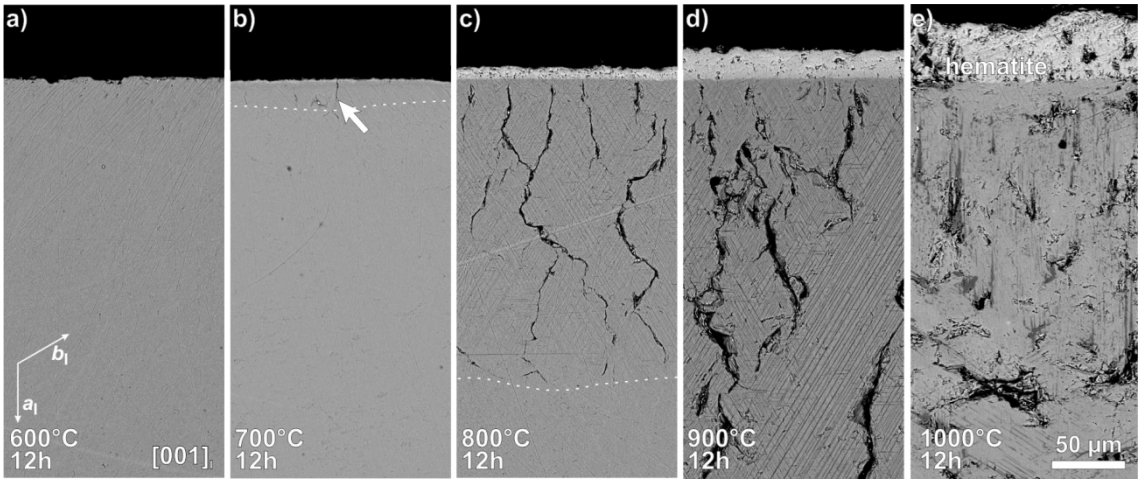


Figure 4.4: SEM/BSE images of samples heat-treated at different temperatures (600-1000 °C) for 12 hours a) At 600 °C sample is homogeneous without oxidation products. b) At 700 °C thin oxide layer is formed at the surface of the sample with recrystallization front (indicated by dashed line) extending from the surface into the interior of the sample. c) At 800 °C thickness of the surface layer and recrystallization front increases, and the cracks start to appear. d) At 900 °C the sample is completely recrystallized. e) At 1000 °C the rutile is starting to react with parent ilmenite and forms irregular grains.

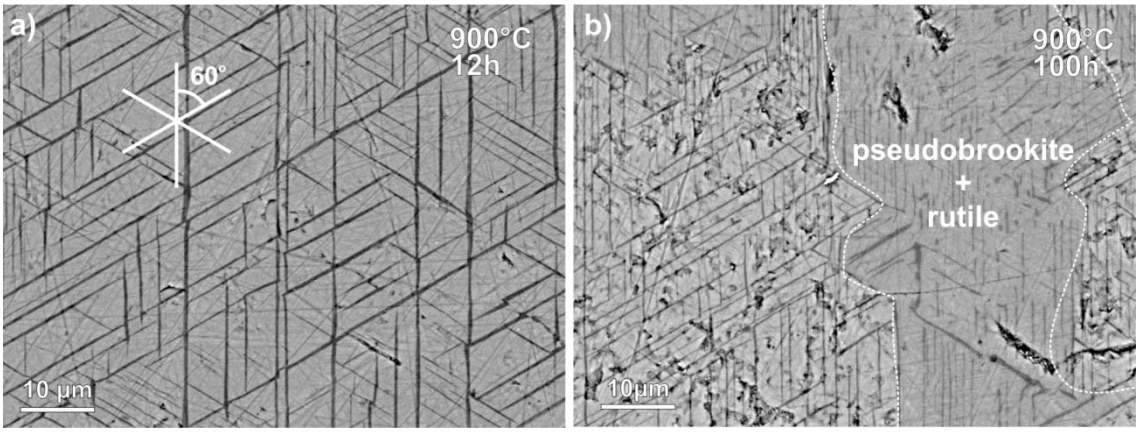


Figure 4.5: SEM/BSE image of rutile lamellae in ilmenite and pseudobrookite a) In the sample heated at 900 °C for 12h, rutile lamellae are extended in three directions intersecting at 60°. b) With the reaction of ilmenite and rutile the rutile is transformed to grains of irregular shape in the pseudobrookite matrix. However, rutile lamellae in ilmenite still have three main directions.

$<001>_R$ $\{010\}_R$ || $<210>_I$ $\{001\}_I$, with rutile–ilmenite interface $(200)_R$ | $(110)_I$. It appears that the rutile's c-axis runs parallel to the elongation of the rutile lamellae, which coincides with the most rapid diffusion pathway reported for rutile (Sasaki, et al., 1985).

While in the mid of the recrystallization zone rutile has a well-defined structure, a transitional rutile-type phase is observed at the recrystallization front, where ilmenite crystal is being transformed into the rutile. Here, some rutile lamellae exhibit an extra

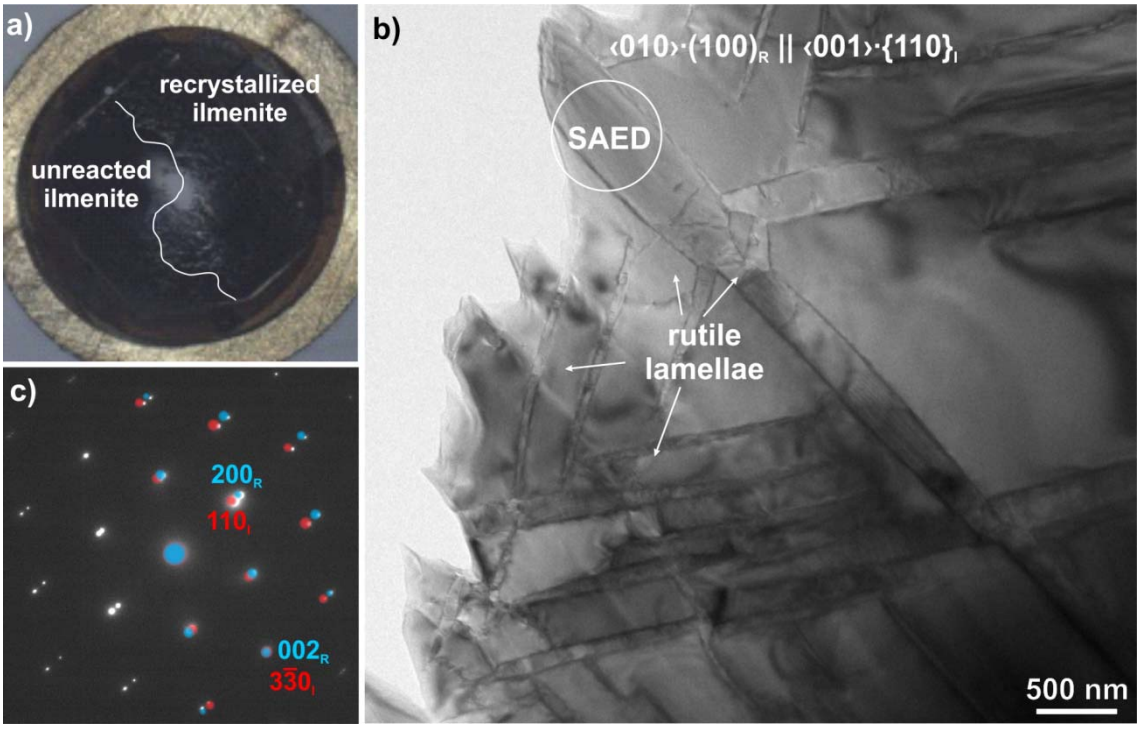


Figure 4.6: Low-magnification TEM analyses of rutile lamellae in the 800 °C/12h sample observed in $[001]_I$ a) TEM sample with the beginning of the recrystallization front in the electron transparent part. b) Bright-field TEM image of rutile lamellae in Mn-ilmenite matrix. c) Electron diffraction pattern of Mn-ilmenite and rutile from area indicated in TEM image. Indexing shows that rutile and ilmenite are met in OR-1.

superperiodicity, characteristic for modulated structures. Figure 4.7a shows a HRTEM image of such transition zone between ilmenite and rutile. While the upper part of rutile domain shows a regular pattern for the rutile structure in $[010]_R$ projection, the lower part shows superperiodic pattern along one set of lattice planes. The boundary between these two domains is diffuse, showing smooth transition from one pattern to another. Fourier transforms from superperiodic (Figure 4.7b) rutile indicate triple periodicity along a set of $(101)_R$ diffraction spots. Similar tripling in this direction was reported by Putnis (1978) and Rečnik et al. (2015) for Fe-rich rutile, where the authors assigned this modulation to the so-called Guinier-Preston (GP) zones. The superperiodicity is also typical for defect rutile structures with long range ordering, the so-called Magnéli phases (Bursill & Hyde, 1972). Magnéli phases are a reduced form of titanium-oxide and for determination of local oxidation state of titanium I preformed the EELS analyses. The oxidation states were determined based on the absolute energy shift of ionization edges in ELNES and the white-line intensity ratio between L_3/L_2 (Paterson & Krivanek, 1990). The EELS spectrums were recorded on lamella with superperiodic structure, rutile lamella and on ilmenite matrix for comparison (Figure 4.8a). The Ti-L_{23} ELNES spectra of transitional zone showed characteristic four white lines for Magnéli phases (Stoyanov, et al., 2007). In the case of rutile additional pre-peak exist (a'') and the second white line of the L_3 edge is split into b and b' peaks. On the other hand, Ti_4O_7 and Ti_5O_9 show a splitting of the first of the L_3 edge into peaks a and a'. Also the shift of the L_{32} edge to lower energies is observed with increase in oxidation state (Stoyanov, et al., 2007). Our measurements show that the energy positions of the Ti L_{32} peaks of the transitional zone

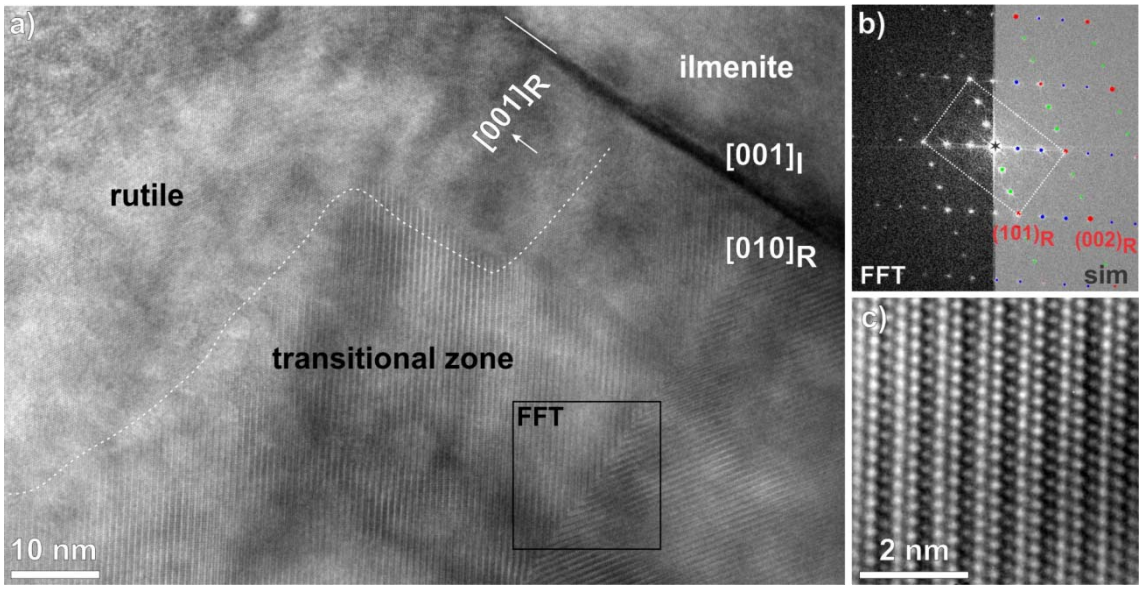


Figure 4.7: Transitional rutile-type phase at the recrystallization front observed in the sample 800 °C/12h a) HRTEM of the recrystallization front with rutile lamella showing the transitional zone with evident superperiodicity b) FFT of transitional zone showing tripling of $(101)_R$ reflection spots c) Enlarged part of the transitional zone showing tripled periodicity along $(101)_R$.

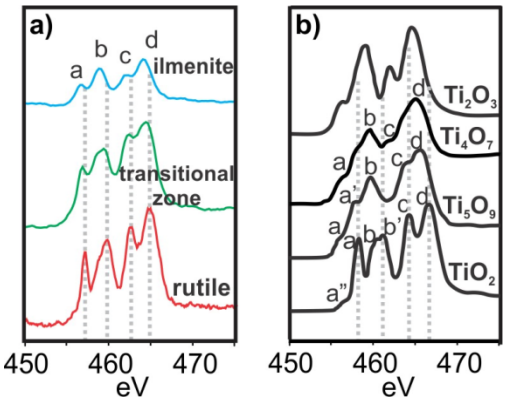


Figure 4.8: EELS analyses of Ti-L_{32} edge in ilmenite, transitional zone and rutile. a) Experimental EELS spectra of Ti L_{23} edge recorded on ilmenite, transitional zone and in rutile. b) Ti-L_{32} EELS spectra of various Ti-oxides taken from Stoyanov, et al., 2007.

are in-between those of the end-member Ti_2O_3 and TiO_2. Because of the similarity of the positions and intensity of Ti-L_{23} edge for all the phases with mixed titanium state, the most probable one is Ti_5O_9 since it has the highest ratio of Ti^{4+}/ Ti^{3+}.

4.4 Characterization of Surface Layer

Surfaces of the samples heated at 700-1000 °C for 12 hours are presented in Figure 4.9. The formation of the surface layer begins at 700 °C by reaction of Fe^{3+} with oxygen and formation of hematite platelets (Figure 4.9a). However, at this stage of transformation the surface is still not completely covered with newly formed oxide as it is shown in inset of Figure 4.9a. At 800 °C for 12 hours a mixed hematite and bixbyite starts to form as polycrystalline layer with the grain size up to a few 100 nm. The nano-size of hematite grains explains why the hematite is only visible as a very broad shoulder on the XRD patterns (Figure 4.2.). At this stage hematite-bixbyite layer is still porous enabling further diffusion of Fe and Mn cations (Figure 4.9b). At 900 °C the grain size increases and isolated tabular crystals up to a few µm appear on the surface (Figure 4.9c). With the increased thickness of the surface oxide layer and with closing of the pores, the diffusion paths are closing. At 1000 °C, the thick surface layer is composed of nicely developed crystals (Figure 4.9d), which completely close the diffusion paths, resulting in the recrystallization of ilmenite and rutile, in the interior of the crystal, to pseudobrookite.

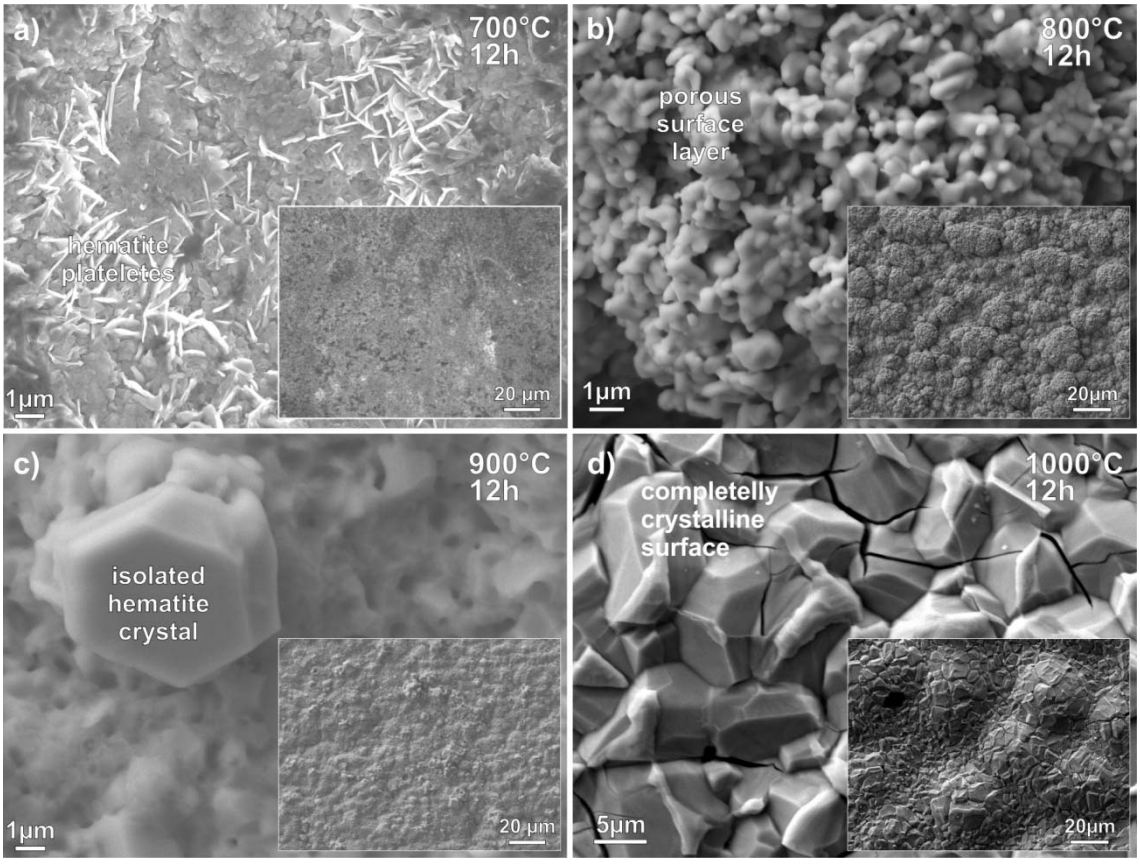


Figure 4.9: SEM images of surface oxide layer of samples heated for 12 hours at temperatures from 700 to 1000 °C. At 700 °C the surface layer starts to form as platelets and the ilmenite surface are not completely covered; b) At 800 °C surface oxide layer is polycrystalline with the grain size ~ 100 nm c) At 900 °C µm-sized hematite crystals are forming at the surface and slowly close the diffusion paths; d) At 1000 °C the surface is covered with well-developed hematite crystals.

4.5 Microstructure Characterization of Heated Ilmenite Along $[110]_I$

Further information on exsolution mechanism was obtained in prism orientation of the sample. Figure 4.10 shows the 800 °C/100h sample in $[1\bar{1}0]_I$ projection. Here, the exsolution texture appears very different compared to that in basal projection. In $[1\bar{1}0]_I$ projection the c-axis of parent Mn-ilmenite is pointing upwards. SEM image in Figure 4.10a shows that rutile exsolution lamellae are lined parallel to the $[110]_I$ prism surface of ilmenite. Vertical orientation of the exsolution lamellae indicates that they chose the direction of fast cation diffusion reported for oxides with the corundum-type structure (Sabioni, et al., 2005). The length of individual rutile columns well exceeds 100 µm, while their widths are generally below 250 nm. A close-up into the fine texture of exsolution lamellae shows that rutile columns are interrupted by perpendicular nano-sized nodes extending across the width of the column (Figure 4.10b). This interesting feature was further analysed by TEM. Rutile columns have an unusual bamboo-like appearance where the rutile lamella is randomly interrupted by joint-like nodes (Figure 4.10c). The main feature of bamboo-like rutile columns are the concave rutile sections with respect to hosting ilmenite and the nodes are thicker and have a convex shape. Chemical composition (EDS) of these nodes indicates that they consist of ilmenite, with a slightly altered Fe/Mn ratio compared to that of the parent ilmenite. While the composition of the parent ilmenite is $Fe_{0.60}Mn_{0.40}TiO_3$ (TEM/EDS analysis), the composition of the ilmenite within the rutile nodes corresponds to $Fe_{0.67}Mn_{0.33}TiO_3$ (see Table 4.3). Interestingly, the Fe/Mn ratio in the rutile lamella is comparable to the ilmenite in the node sections of the lamella. Figure 4.10d shows a typical joint section at higher magnification. At first glance a complex situation carries valuable information on the dynamics of diffusion controlled exsolution processes. In addition to a different chemical composition, ilmenite in rutile nodes has a different orientation than the parent ilmenite indicating its different origin. While the c-axis in parent ilmenite is pointing upwards, the one in the nodes points sideways. Both compositional and structural features strongly indicate a different origin of nodular ilmenite, which will be termed as ilmenite'. FFT transform of the ilmenite–rutile–ilmenite' section (Figure 4.10e) clearly shows that the ilmenite domains are rotated by 90° with respect to each other. Similar Fe/Mn ratio to to the that measured in rutile lamellae and its perpendicular orientation suggest that ilmenite' exsolved from rutile on cooling, rather than from parent ilmenite. Another evidence of this process is the concave shape of rutile sections which indicate reverse exsolution of ilmenite that resulted in a volume reduction of rutile.

Table 4.3: TEM/EDS analyses of composition in parent ilmenite, rutile and secondary ilmenite'.

	Ti (at%)	Fe (at%)C	Mn (at%)	Fe/Mn
Ilmenite	52.2±2.7	30.3±2.6	19.5±2.1	3:2
Rutile	95.5±0.8	3.1±0.5	1.5±0.4	2:1
Ilmenite'	48.2±2.4	34.6±3.0	17.2±1.6	2:1

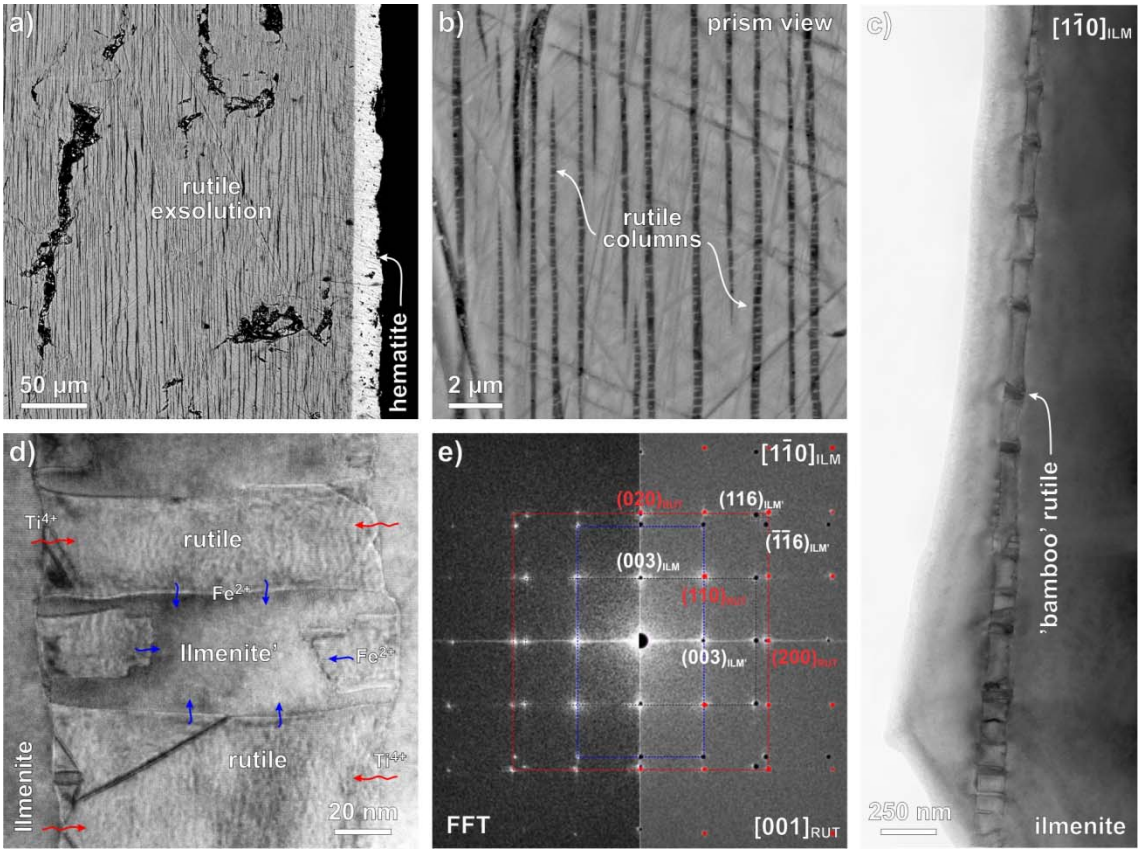


Figure 4.10: Rutile lamellae in the 800 °C/100h sample viewed along $[1\bar{1}0]_I$. a) SEM/BSE of recrystallized ilmenite with ~25 µm thick surface layer and rutile lamellae lined along the c-axis of parent ilmenite. b) Close-up of rutile lamellae showing light-grey notches interrupting the vertical rutile columns. c) Bright-field TEM image of a single rutile column showing bamboo-like morphology. d) Close-up of an ilmenite node of rutile column. e) FFT of the ilmenite-rutile-ilmenite' section showing that the c-axes of parent ilmenite and ilmenite' in node section of rutile are rotated by 90° with respect to each other.

4.6 Mechanism of Topotaxial Transformation of Heated Ilmenite

The ilmenite oxidation is a typical example of topotaxial recrystallization, where the original single crystal is transformed into structurally related phases along the crystallographically best matching directions (Dent Glasser, et al., 1962). In this part of the thesis I have shown that oxidation of ilmenite is a structurally controlled topotaxial reaction where rutile TiO_2 is exsolved from the parent Mn-ilmenite phase following previously described OR-1: $<001>_R \{010\}_R \parallel <210>_I \{001\}_I$ (Armbruster, 1981; Rečnik, et al., 2015). This complex structural transformation is driven by surface oxidation and lattice diffusion. The only species that can be oxidized in the system are the Fe^{2+} and Mn^{2+} ions, while Ti^{4+} ions are already in their fully oxidized state. This triggers a constant diffusion of divalent cations to the crystal surface, where they are oxidized into their trivalent state and form polycrystalline (Fe, Mn)-oxide layer, which is

consistent with the previous studies on fine crystalline ilmenite (Bhogeswara Rao & Rigaud, 1974; Fu, et al., 2010). In the beginning the hematite grows in the form of plates and only partially covers the surface of the sample, making the iron out-diffusion from ilmenite structure very fast. The morphology of products influences the kinetics of a gas-solid reaction where the plate's growth affects the kinetics in the early stages. It is usually assumed that the reaction product covers the surface of a solid in the form of a dense film and migration of ions through it becomes a rate determining process (Bhogeswara Rao & Rigaud, 1974). With prolonged heating and increase of temperature the hematite layer gets thicker making the surface oxidation slower, and the most important process of transformation becomes lattice diffusion. The surface layer is becoming richer in bixbyite, since the diffusivity of Mn increases with the temperature (Grant, et al., 1968).

No different than in fine crystalline ilmenite (Briggs & Sacco, 1993), oxidation of Fe^{2+} and Mn^{2+} begins on the surface of the crystal, while the reaction is driven by the chemical potential (Fu, et al., 2010; Zhang, et al., 2013). As a consequence, the host ilmenite becomes Mn and Fe-deficient, which triggers structural rearrangement and the formation of rutile lamellae within the so-called recrystallization zone. In this (Fe, Mn)-depleted Mn-ilmenite, Ti^{4+} ions start to rearrange into the closely related rutile structure within the ilmenite host. The oxygen sublattice serves as a diffusion path for Fe and Mn to diffuse out and for Ti to rearrange and form rutile lamellae. During the rearrangement of Ti a transition zone is formed in the recrystallization front in the samples, where I found a rutile with an unusual modulation. In rutile, such structures can form by crystallographic shear (CS) mechanisms (Reece & Morrell, 1991), or indicate the presence of transitional Guinier-Preston (GP) zones (Putnis, 1978). CS structures are more characteristic for non-stoichiometric rutile (reduced; Ti^{3+} present in the CS-planes), whereas GP zones have been reported for Fe-rich rutiles (Putnis, 1978; Rečnik, et al., 2015). Transitional zones were found only at the recrystallization front of rutile and it seems that the transition phase is short-living and rapidly recrystallizes to normal rutile structure by out-diffusion of the Fe ions.

The change of the structure from ilmenite to intermediate phase and finally rutile occurs through the crystallographic shear mechanism. In the *hcp* structure the slip plane is $(110)_I$ since it has the highest packing density (Partridge, 1967). The intermediate phase between corundum type structure and rutile was also observed on the boundary of corundum with rutile, suggesting that this is a typical transition phase from corundum to rutile type structure (Bursill & Blanchin, 1989). In heat-treated Mn-ilmenite samples the EELS analysis revealed that intermediate structure contains titanium-oxide in the form of crystallographic shear phase Ti_nO_{n-1}, most probably Ti_4O_7. Both phases have Ti in both Ti^{3+} and Ti^{4+} state. Since the transformation of ilmenite and lamellae growth occurs in the oxidizing atmosphere, it is more likely that the transition phase is Ti_5O_9 since it contains more Ti^{4+}. Also, the Ti_5O_9 structure is built from rutile slabs that are 5 $[TiO_6]$ octahedra which are connected through sharing faces. Across crystallographic shear plane the adjacent slabs are relatively displaced toward each other by the vector ½ $[011]_R$. The structure of CS plane also contains the corundum slab where double octahedra lay parallel to b-axis of Ti_5O_9. The corundum type slabs are remains of ilmenite structure in case of transition phase that is formed during oxidation of ilmenite (Andersson, 1960).

The fact that the intermediate phase contains the Ti cation in two oxidation states suggests that titanium is locally reduced during oxidation with the intervalence charge transfer (IVCT) (Chen, et al., 2013; Seda & Hearne, 2004). IVCT is an electron transfer from a low oxidation state cation to a neighbouring cation of higher oxidation state. In the case of ilmenite this transfer is presented as:

$$Fe^{2+} + Ti^{4+} \rightarrow Fe^{3+} + Ti^{3+} \tag{4.1}$$

The main question in these processes is how the divalent cations diffuse from the interior of the ilmenite crystal. Solid-state diffusion studies showed that the mobility of Fe along the c-axis of the hematite is several orders of magnitude faster than in prism directions (Sabioni, et al., 2005). This opens channels for rearrangement of the Ti^{4+} ions, forming topotaxial rutile exsolutions along the c-axis of parent ilmenite. It can be expected that the diffusion rates are similar in the Mn-ilmenite, which is isostructural with hematite. As soon as rutile is formed, this accelerates the out-diffusion of divalent cations, as their diffusion (Fe) along the c-axis of rutile is faster by several orders of magnitude compared to that in hematite (Rečnik, et al., 2015; Sabioni, et al., 2005; Sasaki, et al., 1985). This has been confirmed by our observations which indicate that c-axis of parent Mn-ilmenite serves as a main diffusion path for divalent cations; leaving a free space for rearrangement of Ti^{4+} ions to form rutile lamellae along this direction (see Figure 4.10). As soon as rutile lamellae are formed, they start to act as paths for fast diffusion of divalent cations to the crystal surface, where they are oxidized. As a consequence, rutile is heavily enriched with Mn and Fe (EDS analyses, Table 4.3). Upon cooling, the solid solubility of these cations is exceeded and therefore they are exsolved from rutile in form of ilmenite' in orientation perpendicular to matrix ilmenite. The observed difference between the Fe/Mn ratio in the primary ilmenite and ilmenite' is probably due to different diffusion rates of the two cations. Exsolution of Fe-deficient ilmenite' thus indicates faster out-diffusion of Mn^{2+} compared to Fe^{2+}, which is an interesting result. Because of the negative volume difference, the host ilmenite crystal starts to crack, which further boosts the transformation (see Figure 4.4), and in this way, the oxidation process progresses further into the single crystal.

The reverse exsolution of ilmenite' is indicative of intense cation diffusion dynamics through rutile. Figure 4.11 shows a HRTEM image of ilmenite–rutile–ilmenite' section with proposed model of structurally controlled exsolution processes that lead to the formation of bamboo-like rutile exsolution lamellae. The sequence of exsolution can be deduced based on structural coherency across the ilmenite–rutile and rutile–ilmenite' interfaces. *hcp* stacking of the parent ilmenite is easily translated into the a-plane of rutile through reordering of Ti^{4+} ions in the common oxygen sublattice. Formation of rutile structure involves minor tetragonal distortion that produces a *hcp*-like stacking also in the perpendicular, b-plane of rutile. During the heat treatment rutile structure serves as the easy transport pathway for out-diffusion of cations (Fe^{2+} and Mn^{2+}) that are leaving the structure. During annealing the rutile is thus 'saturated' by Fe^{2+} and Mn^{2+}. However, when the temperature drops, rutile throws out the excess cations down to a given limit when they are 'frozen' in the structure. Exsolution of Fe^{2+} and Mn^{2+} can take place only within the rutile, which now becomes the parent structure in this secondary topotaxial process. Rutile and precipitated ilmenite' form another low-energy interface with b-plane of rutile parallel to hcp sequence of ilmenite'. This interface is structurally identical to the primary ilmenite–rutile interface, but translated by 90° through rutile structure (see Figure 4.11b). The resulting ilmenite–ilmenite' $(110)_I \mid (003)_{I'}$ interface is fully incoherent and reflects the exsolution sequence.

I have shown that oxidation of ilmenite in air is a topotaxial transformation caused by surface oxidation of divalent cations from the ilmenite structure. This triggers progressive recrystallization from the surface towards the interior of the crystal, according to the following mechanism:

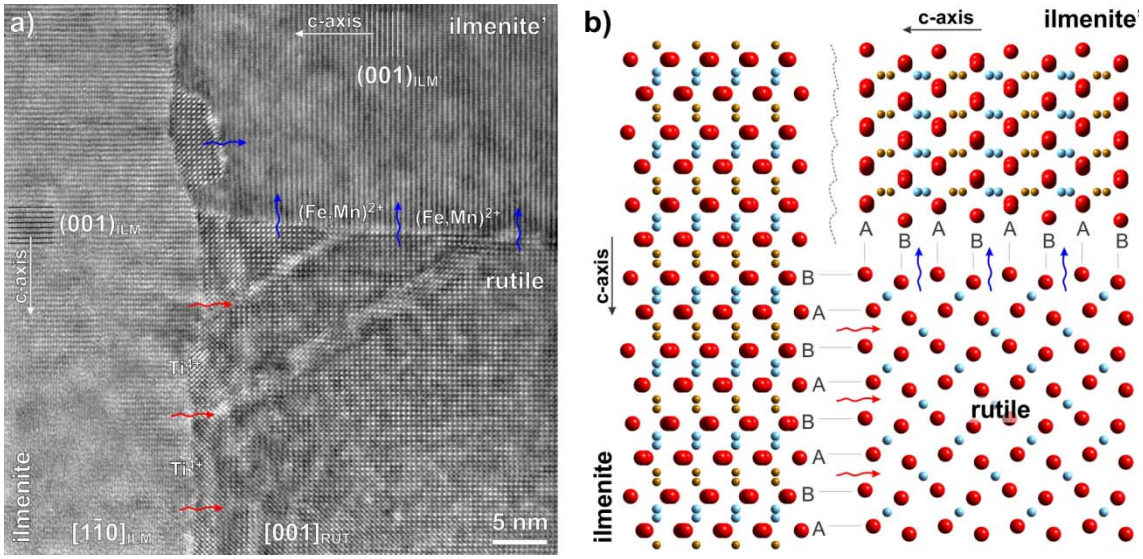


Figure 4.11: The mechanism of exsolution processes during oxidation of ilmenite under 800 °C. a) HRTEM image showing parent ilmenite, exsolved rutile and secondary ilmenite. b) Structural relations between the exsolved phases. First, rutile is exsolved from parent ilmenite forming a coherent $(110)_I$ $|(100)_R$ interface. On cooling, Fe^{2+} and Mn^{2+} cations that diffused through rutile are exsolved and form ilmenite' with secondary coherent $(010)_R|(110)_{I'}$ interface.

(1) Surface oxidation generates out-diffusion of divalent cations (Mn and Fe) and formation of polycrystalline hematite/bixbyite layer at the crystal surface. However, the question is how the oxidation starts at the surface, or how the Fe and Mn are oxidized from divalent to trivalent cations. The electron transfer is happening between oxygen from the surrounding atmosphere and divalent cation from the ilmenite structure. With the temperature increase the activation energy for electron release is achieved and the oxidation-reduction processes are occuring at the surface, when oxygen molecules from the atmosphere form oxide surface layer with trivalent cations oxidized in ilmenite structure.

(2) Depletion in Mn and Fe in the interior of the ilmenite crystal leads to structurally controlled exsolution of rutile lamellae, following a simple crystallographic relationship $<001>_R \{010\}_R \parallel <210>_I \{001\}_I$, producing networks of sagenitic rutile within the parent ilmenite. The open question is how the electroneutrality is preserved during the diffusion processes. The most probable point defects in ilmenite structure are iron and oxygen vacancies. With the addition of oxygen ions from atmosphere, to the crystal leads to formation of new structural unit and metal vacancies (Fe^{2+} and Mn^{2+} vacancies) (Andreozzi, et al., 1996; Atkinson & Taylor, 1985). When the iron and manganese form oxide surface layer, they are no longer part of ilmenite structure, titanium diffuses to the iron sites, leading to formation of Ti vacancies. At this point, electroneutrality can be reached by the formation of oxygen vacancies.

(3) Formation of rutile lamellae further boosts out-diffusion of divalent cations (Mn and Fe) along the c-axis of the rutile structure and further accelerates the oxidation process.

(4) Volume difference between the starting ilmenite and the exsolved rutile causes cracking of the parent ilmenite crystal, opening further paths for oxidation.

The described recrystallization mechanism studied on the scale of a single ilmenite crystal helps to understand the oxidation processes in fine crystalline ilmenite, where the diffusion paths are much shorter and thus ilmenite-to-rutile transformation is incomparably faster.

Chapter 5

Conclusions

Rutile forms intergrowths with the corundum type structure (hematite/ilmenite) and during topotaxial reaction they form two main orientation relationships which were the main focus of the thesis. In the case of the samples from Mwinilunga, Zambia, rutile and hematite are intergrown with the crystallographic OR-2. On the other hand, heat treated ilmenite samples from Zagi Mountain Pakistan showed the OR-1. This gave me the possibility to study the formation of two different orientation relationships and to observe the conditions that lead to these relationships. In the end concluded the mechanism of formation of both samples and how the different orientation relationships are formed.

The oxidation of ilmenite is a replacement reaction that results in the formation of topotaxial rutile and hematite. The transformation is governed by the diffusion of cations through the common *hcp* oxygen sublattice resulting in the formation of specific crystallographic orientation relationships. I studied crystallographic and structural relations between exsoluted rutile in hematite or ilmenite matrix down to the atomic level in order to reconstruct the mechanism of their formation. The type of orientation relationship is a function of temperature and oxygen fugacity f_{O_2}.

I have shown that the rutile/hematite intergrowths from Mwinilunga, Zambia, originate from hemo-ilmenite crystals with a general formula of $(Fe_x^{2+}, Fe_{2-2x}^{3+})Ti_x^{4+}O_3$ where x=0.67 and formula of the solid solution is $Ilm_{0.67}Hem_{0.33}$. The parent crystal was formed at temperatures of 1050-1150 °C and low oxygen fugacities that were insufficient for oxidation of iron in ilmenite-rich solid solution. When the temperature dropped under 900 °C and $f_{O_2}$is ~10-11 bar the solid solution unmixed to ilmenite and hematite. With further decrease of temperature Fe^{2+} oxidized to Fe^{3+}. Discharged electron reduces the oxygen from the surrounding atmosphere, leading to the formation of surface oxide layer. The diffusion of Fe along the c-axis of hematite is several orders of magnitude faster than in prism directions. With the out-diffusion of Fe, the pillar-like rutile structures are formed along the c-axis of hosting hematite. Since the Ti preferred diffusion direction is in basal plane of hematite, pillars grow perpendicular to c-axis of parent crystal after nucleation. Based on the observed interfaces the temperature of rutile nucleation is ~740 °C. When the temperature further decreases below 600 °C the excess iron from rutile is exsolved in form on nm-size hematite lamellae. The final stage of the transformation is growth of larger rutile crystals on the surface characteristic for the pneumatolytic stage of crystallization. The large rutile crystals follow the orientation of rutile domains from the interior of the intergrowths formed at previous stage of replacement reaction.

Oxidation of single Mn-ilmenite crystal from Zagi Mountain, Pakistan, also showed that transformation of ilmenite to rutile and hematite is a topotaxial replacement reaction caused by progressive transformation from the surface towards the interior of

the crystal. The first step in this replacement reaction is oxidation of divalent Fe^{2+} and Mn^{2+} cations to trivalent state on the surface of the single crystal. This leads to a depletion of parent Mn-ilmenite in Mn and Fe which triggers the diffusion of Ti atoms within the oxygen sublattice and initiates the formation of rutile lamellae. The formation of rutile goes through transitional Magnéli phase. With the formation of rutile lamellae also new diffusion paths are open for the accelerated out-diffusion of divalent Fe^{2+} and Mn^{2+} cations. As a result some of the Fe and Mn cations are trapped in rutile at higher temperatures and they exsolute in the form of nodular ilmenite precipitates in rutile lamellae on cooling of the sample.

Although in both instances the mechanism of transformation is triggered by out-diffusion of Fe, the final orientation relationship depends on the temperature and oxygen fugacity. In the intergrowth of rutile and hematite from Mwinilunga in Zambia, the observed orientation relationship is:

$$\text{OR-3: } \langle 010 \rangle_{\text{R}} \{401\}_{\text{R}} \,||\, \langle 001 \rangle_{\text{H}} \{170\}_{\text{H}}$$

This orientation relationship leads to a formation of four main rutile-rutile relations: symmetry-related configuration, $\{101\}_{\text{R}}$ and $\{301\}_{\text{R}}$ twins and low-angle tilt boundaries.

The heat-treated single Mn-ilmenite crystal from Mt Zagi in Pakistan, because of the readily available oxygen, diffusion of cations through the *hcp* oxygen sublattice is very fast leading to the orientation relationship:

$$\text{OR-1: } <001>\{010\}_{\text{R}} \,||\, <210>_{\text{I}} \{001\}_{\text{I}}$$

In the OR-1, fast diffusion of cations leads to the formation of only non-crystallographic configuration of rutile domains.

The topotaxial transformation of ilmenite to rutile and hematite is triggered by oxidation of Fe^{2+} in ilmenite to Fe^{3+} at the surface that triggers exsolution of Ti ions within the parent ilmenite oxygen sublattice to form rutile lamellae. The diffusion of iron is controlled by the activity of oxygen. When the oxygen is readily available for the oxidation of Fe^{2+} to Fe^{3+}, diffusion is fast; on the other hand if activity of oxygen is low, the oxidation of iron is slow. The kinetics of diffusion controls the orientation relationship: the OR-1 is formed when the diffusion is fast since the Ti cations completely inherit the ilmenite oxygen sublattice, while the OR-3 is a result of slow iron diffusion when Ti cations have enough time to adopt energetically most favourable positions.

References

Amami, B., Addou, M., Millot, F., Sabioni, A., & Monty, C. (1999). Self-diffusion in α-Fe_2O_3 natural single crystals. *Ionics, 5*(5-6), 358-370.

Andersson, S. (1960). The crystal structure of Ti_5O_9. *Acta chemica scandivica, 14*, 1161-1172.

Andreozzi, G. B., Cellucci, F., & Gozzi, D. (1996). High-temperature electrical conductivity of $FeTiO_3$ and ilmenite. *Journal of Materials Chemistry, 6*(6), 987-991.

Ariskin, A. A., & Barmina, G. S. (1999). An empirical model for the calculation of spinel-melt equilibria in mafic igneous systems at atmospheric pressure: 2. Fe-Ti oxides. *Contributions to Mineralogy and Petrology, 134*(2-3), 251-263.

Armbruster, T. (1981). On the origin of sagenites: structural coherency of rutile with hematite and spinel structures types. *Neues Jahrbuch für Mineralogy, 7*, 328-334.

Atkinson, A., & Taylor, R. I. (1985). Diffusion of ^{55}Fe in Fe_2O_3 single crystals. *Journal of Physics and Chemistry of Solids, 46*(4), 469-475.

Baker, D. R., & Buddington, A. F. (1970). Geology and magnetite deposits of the Franklin quadrangle and part of the Hamburg quadrangle, New Jersey *USGS Numbered Series* (Vol. 638). Washington: United States Government printing office.

Bateman, A. M. (1951). The formation of late magmatic oxide ores. *Economic Geology, 46*(4), 404-426. doi: 10.2113/gsecongeo.46.4.404

Bernal, J. D. (1960). On topotaxy. *Schweizer archiv*, 69-75.

Bernal, J. D., Dasgupta, D. R., & Mackay, A. L. (1957). Oriented transformations in iron oxides and hydroxides. *Nature, 180*(4587), 645-647.

Bernal, J. D., & Mackay, A. L. (1965). Topotaxy. *Tschermaks mineralogische und petrographische Mitteilungen, 10*(1-4), 331-340.

Bhogeswara Rao, D., & Rigaud, M. (1974). Oxidation of ilmenite and the product morphology. *High Temperature Science 6*, 323-341.

Bhogeswara Rao, D., & Rigaud, M. (1975). Kinetics of the oxidation of ilmenite. *Oxidation of Metals, 9*(1), 99-116.

Blake, R. L., Hessevick, R. E., Zoltai, T., & Finger, L. W. (1966). Refinement of the hematite structure. *American Mineralogist, 51*, 123-129.

Bosi, F., Hålenius, U., & Skogby, H. (2009). Crystal chemistry of the magnetite-ulvöspinel series. *American Mineralogist, 94*(1), 181-189. doi: 10.2138/am.2009.3002

Bowles, J. F. W., Howie, R. A., Vaughan, D. J., & Zussman, J. (2011). *Non-silicates: oxides, Hydroxides and sulphides* (2nd edition ed. Vol. 5A): The Geological Society.

Briggs, R., & Sacco, A. (1993). The oxidation of llmenite and its relationship to the FeO-Fe_2O_3-TiO_2 phase diagram at 1073 and 1140 K. *Metallurgical Transactions A, 24*(6), 1257-1264.

Brownlee, S. J., Feinberg, J. M., Harrison, R. J., Kasama, T., Scott, G. R., & Renne, P. R. (2010). Thermal modification of hematite-ilmenite intergrowths in the Ecstall pluton, British Columbia, Canada. *American Mineralogist, 95*(1), 153-160. doi: 10.2138/am.2010.3191

Buddington, A. F., & Lindsley, D. H. (1964). Iron-titanium oxide minerals and synthetic equivalents. *Journal of Petrology, 5*(2), 310-357. doi: 10.1093/petrology/5.2.310

Bursill, L. A., & Blanchin, M. G. (1989). Interphase structures observed as alumina precipitates in rutile. *Philosophical Magazine A, 60*(5), 631-642.

Burton, B. P. (1985). Theoretical analysis of chemical and magnetic ordering in the system Fe_2O_3 -$FeTiO_3$. *American Mineralogist, 70*(9-10), 1027-1035.

Burton, B. P. (1991). The interplay of chemical and magnetic ordering. *Reviews in Mineralogy and Geochemistry, 25*(1), 303-322.

Carmichael, C. M. (1961). The magnetic properties of ilmenite-haematite crystals. *Proceedings of the Royal Society of London. Series A. Mathematical and Physical Sciences, 263*(1315), 508-530. doi: 10.1098/rspa.1961.0177

Carmichael, I. S. E., & Nicholls, J. (1967). Iron-titanium oxides and oxygen fugacities in volcanic rocks. *Journal of Geophysical Research, 72*(18), 4665-4687.

Charlier, B., Namur, O., Malpas, S., de Marneffe, C., Duchesne, J.-C., Auwera, J. V., & Bolle, O. (2010). Origin of the giant Allard Lake ilmenite ore deposit (Canada) by fractional crystallization, multiple magma pulses and mixing. *Lithos, 117*(1–4), 119-134.

Charlier, B., Skår, Ø., Korneliussen, A., Duchesne, J.-C., & Vander Auwera, J. (2007). Ilmenite composition in the Tellnes Fe–Ti deposit, SW Norway: fractional crystallization, postcumulus evolution and ilmenite–zircon relation. *Contributions to Mineralogy and Petrology, 154*(2), 119-134.

Chen, S. W., Huang, M. J., Lin, P. A., Jeng, H. T., Lee, J. M., Haw, S. C., Chen, S. A., Lin, H. J., Lu, K. T., Chen, D. P., Dou, S. X., Wang, X. L., & Chen, J. M. (2013). Orbital structure of $FeTiO_3$ ilmenite investigated with polarization-dependent X-ray absorption spectroscopy and band structure calculations. *Applied Physics Letters, 102*(4), 042107. doi: doi:http://dx.doi.org/10.1063/1.4789992

Daneu, N., Rečnik, A., & Mader, W. (2014). Atomic structure and formation mechanism of (101) rutile twins from Diamantina (Brazil). *American Mineralogist, 99*, 612-624.

Daneu, N., Schmid, H., Rečnik, A., & Mader, W. (2007). Atomic structure and formation mechanism of (301) rutile twins from Diamantina (Brazil). *The American mineralogist, 92*, 11-12.

Dent Glasser, L. S., Glasser, F. P., & Taylor, H. F. W. (1962). Topotactic reactions in inorganic oxy-compounds. *Quarterly Reviews, Chemical Society, 16*(4), 343-360.

Eugster, H. P. (1957). Heterogeneous reactions involving oxidation and reduction at high pressures and temperatures. *The Journal of Chemical Physics, 26*(6), 1760-1761. doi: doi:http://dx.doi.org/10.1063/1.1743626

Fleet, M. (1981). The structure of magnetite. *Acta Crystallographica Section B, 37*(4), 917-920. doi: doi:10.1107/S0567740881004597

Force, E. R. (1980). The provenance of rutile. *Journal of Sedimentary Research, 50*(2), 485-488. doi: 10.1306/212f7a31-2b24-11d7-8648000102c1865d

Force, E. R., Richards, R. P., Scott, K. M., Valentine, P. C., & Fishman, N. S. (1996). Mineral intergrowths replaced by "elbow-twinned" rutile in altered rocks. *The Canadian Mineralogist, 34*(3), 605-614.

Frost, B. R. (1991). Introduction to oxygen fugacity and its petrologic importance. In D. H. Lindsley (Ed.), *Oxide Minerals: Petrologic and Magnetic Significance*. New York, USA: Stony Brook.

Fu, X., Wang, Y., & Wei, F. (2010). Phase transitions and reaction mechanism of ilmenite oxidation. *Metallurgical and Materials Transactions A, 41*(5), 1338-1348.

Ghiorso, M. S. (1990). Thermodynamic properties of hematite - ilmenite - geikielite solid solutions. *Contributions to Mineralogy and Petrology, 104*(6), 645-667.

Ghiorso, M. S., & Sack, O. (1991). Fe-Ti oxide geothermometry: thermodynamic formulation and the estimation of intensive variables in silicic magmas. *Contributions to Mineralogy and Petrology, 108*(4), 485-510.

Grant, R. W., Geller, S., Cape, J. A., & Espinosa, G. P. (1968). Magnetic and crystallographic transitions in the α–Mn_2O_3-Fe_2O_3 system. *Physical Review, 175*(2), 686-695.

Grey, I. E., & Reid, A. F. (1972). Shear structure compounds $(Cr,Fe)_2Ti_{n-2}O_{2n-1}$ derived from the α-PbO_2 structural type. *Journal of Solid State Chemistry, 4*(2), 186-194.

Guo, W. Q., Malus, S., Ryan, D. H., & Altounian, Z. (1999). Crystal structure and cation distributions in the $FeTi_2O_5$-Fe_2TiO_5 solid solution series. *Journal of Physics: Condensed Matter, 11*(33), 6337.

Gupta, S., Rajakumar, V., & Grieveson, P. (1991). Phase transformations during heating of ilmenite concentrates. *Metallurgical Transactions B, 22*(5), 711-716.

Hallström, S., Höglund, L., & Ågren, J. (2011). Modeling of iron diffusion in the iron oxides magnetite and hematite with variable stoichiometry. *Acta Materialia, 59*(1), 53-60.

Harrison, R. J., Redfern, S. A. T., & Smith, R. I. (2000). In-situ study of the $R\bar{3}$ to $R\bar{3}c$ phase transition in the ilmenite-hematite solid solution using time-of-flight neutron powder diffraction. *American Mineralogist, 85*(1), 194-205.

Hill, R., & Roedar, P. (1974). The crystallization of spinel from basaltic liquid as a function of oxygen fugacity. *The Journal of Geology, 82*(6), 709-729.

Howard, C. J., Sabine, T. M., & Dickson, F. (1991). Structural and thermal parameters for rutile and anatase. *Acta Crystallographica Section B, 47*(4), 462-468. doi: doi:10.1107/S010876819100335X

Hwang, S.-L., Shen, P., Yui, T.-F., & Chu, H.-T. (2010). On the coherency-controlled growth habit of precipitates in minerals. *Journal of Applied Crystallography, 43*(3), 417-428. doi: doi:10.1107/S0021889810007454

Hyde, B. G. (1976). Rutile: Planar Defects and Derived Structures. In H. R. Wenk (Ed.), *Electron Microscopy in Mineralogy* (pp. 310-318): Springer Berlin Heidelberg.

Ishikawa, Y. (1958). An order-disorder transformation phenomenon in the $FeTiO_3$–Fe_2O_3 solid solution series. *Journal of the Physical Society of Japan, 13*(8), 828-837.

Ishikawa, Y. (1962). Magnetic properties of ilmenite-hematite system at low temperature. *Journal of the Physical Society of Japan, 17*(12), 1835-1843.

Ishikawa, Y., & Syono, Y. (1963). Order-disorder transformation and reverse thermo-remanent magnetism in the $FeTiO_3$-Fe_2O_3 system. *Journal of Physics and Chemistry of Solids, 24*(4), 517-528.

Key, R. M., Liyungu, A. K., Njamu, F. M., Somwe, V., Banda, J., Mosley, P. N., & Armstrong, R. A. (2001). The western arm of the Lufilian Arc in NW Zambia and its potential for copper mineralization. *Journal of African Earth Sciences, 33*(3), 503-528.

Kidoh, K., Tanaka, K., Marumo, F., & Takei, H. (1984). Electron density distribution in ilmenite-type crystals. II. Manganese(II) titanium(IV) trioxide. *Acta Crystallographica Section B, 40*(4), 329-332. doi: doi:10.1107/S0108768184002238

Lee, W. E., & Lagerlof, K. P. D. (1985). Structural and electron diffraction data for sapphire (α -al2o3). *Journal of Electron Microscopy Technique, 2*(3), 247-258.

Lee, W. Y., Bristowe, P. D., Gao, Y., & Merkle, K. L. (1993). The atomic structure of twin boundaries in rutile. *Philosophical Magazine Letters, 68*(5), 309-314.

Lindsley, D. H. (1962). Investigation in the system FeO-Fe_2O_3-TiO_2 (Vol. 61): Carnegie Intitute Washington Yearbook.

Lindsley, D. H. (1963). Equlibrium relations of coexisting pairs of Fe-Ti oxides (Vol. 68): Carnegie Insitute Washington yearbook.

Lindsley, D. H. (1973). Delimitation of the eematite-ilmenite miscibility gap. *Geological Society of America Bulletin, 84*(2), 657-662. doi: 10.1130/0016-7606(1973)84<657:dothmg>2.0.co;2

Lindsley, D. H. (1976). The crystal chemistry and structure of oxide minerals as exemplified by the Fe-Ti oxides. In Douglas Rumble, III (Ed.), *Review in mineralogy: Oxide minerals* (Vol. 3).

Lindsley, D. H. (1991). Experimental studies of oxide minerals. In D. H. Lindsley (Ed.), *Oxide minerals: Petrologic and Magnetic Significance*. New York, USA: Stony Brook.

Löffler, L., & Mader, W. (2003). Transformation mechanism of the dehydration of diaspore. *Journal of the American Ceramic Society, 86*(4), 534-540.

Lotgering, F. K. (1959). Topotactical reactions with ferrimagnetic oxides having hexagonal crystal structures—I. *Journal of Inorganic and Nuclear Chemistry, 9*(2), 113-123.

Mackay, A. L. (1960). *Some aspects of the topochemistry of the iron oxides and hydroxides.* Paper presented at the Fourth international symposium on the reactivity of solids, Amsterdam.

McEnroe, S. A., & Brown, L. L. (2000). A closer look at remanence-dominated aeromagnetic anomalies: Rock magnetic properties and magnetic mineralogy of the Russell Belt microcline-sillimanite gneiss, northwest Adirondack Mountains, New York. *Journal of Geophysical Research: Solid Earth, 105*(B7), 16437-16456.

McEnroe, S. A., Harrison, R. J., Jackson, M. J., Hirt, A. M., Peter, R., Falko, L., Heidelbach, F., Takeshi, K., Andrew, P., Brown, L. L., & Ute, G.-S. (2005). Lamellar magnetism: effects of interface versus exchange interactions of nanoscale exsolutions in the ilmenite-hematite system. *Journal of Physics: Conference Series, 17*(1), 154.

McEnroe, S. A., Harrison, R. J., Robinson, P., & Langenhorst, F. (2002). Nanoscale haematite–ilmenite lamellae in massive ilmenite rock: an example of 'lamellar magnetism' with implications for planetary magnetic anomalies. *Geophysical Journal International, 151*(3), 890-912.

McEnroe, S. A., Robinson, P., Langenhorst, F., Frandsen, C., Terry, M. P., & Boffa Ballaran, T. (2007). Magnetization of exsolution intergrowths of hematite and ilmenite: Mineral chemistry, phase relations, and magnetic properties of hemo-ilmenite ores with micron- to nanometer-scale lamellae from Allard Lake, Quebec. *Journal of Geophysical Research: Solid Earth, 112*(B10), B10103.

Meinhold, G. (2010). Rutile and its applications in earth sciences. *Earth-Science Reviews, 102*(1–2), 1-28.

Morisset, C.-E., Scoates, J. S., Weis, D., Sauvé, M., & Stanaway, K. J. (2010). Rutile-bearing ilmenite deposits associated with the proterozoic Saint-Urbain and Lac Allard anorthosite massifs, Grenville Province, Quebec. *The Canadian Mineralogist, 48*(4), 821-849. doi: 10.3749/canmin.48.4.821

Murphy, P., & L.Frick. (2006). Titanium. In J.E. Kogel, N.C. Trivedi, J.M. Barker & S.T. Krukowski (Eds.), Industrial Minerals and Rocks - Commodities, Markets and Uses (pp. 987-1003): Society for Mining Metallurgy, and Exploration, Inc. Colorado.

Nakamura, A., Tochigi, E., Shibata, N., Yamamoto, T., & Ikuhara, Y. (2009). Structure and configuration of boundary dislocations on low angle tilt grain boundaries in alumina. *MATERIALS TRANSACTIONS, 50*(5), 1008-1014.

Nešković, N. B., Babić, B., & Konstantinović, J. (1977). High temperature anomalous behaviour of the crystal lattice of hematite. *Physica Status Solidi (a), 41*(2), K133-K136.

Nielsen, R., & Dungan, M. (1983). Low pressure mineral-melt equilibria in natural anhydrous mafic systems. *Contributions to Mineralogy and Petrology, 84*(4), 310-326.

Nord, G., & Lawson, C. (1989). Order-disorder transition-induced twin domains and magnetic properties in ilmenite-hematite. *American Mineralogist, 74*, 160-176.

Palache, C., Berman, H., & Frondel, C. (1952). Dana's System of Mineralogy. 7. Ed. *Geologiska Föreningen i Stockholm Förhandlingar, 74*(2), 218-219.

Partridge, P. G. (1967). The crystallography and deformation modes of hexagonal close-packed metals. *Metallurgical Reviews, 12*(1), 169-194. doi: doi:10.1179/mtlr.1967.12.1.169

Petersen, N. (1970). Calculation of diffusion coefficient and activation energy of titanium in titanomagnetite. *Physics of the Earth and Planetary Interiors, 2*(3), 175-178.

Porada, H., & Berhorst, V. (1998). Thrust tectonics in the domes region and copperbelt of Zambia: outline and outlook. *Freib Forschungsh, C475*, 145-162.

Putnis, A. (1978). The mechanism of exsolution of hematite from iron-bearing rutile. *Physics and Chemistry of Minerals, 3*(2), 183-197.

Putnis, A. (1995). *Introduction to mineral sciences*. Cambridge: Cambridge Univ. Press.

Ramdohr, P. (1979). *The ore minerals and their intergrowths*. Oxford ; New York: Pergamon Press.

Rao, N. K., & Rao, G. V. U. (1965). Intergrowths in ilmenite of the beach sands of Kerala. *Mineralogical Magazine, 35*(269).

Rečnik, A., Stanković, N., & Daneu, N. (2015). Topotaxial reactions during the genesis of oriented rutile/hematite intergrowths from Mwinilunga (Zambia). *Contributions to Mineralogy and Petrology C7 - 19, 169*(2), 1-22.

Reece, M., & Morrell, R. (1991). Electron microscope study of non-stoichiometric titania. *Journal of Materials Science, 26*(20), 5566-5574.

Roth, W. L. (1959). On the nature of defects in the magnetic structure of wüstite. *Journal of Applied Physics, 30*(4), S303-S304. doi: doi:http://dx.doi.org/10.1063/1.2185943

Sabioni, A. C. S., Huntz, A. M., Daniel, A. M. J. M., & Macedo, W. A. A. (2005). Measurement of iron self-diffusion in hematite single crystals by secondary ion-mass spectrometry (SIMS) and comparison with cation self-diffusion in corundum-structure oxides. *Philosophical Magazine, 85*(31), 3643-3658.

Sasaki, J., Peterson, N. L., & Hoshino, K. (1985). Tracer impurity diffusion in single-crystal rutile (TiO_{2-x}). *Journal of Physics and Chemistry of Solids, 46*(11), 1267-1283. doi: 10.1016/0022-3697(85)90129-5

Scoon, R. N., & Mitchell, A. A. (1994). Discordant iron-rich ultramafic pegmatites in the Bushveld Complex and their relationship to iron-rich intercumulus and residual liquids. *Journal of Petrology, 35*(4), 881-917. doi: 10.1093/petrology/35.4.881

Seda, T., & Hearne, G. R. (2004). Pressure induced Fe^{2+} + Ti^{4+} to Fe^{3+} + Ti^{3+} intervalence charge transfer and the Fe^{3+}/Fe^{2+} ratio in natural ilmenite ($FeTiO_3$) minerals. *Journal of Physics: Condensed Matter, 16*, 2707-2718.

Shannon, R., & Pask, J. A. (1964). Topotaxy in the anatase-rutile transformation. *American Mineralogist, 49*.

Shannon, R. D., & Rossi, R. C. (1964). Definition of topotaxy. *Nature, 202*(4936), 1000-1001.

Steele, J. L., & McCartney, E. R. (1969). Anisotropy of diffusion in rutile. *Nature, 222*(5188), 79-79.

Takeuchi, S., & Hashimoto, T. (1990). Deformation mechanisms in titanium dioxide single crystals. *Journal of Materials Science, 25*(1), 417-423.

Taylor, R. W. (1963). Liquidus temperatures in the system FeO-Fe_2O_3-TiO_2. *Journal of the American Ceramic Society, 46*(6), 276-279.

Taylor, R. W. (1964). Phase equlibria in the system FeO-Fe_2O_3-TiO_2 at 1300°C. *The American Mineralogist, 49*, 1016-1030.

Thompson, R. (1976). Chemistry of ilmenites crystallized within the anhydrous melting range of a tholeiitic andesite in pressures between 5 and 26 kb. *Mineralogical Magazine, 40*, 857-862.

Toplis, M. J., & Carroll, M. R. (1995). An experimental study of the influence of oxygen fugacity on Fe-Ti oxide stability, phase relations, and mineral—melt equilibria in ferro-basaltic systems. *Journal of Petrology, 36*(5), 1137-1170. doi: 10.1093/petrology/36.5.1137

Verhoogen, J. (1962). Oxidation of iron-titanium oxides in igneous rocks. *The Journal of Geology, 70*(2), 168-181.

Waychunas, G. A. (1991). Crystal chemistry of oxides and oxyhydroxides *Reviews in Mineralogy and Geochemistry* (Vol. 25, pp. 11-68).

Wechsler, B. A., & Prewitt, C. (1984). Crystal structure of ilmenite ($FeTiO_3$) at high temperature and at high pressure. *American Mineralogist, 69*, 176-185.

Wilson, N. C., Muscat, J., Mkhonto, D., Ngoepe, P. E., & Harrison, N. M. (2005). Structure and properties of ilmenite from first principles. *Physical Review B, 71*(7), 075202.

Wittke, J. P. (1966). Diffusion of transition metal ions into rutile (TiO_2) *Journal of The Electrochemical Society, 113*(2), 193-194. doi: 10.1149/1.2423901

Wittke, J. P. (1967). Solubility of iron in TiO_2 (Rutile). *Journal of the American Ceramic Society, 50*(11), 586-588.

Wu, X., Qin, S., & Dubrovinsky, L. (2010). Structural characterization of the FeTiO3–MnTiO3 solid solution. *Journal of Solid State Chemistry, 183*(10), 2483-2489.

Zhang, G., & Ostrovski, O. (2002). Effect of preoxidation and sintering on properties of ilmenite concentrates. *International Journal of Mineral Processing, 64*(4), 201-218. doi: 10.1016/S0301-7516(01)00055-2

Zhang, J., Zhu, Q., Xie, Z., Lei, C., & Li, H. (2013). Morphological changes of Panzhihua ilmenite during oxidation treatment. *Metallurgical and Materials Transactions B, 44*(4), 897-905.

Zhu, T., & Gao, S.-P. (2014). The stability, electronic structure, and optical property of TiO_2 polymorphs. *The Journal of Physical Chemistry C, 118*(21), 11385-11396.

Bibliography

Publications Related to the Thesis

Rečnik, A., Stanković, N., & Daneu, N. (2015). Topotaxial reactions during the genesis of oriented rutile/hematite intergrowths from Mwinilunga (Zambia). *Contributions to Mineralogy and Petrology C7 - 19, 169*(2), 1-22.

Stanković, N., Rečnik, A., & Daneu, N. (2015). Topotaxial reactions during oxidation of ilmenite single crystal. *Journal of Materials Science*, 1-11.

Journal Articles

Zavašnik, J., Stanković, N., Arshad, S., & Rečnik, A. (2014). Sonochemical synthesis of mackinawite and the role of Cu addition on phase transformations in the Fe–S system. *Journal of Nanoparticle Research C7 - 2223, 16*(2), 1-13.

Pantić, J., Kremenović, A., Došen, A., Prekajski, M., Stanković, N., Baščarević, Z., & Matović, B. (2013). Influence of mechanical activation on sphene based ceramic material synthesis. *Ceramics International, 39*(1), 483-488.

Conference Papers

Daneu, N., Stanković, N., & Rečnik, A. (2015). Topotaxial reactions at the atomic scale - the origin of sagenitic rutile and rutile/hematite intergrowths. In *Proceedings of the 6th MSCC, 6th Mineral Sciences in the Carpathians Conference.* Veszprem, Hungaryg. Acta mineralogica-petrographica.

Češarek, M., Stanković, N., Daneu, N., Rečnik, A., & Čeh, M. (2015). The role of sample preparation on the accuracy of EBSD pattern indexation studies on the rutile/hematite intergrowths. In *Book of tutorials and abstracts of EMAS, 2015.* Piran, Slovenia.

Stanković, N., Rečnik, A., & Daneu, N. (2015). Phase transformation of ilmenite single crystal during oxidation in air. *In Proceedings of the 9th Young researchers' day.* Ljubljana, Slovenia. Jožef Stefan Institute.

Stanković, N., Rečnik, A., & Daneu, N. (2015). Imenite single crystal transformation to rutile and hematite induced by heating in air atmosphere.. In *Program and the book of abstracts of the 3CSCS-2015, 3rd Conference of the Serbian Ceramic Society.* Belgrade, Serbia. Institute for Multidisciplinary Research.

Stanković, N., Rečnik, A., Šturm, S., & Daneu, N. (2014). Topotaxial transformation of ilmenite ($FeTiO_3$) single-crystals to rutile (TiO_2) and hematite (Fe_2O_3) during thermal treatment. In *Proceedings of the 18th International Microscopy Congress.* Prague Czech, Republic. Microscopy for global challenges: touching atoms, molecules, nanostructures and cells by multidimensional microscopy.

Stanković, N., Rečnik, A., Hanžel, D., & Daneu, N. (2014). Thermally induced topotaxial transformation of ilmenite single-crystals to rutile and hematite. In *Proceedings of the 8th Young Researchers' Day.* Ljubljana, Slovenia. Jožef Stefan Institute.

Stanković, N., Rečnik, A., & Daneu, N. (2013). Topotaxial transformation of ilmenite to rutile and hematite. In *Proceedings of the 2CSCS-2013, 2nd Conference of the Serbian Ceramic Society.* Belgrade, Serbia. Institute for Multidisciplinary Research.

Stanković, N., Rečnik, A., & Daneu, N. (2013). Formation mechanism of hematite-rutile pseudomorphs from Mwinilunga (Zambia). In *Proceedings of the 23rd V. M. Goldschmidt Conference.* Florence, Italy.

Stanković, N., Daneu, N., & Rečnik, A. (2012). Transformation of ilmenite to rutile and hematite pseudomorphs from Mwinilunga (Zambia). In *20. jubilejna konferenca o materialih in tehnologijah.* Portorož, Slovenia. Inštitut za kovinske materiale in tehnologije.

Stanković, N., Daneu, N., & Rečnik, A. (2012). Rutile and hematite pseudomorphs from Mwinilunga (Zambia). In *Joint 5th Mineral Sciences In The Carpathians Conference (MSCC) and 3rd Central-European Mineralogical Conference (CEMC).* Miskolc, Hungary. Acta mineralogica-petrographica, Abstract series

Biography

The author of this thesis, Nadežda Stanković, was born on 7 April 1984 in Belgrade, Serbia. In October 2002 she enrolled the bachelor study at the University of Belgrade, Faculty for Mining and Geology at the department for Mineralogy and Crystallography. She finished her studies with the average mark 9.08 (6-10). She defended a diploma with the title "Mineral composition and mechanism of black crust formations on the 'Kralj kapija' monument, Kalemegdan" on 25 June 2009 under the supervision of Dr. Suzana Erić. For her excellent marks during her studies, she was awarded the government support for gifted young scientists in the period from 2006-2009. Also, she attended two summer schools Erasmus Intensive Programme in 2006 and 2007. During the studies she also spent 4 months in Ljubljana, Slovenia at the University of Ljubljana, Faculty of Natural Sciences and Engineering, Department of Geology, under the guidance of Prof. Dr. Breda Mirtič.

She enrolled the PhD studies at the Jožef Stefan Postgraduate School in October 2011. Her PhD was mainly focused on the microscopy characterization of minerals at atomic level. During the studies she attended the School for Quantitative Electron Microscopy in May 2013 where she was studying various techniques for quantitative analyses at atomic level with help from various quantitative microscopy techniques like EELS and EDS. She presented her results at two international conferences from the field. One was in the field of geochemistry: Goldschmidt 2013, at Florence and the other was in the field of microscopy in Prague 2014.